

**A Study on**  
**Passive Aerothermodynamic Flow Control Methods for**  
**Hypersonic Lifting Body Configurations**  
(極超音速揚力飛行体形状に対する非能動的熱空気力学的  
流れ制御に関する研究)

**Shashank Khurana**  
シャシャンク クラナ



to the  
DEPARTMENT OF ADVANCED ENERGY  
GRADUATE SCHOOL OF FRONTIER SCIENCES (G.S.F.S.)  
THE UNIVERSITY OF TOKYO

June 2013

## **Dedication**

This work is dedicated to my parents Mr. Satish Khurana and Mrs. Veenu Khurana, my late Grandparents, Mr. Narayan Das Khurana and Mrs. Kaushalya Devi Khurana (paternal), and Mr. Kedarnath Kapoor and Mrs. Sudarshan Kapoor (maternal); and to my loving sister Ms. Rini Khurana.

# CONTENTS

Abstract.....	(vii)
Nomenclature.....	(ix)
List of Figures.....	(xi)
List of Tables.....	(xv)

## CHAPTER 1

### **INTRODUCTION.....1**

1.1 Introduction of Flow Field	1
1.2 Drag on Bodies	2
1.3 Flow Control for Drag Reduction	3
1.3.1 Active Control Methods	3
1.3.2 Passive Control Methods	4
1.4 Need for Blunt Nose	5
1.5 Lifting Body Configuration	5
1.5.1 Need and Motivation	5
1.5.2 Application	6
1.6 Drag Reduction	6
1.6.1 Wave Drag Reduction	6
1.6.1.1 Wave Drag Reduction Techniques	6
1.6.1.2 Aerospike Technique	7
1.7 Base Drag Reduction	8
1.7.1 Factors affecting Base Drag Control	9
1.7.2 Base Drag Reduction Techniques	9
1.7.2.1 Breathing Blunt Nose Technique	9
1.8 Research Objective	11

## CHAPTER 2

### **GEOMETRIC CONFIGURATIONS.....15**

2.1 Lifting Body Configuration	15
2.1.1 Non-axisymmetric Nose Delta Configuration	16
2.1.2 Axisymmetric Nose Delta Configuration	20
2.2 Aerospike Technique	22

2.2.1 Non-axisymmetric Nose Delta Configuration	22
2.2.1.1 60°–Swept Leading Edge Configuration	22
2.2.1.1.1 Aerospike-geometry considerations	24
2.2.1.2 70°–Swept Leading Edge Configuration	25
2.2.1.2.1 Aerospike-geometry considerations	25
2.2.2 Axisymmetric Nose Delta Configuration	27
2.2.2.1 Aerospike-geometry considerations	27
2.3 Breathing Blunt Nose Technique	28
2.3.1 Axisymmetric Nose Delta Configuration	28
2.3.1.1 Nose-hole considerations	28

### **CHAPTER 3**

#### **METHOD DESCRIPTION.....31**

3.1 Hypersonic Wind Tunnel Experiments	31
3.1.1 Hypersonic Wind Tunnel	31
3.1.1.1 Wind Tunnel Specifications	32
3.1.1.2 Test Conditions	32
3.1.1.3 Instrumentation	33
3.1.1.3.1 Model Manufacturing	33
3.1.1.3.2 Force measurements	34
3.1.1.3.3 Heat Transfer Measurements	35
3.1.1.3.4 Schlieren System	36
3.1.1.4 Experimental Data Uncertainty	37

### **CHAPTER 4**

#### **RESULTS AND DISCUSSIONS.....39**

4.1 Non-axisymmetric Nose Delta Configuration	39
4.1.1 Schlieren Visualization	39
4.1.2 Force Measurements Results	39
4.1.3 Heat Transfer Measurement Results	42
4.2 Aerospike Investigation	46
4.2.1 Hypersonic Wind Tunnel Investigation	46
4.2.1.1 Non-axisymmetric Nose Delta Configuration	46
4.2.1.1.1 60°–Swept Leading Edge Configuration	46
4.2.1.1.1.1 Schlieren Visualization	47

4.2.1.1.1.2 Force Measurements Results	51
4.2.1.1.1.3 Heat Transfer Measurement Results	54
4.2.1.1.2 70°–Swept Leading Edge Configuration	58
4.2.1.1.2.1 Force Measurements Results	58
4.2.1.1.2.2 Heat Transfer Measurement Results	59
4.2.1.2 Axisymmetric Nose Delta Configuration	61
4.2.1.1.1.1 Schlieren Visualization	61
4.2.1.1.1.2 Force Measurements Results	62
4.2.1.1.1.3 Heat Transfer Measurement Results	64
4.3 Breathing Blunt Nose Investigation	67
4.3.1 Axisymmetric Nose Delta Configuration	67
4.3.1.1 Schlieren Visualization	67
4.3.1.2 Force Measurements Results	68
4.3.1.3 Heat Transfer Measurements Results	71
<b>CHAPTER 5</b>	
<b>CONCLUSIONS.....</b>	<b>75</b>
5.1 Aerospike Technique	75
5.2 Breathing Blunt Nose Technique	76
5.3 Consolidated Results	77
Appendix.....	79
Appendix A: Water Channel Experiments	79
A.1 Theory	79
A.2 Methodology	81
A.2.1 Test Conditions	82
A.2.2 Instrumentation	83
A.2.3 Data Acquisition and Processing	84
Case A	85
Case B	93
Case C	106
Case D	110

References.....	119
Acknowledgment.....	123
Related Publications .....	127

## Dissertation Abstract

With the retirement of conventional space shuttles and the emerging interest in the space tourism, the efforts to design and investigate various geometrical configurations added with different techniques for ensuring safe, reliable and economical travel have paced up. The increased drag and convective heating associated with flow at hypersonic speeds have a significant impact on the design of vehicles. Together with optimization design study, techniques for simultaneous control aerodynamic flow field have been researched for a long time, which can be classified into Active (requiring a dedicated energy source) and Passive Control Methods (manageable with simple modification in the geometry). Considering significant design and application complexities of Active control methods, Passive flow control techniques of using a forward-facing aerospike and breathing blunt nose concept were chosen as the potential candidates for the current investigation.

A forward-facing spike attached at the nose of a blunt-body has been established as a means to favorably modify the flow field with a significant influence on the aerodynamic characteristics in hypersonic flow and can be regarded as a prospective option for drag reduction and increase of (lift/drag)-ratio of blunt nosed flying vehicles. The various parameters to be considered includes spike length, shape, spike-nose configuration and angle of attack. However, the studies have been conducted only on simple axisymmetric geometries and not on representative lifting body shapes. Therefore, as a first of its kind study, the efforts were focused on analysis of using forward-facing aerospikes and its effectiveness with varying angle of attack ( $-10^\circ$  to  $+10^\circ$ ) and spike-nose configuration, on key aerothermodynamic parameters of drag and heat reduction for prospective application to two type of lifting body configurations, with leading edges swept at  $70^\circ$  forming a delta shape, one with a non-axisymmetric forward stagnation surface and another with an axisymmetric nose. Flow visualization was carried out using the schlieren technique. Measurements made at freestream Mach number 7 with six-component force balance system revealed a large increase in the Lift/Drag Ratio and marginal increase in pitching moment coefficient compared to no-spike case, together with overall reduction in the nose surface area exposed to heating, with aerospikes proving worthy

at high angles of attack; thereby indicating their practical feasibility for eventual future applications to spacecrafts.

Breathing blunt nose concept study, proposed for drag reduction, by bleeding the air from nose and discharging it at the base, in an attempt to increase the pressure at the base of the body, hence reducing the contribution from base drag against the direction of motion. This concept also has been studied on simple basic geometries only, therefore it has been investigated for practical feasibility and application on lifting body configurations with the help of wind tunnel experiments carried out at Mach 7 on a  $70^\circ$  swept-back lifting body shape forming a delta shape, with axisymmetric nose, and using shallow water channel visualization technique. The visualization results highlights the similarity between the flow field estimated by the two methods, and the latter provides an insight into the flow physics of inside the channel with an assumption of quasi one-dimensionality. The aerodynamic measurements at the wind tunnel demonstrated that with the breathing blunt nose, the drag can be fairly reduced without adversely affecting the stability of the basic body, proving it worthy of practical utility, and underlines the existence of limit of bleeding from the nose.

Both the techniques have been proven to be worthy of favorably modifying the flow field resulting in the improvement of aerodynamic characteristics over the basic reference configuration. The only issues that needs to be addressed, for aerospikes, includes optimum selection of aerospike for a specific body for avoiding any reattachment of shear layer on the body and to curb the extra normal force component acting on the spike nose at higher angles of attack which needs to be taken into consideration. For the breathing blunt nose concept, the design of the channel, for carrying and discharging the high pressure and high temperature air from the nose to the base, needs dedicated study for maximizing the drag reduction and to bear the heat load of the from the air bled and moving inside the channel. The results obtained by investigating the flow features around various configurations, by varying the geometric parameters, are valid within the parameters investigated here.

# Nomenclature

$A$	: reference area
$B$	: bias limit
$c$	: specific heat of material
$C.G.$	: center of gravity
$C_{AF}$	: coefficient of axial force
$C_D$	: coefficient of drag
$C_h$	: normalized heat transfer coefficient
$C_L$	: coefficient of lift
$C_m$	: coefficient of pitching moment
$C_N$	: coefficient of normal force
$C_p$	: specific heat of material
$d$	: root diameter
$D$	: nose diameter
$F_{AF}$	: axial force
$F_N$	: normal force
$h$	: distance between balance center and center of pressure
$h_b$	: height of the vehicle
$k$	: student value
$K$	: thermal conductivity of material
$l$	: characteristic length
$L$	: length of leading edge
$L_{lead}$	: length of nose-leading edge junction to the base
$L_{tot}$	: total geometrical length
$M$	: mach number
$N$	: number of sample readings
$P$	: precision limit
$P_0$	: stagnation pressure
$q$	: dynamic pressure
$q_s$	: heat transfer rate through conduction
$r$	: cylinder radius

$r_t$	: distance from stagnation point to nose end wing length
$R_b$	: wing length
$R_C$	: radius of curvature
$t$	: time
$\Delta t$	: time interval
$T$	: temperature
$\Delta T$	: surface temperature rise
$v_\infty$	: freestream velocity
$x_t$	: length of nose region
$\alpha$	: angle of attack
$\rho$	: density of material
$\Lambda$	: sweepback angle
CON	: conical nose aerospike
FL	: flat nose aerospike
HS	: hemispherical nose aerospike
NO	: no-spike body
SQ	: square nose aerospike

#### Subscripts

b	: balance center
eq	: equivalent
min	: minimum
max	: maximum
s	: spike
w	: wall condition
0	: stagnation condition
$\infty$	: ambient condition

# List of Figures

- Figure 1.1. Mechanism using spiked blunt bodies in hypersonic flow
- Figure 1.2. Flow field around breathing blunt nose
- Figure 1.3. Drag characteristics
- Figure 1.4. Tree of Doctoral Research
- Figure 2.1. Schematic of lifting body of typical hypersonic vehicle (a) Plan-view (b) Side-view
- Figure 2.2. Bicurvature geometry
- Figure 2.3. Schematic of hypothesized delta configuration
- Figure 2.4. Experimental models of configurations
- Figure 2.4 Experimental test model.
- Figure 2.5. Representative (reference) geometry.
- Figure 2.6. Experimental spiked model.
- Figure 2.7. Spike nose configuration.
- Figure 2.8. Experimental test model with holes.
- Figure 3.1. Hypersonic Wind Tunnel
- Figure 3.2. Typical time-sequence.
- Figure 3.3. Rapid-prototyping machine
- Figure 3.4. Six-strain gauge force balance system.
- Figure 3.5. Data recorder system.
- Figure 3.6. Xenon lamp and reflecting mirror.
- Figure 3.7. TP-L series thermal imaging sensor
- Figure 3.8. Knife-edge section and video source.
- Figure 3.9. A typical model setup inside test section
- Figure 4.1. Schlieren picture for  $\Lambda = 70^\circ$  at  $\alpha = 0^\circ$
- Figure 4.2.  $C_L$  v/s  $\alpha$  variation for various  $\Lambda$
- Figure 4.3.  $C_D$  v/s  $\alpha$  variation for various  $\Lambda$
- Figure 4.4. (*Lift/ Drag*) ratio v/s  $\alpha$  variation for various  $\Lambda$
- Figure 4.5 Instantaneous temperature ( $^\circ\text{C}$ ) distribution at  $\alpha = 0^\circ$  for different  $\Lambda$
- Figure 4.6 Heat transfer along leading edges with  $x/L$  for different  $\Lambda$  at  $\alpha = 0^\circ$
- Figure 4.7 Instantaneous temperature ( $^\circ\text{C}$ ) distribution at  $\alpha = 10^\circ$  for different  $\Lambda$
- Figure 4.8 Heat transfer along leading edges  $x/L$  variation for various  $\Lambda$  at  $\alpha = 10^\circ$

Figure 4.9 Instantaneous temperature ( $^{\circ}\text{C}$ ) distribution for  $\Lambda=70^{\circ}$  at different  $\alpha$

Figure 4.10  $T_{\max}$  v/s  $x/L$  variation for  $\Lambda=70^{\circ}$  at different  $\alpha$

Figure 4.11 Schlieren pictures for no-spike body at  $\alpha=0^{\circ}$

Figure 4.12. Schlieren pictures and schematic diagram for hemispherical spike at  $\alpha=0^{\circ}$

Figure 4.13. Schlieren pictures and schematic diagram for flat faced spike at  $\alpha=0^{\circ}$

Figure 4.14. Schlieren pictures and schematic diagram for conical spike at  $\alpha=0^{\circ}$

Figure 4.15. Schlieren pictures (side view) for no-spike body

Figure 4.16. Schlieren pictures (side view) for flat-faced spike

Figure 4.17. Coefficient of lift comparison with angle of attack

Figure 4.18. Coefficient of drag comparison with angle of attack

Figure 4.19. Lift/Drag-ratio comparison with angle of attack

Figure 4.20. Coefficient of pitching moment comparison with angle of attack

Figure 4.21. Time-history of maximum surface temperature ( $T_{w,\max}$ )

Figure 4.22  $T_w/T_0$ -variation with non-dimensional length along nose curvature at  $\alpha=0^{\circ}$  and  $t=33$  sec

Figure 4.23. Normalized heat flux comparison with non-dimensional length along nose curvature at  $\alpha=0^{\circ}$  and  $t=33$  sec

Figure 4.24. Model inspection after the experiment

Figure 4.25. Lift/Drag Ratio variation with angle of attack

Figure 4.26. Instantaneous temperature profile over model without spike captured by InfraRed camera at  $\alpha=0^{\circ}$ . (temperature scale in  $^{\circ}\text{C}$ )

Figure 4.27. Instantaneous temperature profile over model with spike captured by InfraRed camera at  $\alpha=0^{\circ}$ . (temperature scale in  $^{\circ}\text{C}$ )

Figure 4.28. Schlieren pictures for model without spike at  $\alpha = 0^{\circ}$

Figure 4.29. Schlieren pictures for model with hemispherical nose spike with  $l/D=1.5$  at  $\alpha = 0^{\circ}$

Figure 4.30. Lift/Drag-ratio variation with angle of attack

Figure 4.31. Variation of pitching moment coefficient with angle of attack

Figure 4.32. Temperature distribution around body without spike at  $\alpha = 0^{\circ}$  (temperature in  $^{\circ}\text{C}$ )

Figure 4.33. Temperature distribution around body with conical nose spike ( $l/D=1.0$ ) at  $\alpha = 0^{\circ}$  (temperature in  $^{\circ}\text{C}$ )

Figure 4.34. Schlieren pictures for model without nose hole

Figure 4.35. Schlieren pictures for model with  $\phi 5$  mm nose hole

Figure 4.36. Schlieren pictures for model with  $\phi 7$  mm nose hole  
Figure 4.37.  $C_L$ -variation with  $\alpha$   
Figure 4.38.  $C_D$ -variation with  $\alpha$ .  
Figure 4.39. (Lift/Drag)-Ratio variation with  $\alpha$   
Figure 4.40.  $C_m$ -variation with  $\alpha$   
Figure 4.41. Instantaneous temperature ( $^{\circ}\text{C}$ ) distribution around the lifting body configurations

Figure A.1. (a) Schematic diagram of the experimental set-up (dimensions in mm), (b) pictorial view of the set-up.

Figure A.2. Still camera for capturing pictures

Figure A.3. Flow field nomenclature

Figure A.4. Test geometry with spike configurations

Figure A.5. Flow field around the test models at  $Re=2277.6$

Figure A.6. Flow field around the hemispherical spiked models at varying  $Re$

Figure A.7.  $H/D$ -variation for various spikes

Figure A.8.  $H/D$ -variation with  $Re$ .

Figure A.9.  $Z/D$ -variation for various spikes

Figure A.10.  $Z/D$ -variation with  $Re$

Figure A.11.  $V/D$ -variation for various spikes

Figure A.12.  $V/D$ -variation with  $Re$

Figure A.13. Schematic of the basic body and spike configurations

Figure A.14. Flow field nomenclature.

Figure A.15. Flow field for various test cases for  $l/D = 0.5$

Figure A.16. Flow field for various test cases for  $l/D = 1.0$

Figure A.17. Flow field for various test cases for  $l/D = 1.5$

Figure A.18. Flow field for various test cases for  $l/D = 2.0$

Figure A.19.  $H/D$ -variation around the nose for various spikes

Figure A.20.  $Z/D$ -variation around the nose for various spikes

Figure A.21. Flow field showing near-nose region with ( $l/D=1.5$ ) and without spike

Figure A.22.  $V/D$ -variation around the nose for various spikes

Figure A.23. Flow field showing wake region with ( $l/D=2.0$ ) and without spike

Figure A.24.  $W/D$ -variation around the base for various spikes

- Figure A.25. Test geometry with spike configurations
- Figure A.26. Flow field around the basic body (no vortices)
- Figure A.27. Flow field for spiked with conical-nose
- Figure A.28. Flow field for spike with flat-nose
- Figure A.29. Flow field for spike with hemispherical-nose
- Figure A.30. Typical models for water channel visualization
- Figure A.31. Time-captured images around no-hole body at  $\alpha=0^\circ$
- Figure A.32. Time-captured images around  $\phi 5\text{mm}$  nose hole geometry at  $\alpha=0^\circ$
- Figure A.33. Time-captured images around  $\phi 7\text{mm}$  nose hole geometry at  $\alpha=0^\circ$
- Figure A.34. Two-dimensional flow field around representative geometries at  $\alpha=0^\circ$ .

# List of Tables

Table 3.1 Wind Tunnel Specifications

Table 3.2. Experimental test conditions

Table 4.1.  $T_0$ -variation for different cases.

Table 5.1. Conclusions in a consolidated manner

Table A.1. Hydraulic analogy

Table A.2. Reynolds Number for the test cases

## CHAPTER 1

# INTRODUCTION

### 1.1 Introduction of Flow Field

The flow field study, coined as aerodynamics, around any object has been credited a key design factor, especially in the design of aerospace vehicles. The design of such vehicles is dictated by the Mach number regime of the flow field in which the object is flying. The flow field can be classified in to different regimes depending on the change of fluid properties. A flow is classified as incompressible, if the density variation is negligibly small (less than 5%), and compressible, if the corresponding variation is significant (greater than 5%). Furthermore, it can be classified as a low-speed (where the temperature changes associated with the flow velocity is insignificant), and high-speed (where the temperature changes are significant). For distinguishing between the incompressible and compressible flow fields, the Mach number ( $M$ ) limit is taken as 0.3. Based on Mach number, the flow field is divided into four regimes. When  $M < 0.8$ , the flow field is called subsonic flow, in case of  $0.8 < M < 1.2$ , the flow field is termed as transonic regime, between  $1.2 < M < 5$  the flow field is called the supersonic regime, and  $M > 5$  is referred to as the hypersonic regime [1]. In supersonic and hypersonic flow fields the perturbations travels slower than the fluid speed. This leads to the formation of compression and expansion waves in supersonic and hypersonic flows. The flow field governs the aerodynamic performance of a flying body because the forces and moments experienced by the body are a strong function of the flow regimes in which the body is traversing.

The First hypersonic flight in the history dates back to late 1940's, that the first manufactured object German V-2 Rocket achieved, which was once thought to be impossible. In April 1961, Russian Major Yuri Gagarin became the first human to travel at hypersonic speed, during the world's first piloted orbital flight, in his craft Vostok I, traveling beyond Mach 25 [1]. Since then, there had been a massive

research in this field, to achieve a secured cost-effective means, which can be employed to cater the needs for traveling to planets and beyond, even as a means of commercial transportation system. Aerodynamicists are working on all the challenges posed by such an aerothermal environment. The exploration is still underway, and will lead to a discrete era of hypersonic flight.

The air-breathing Reusable Hypersonic Vehicles (RHV's) have high potential, due to their hyper-speeds, higher altitude flight, and compactness [2]. The RHV programs are initiated at several places across the globe, because they have applications in low cost space and time- critical military missions [3]. The RHV is a fully reusable vehicle that operates at hypersonic speeds for a significant part of its trajectory [4]. It incorporates various key technologies in design that are necessary to safely withstand the environment in hypersonic flight. The interest in TAVs is now renewed also as hypersonic sub-orbital transport and single or two-stage-to-orbit space vehicles [5]. The key problem related to the flights at hypersonic Mach numbers ( $M_\infty \geq 5$ ) is the aerodynamic or kinetic heating of the vehicle bodies. To survive through this, the RHV is equipped with Thermal Protection System (TPS). This reusable TPS must protect the vehicle as well as itself from the aerodynamic heating. Owing to the complexity in design of a particular TPS as per requirement, with a firm focus on minimizing the overall weight of TPS, being an additional weight on the vehicle, alternate techniques and methods have been constantly being devised and sought.

## **1.2 Drag on Bodies**

A body as a virtue of its motion in fluid experiences forces and moments as a result of relative fluid flow past it. The force on the body along the flow direction, retarding the body motion is called drag. In a subsonic flow field, the main components of the drag constitute the pressure drag due to flow separation and the skin friction drag due to viscous effects. On the other hand, the supersonic and hypersonic flights are dominated by three components of which include wave drag (due to the presence of strong compression fronts ahead of the body), skin friction drag (arising from the interaction between the fluid and the skin of the body) and base

drag (due to low pressure region as a consequence of flow separation at the base). The components of wave drag and base drag have long been considered as challenges for the vehicles (having a lifting body), and careful design considerations for minimizing them has been of foremost important for increasing the aerodynamic efficiency for economic use.

### **1.3 Flow Control for Drag Reduction**

Flow control techniques has been a subject of widespread research to improve the overall aerodynamic performance by effective manipulation of a flow field (by improving separation control, adjustment of sectional lift, drag reduction, noise suppression etc.) conceivably leading to a number of significant benefits required to aerospace vehicle systems, including enhanced performance, maneuverability, payload, propulsive efficiency and range, as well as lowered overall operating cost. Flight vehicles, travelling in high-speed regimes, encounter elevated drag forces through out their traversed path, whose suppression becomes the foremost requirement either by appropriate geometry modification or by introducing mechanisms to favorably modify the flow structure around the body.

The various flow control methods that have been devised and researched to cater this innate need of drag reduction can be broadly classified into active and passive controls [6]. Active Flow Control (AFC) employ an auxiliary power source, inbuilt, mounted or installed on the body, which utilizes predetermined algorithms for powered actuation to induce controlled disturbances in a flow field for controlling the drag on the body. Passive flow control, on the other hand, involves non-powered, physical devices that are either a permanent or a deployable fixture and draw the energy directly from the flow to be controlled. Both active and passive controls mainly aim at modifying the flow characteristics to get the desired reduction of drag, a consequent improvement in (lift/drag)-ratio and a possible reduction in local and total heat transfer to the body. Passive controls have the advantage of application with a simple geometric modification with negligible weight addition to the total weight of the vehicle.

#### *1.3.1 Active Control*

At supersonic speeds, major portion of drag consists of wave drag and base

drag. Active flow control technology influences and controls a natural stability of the flow to attain a large effect using small, localized energy input. Moreover, active control can be used to control complex, dynamical processes like turbulence production in turbulent boundary layers to reduce skin friction, and hence viscous drag, where the reduction is proportional to the surface area covered by the actuators. The various active control methods researched in the past include a forward facing counter jet flow to change the shock strength at nose of the flying object, plasma controlled pulsed jets to diminish the instabilities in the flow, fluidic, mechanical, and plasma actuator mechanisms for controlling the shear layer etc. All the control techniques require additional source of energy to be carried on flying vehicle, which results in additional weight constraints together with the complexity of design and installing the systems onboard the vehicle, which hinders and restricts the use of these methods to specific applications, where weight is not a concern.

### *1.3.2 Passive Control*

The passive controls are those, which do not require an additional source of energy. For drag reduction in supersonic and hypersonic regime, different kind of passive controls are in application. For nose drag reduction, spike at the nose, spike with different tipped bodies [7], sharp nose of different fineness ratio [8], straight and conical cavity at the nose etc. are used. For base drag reduction boat-tailed base, cavity at the base, breathing blunt nose [9] etc. are common. These techniques can be applied by physically permanent or deployable structures resulting in simple geometric modification, with negligible weight addition to the overall weight of the structure. These methods are best suited for the current research theme of blunt nose sections, where on one side the rewards of the former can be comprehensively enjoyed, on the other side, there is minimal design complexity and increasing weight issue involved. Owing to these major advantages, and considering the applications to high-speed flight vehicles, these methods will be investigated on simple representative geometries and their potential effectiveness on selected lifting body configurations. The most noticeable and apparently the most desired effect for these methods, which will be discussed throughout this study, is the decay of positive pressure at the nose, termed as “pressure hill”, by either weakening of the compression front (shock wave) or and/or re-positioning of the same away from the

body nose, variation and increase in the size of the vortices (recirculating region) generated near the body-nose, and the decay of negative base pressure in the wake region.

#### **1.4 Need for Blunt Nose**

Blunt nose sections are essential for high enthalpy missions because of their capability to withstand very high temperature, and capable of providing higher volumetric efficiency for encompassing additional payload in the form of passengers and or freight. In high-speed flows, blunt nose provides more area for heat transfer than a sharp nose owing to better flow relieving, which cannot sustain high temperature resulting in the ablation of material. But, the penalty for blunt nose is increased drag due to the formation of detached bow shock in front of the nose. Hence a settlement in this regard, by transforming the flow structure with the original configuration, becomes inevitable to exploit the advantages offered by the blunt sections.

#### **1.5 Lifting Body Configuration**

##### *1.5.1 Need and Motivation*

With the retirement of the conventional space shuttles, stationed for manned space travel for carrying out missions, and with the increasing interest in space tourism and commercial high-speed transportation system between different continents on earth, a new dimension of space age has open to cater all these requirements, motivating scientists and researchers to investigate newer designs for ensure economic, safe and reliable means for faster travel. To safeguard the inner load carrying structure without any significant increase in the overall weight, a lifting-body configuration needs to be obtained by compromising the design favorable for aerodynamic forces and aerodynamic heating viewpoints.

### *1.5.2 Application*

The fundamental configurations of reusable vehicle, capable of travelling at higher speeds, include a lifting body and winged structures. These configurations should be chosen according to the specified mission parameters. The aerodynamic characteristics of such configurations desired for next generation transportation systems include high (Lift/Drag)-ratio at all flow regimes, not only at hypersonic speed but also in transonic and subsonic speeds with static and dynamic stability.

## **1.6 Drag Reduction**

High speed flows are characterized by high aerodynamic drag (inclusive of wave drag, skin friction drag and base drag) induced by the presence of strong shock in front of the flight vehicle geometry and elevated surface heating due to deceleration behind the shock wave [1]. Numerous techniques have been reported in the literature to modify the flow field around the nose, to bring down the positive pressure gradient and the local heat concentration to safeguard the inner structure.

### 1.6.1 Wave Drag Reduction

The positive pressure distribution over the surface of the body in high-speed flows has been a topic of research, discussion and debate for many years now. The main focus in addressing wave drag is on relocating the position of shock wave far from the main body and to modify its structure in front of a sharp or a blunt nose, such that the high-pressure coefficient gets reduced in magnitude.

#### 1.6.1.1 Wave Drag Reduction Techniques

The initial studies, to counter the increase in wave drag at high Mach numbers, were focused on the use of thin probes protruding from the stagnation point of the blunt bodies at supersonic and hypersonic speeds. Mair [10] in 1952 performed a study on bodies of revolution with flat and hemispherical nose shapes, with and without thin protruded probes of different length, at Mach 1.96 and Reynolds number,  $Re = 1.3 \times 10^3$  per centimeter. Based on the results of his investigation, he explained

the physics of flow separation at supersonic speeds with the introduction of a protruding probe and the generation of multiple shock waves. For simultaneous reduction of wave drag and aerodynamic heating at high-speeds, a forward facing spike attached to the nose of the body, as a passive control device, had been investigated in detail in the past, using numerous experiments and numerical analysis [7].

#### 1.6.1.2 Aerospike Technique

Hypersonic flow is characterized by aerodynamic drag induced by the presence of strong shock in front of the flight vehicle geometry and elevated surface heating due to deceleration behind the shock wave [1]. For the simultaneous reduction of these phenomena for economic and safe transportation systems, an engineering trade-off needs to be employed. The concept of a forward-facing spike attached to the hemispherical nose has been proven effective through extensive wind tunnel experiments in the past for simple axisymmetric bodies in hypersonic flow [11,12]. A spike in front of the nose generates a weak oblique shock wave, standing away from the vehicle body, creating a recirculation region around the root of the spike (near the stagnation point) thereby decreasing heat transfer and pressure around the stagnation region as depicted in Figure 1.1. The principal physics behind the introduction of the spike is the shifting of the entire pressure zone acting on the nose of the body onto a small spike nose, thereby generating weak foreshocks and creating low-pressure regions near the spike root. This has been observed to be present and equally effective when checked for their application to lifting body configurations, for the preliminary investigations for pre-decided experimental parameters. The key objective is the behavior and shifting of low-pressure recirculation region at different attitudes of the vehicle, changing the complete aerodynamic characteristics. For lifting body configurations, flying at high angles of attack and performing maneuvers, the effectiveness of using a forward-facing spike needs to be studied in detail through simultaneous experimental and numerical investigations, before arriving at a definite conclusion, as the former acts as a dead weight and does affect the longitudinal stability, which might pose serious concerns for the lifting body.

Recently, the interest in the use of aerospikes for prospective space transportation applications has been renewed and caught global attention. Kubota et

al.[13,14] has effectively conducted research on spiked blunt bodies with aerodisks and aerospikes and concluded disks to be more effective than spikes. They also emphasized that proper selection of aerospikes holds a great potential for passive thermal protection and drag reduction. Kalimuthu et al.[15,16] experimentally investigated influence of aerospikes with varying spike-nose configurations and  $l_s/D$  on blunt body at hypersonic mach numbers. Menezes et al.[17] conducted shock tunnel study on aerospikes and numerically verified the results proving the drag-reduction effectiveness by about 50% for the considered configurations. Mehta [18] focused his research on the peak heating and pressure distribution around reattachment area of separated flow by numerical analysis using axisymmetric, compressible Navier-Stokes equation employing finite volume discretization. From a thorough literature review, it has been proclaimed that investigation of aerospikes is limited only to basic representative axisymmetric shapes. To extend the study of aerospike application and to check its effectiveness for the lifting-body configurations became the motivation behind this study. Hence, in the current research, the efforts were focused on analyzing aerospike influence on wave drag and heat transfer reduction parameters of lifting-body configurations for their prospective futuristic applications.

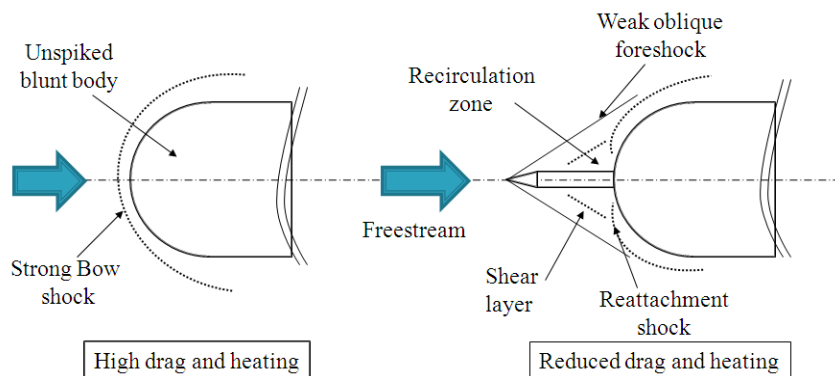


[Figure 1.1. Mechanism using spiked blunt bodies in hypersonic flow.]

### 1.7 Base Drag Reduction

The base drag is caused due to the built of low-pressure region at the base, that is, in the wake region behind the body. The low-pressure region results in a negative

pressure coefficient, thereby adding to the resistance offered to the flow, known as the base the drag. Therefore in order to curb the base drag, the pressure at the base needs to be increased such that the results force in the longitudinal direction, against the direction of motion of body gets reduced.

### 1.7.1 Factors affecting Base Drag Control

The base pressure is a strong function of the Reynolds number, Mach number, body temperature and the shape of the body.

### 1.7.2 Base Drag Reduction Techniques

#### 1.7.2.1 Breathing Blunt Nose Technique

A new concept, coined as *breathing blunt nose* (BBN) [9,19], was proposed, as a technique to tackle the problem of low pressure region at the base (wake region), thereby increasing the base pressure, and consequently reduction in the contribution of base drag.

The flow field around a breathing blunt nose is illustrated in Figure 1.2. In this technique, the flow is made to pass through a small hole on the nose of the body, and the high-pressure air is released at the base. This results in the weakening of the shock thereby reducing the positive pressure exerted at the nose. Moreover, the high-pressure flow discharged at the base increases the base pressure, resulting in the decrease of base drag. This technique tackles both the wave drag and base drag simultaneously. Furthermore, the heat generation due to skin friction is bound to be convected away by the air flowing through the inner surface. For a blunt nose without breathing, a strong bow shock stands in front of the nose. The high-pressure zone (a high pressure coefficient), around the stagnation area, is relieved by breathing the air through a hole of predetermined dimension from the nose, and the discharge of the high pressure air at the base increases the pressure coefficient, thereby decreasing the net pressure against the direction of flow.

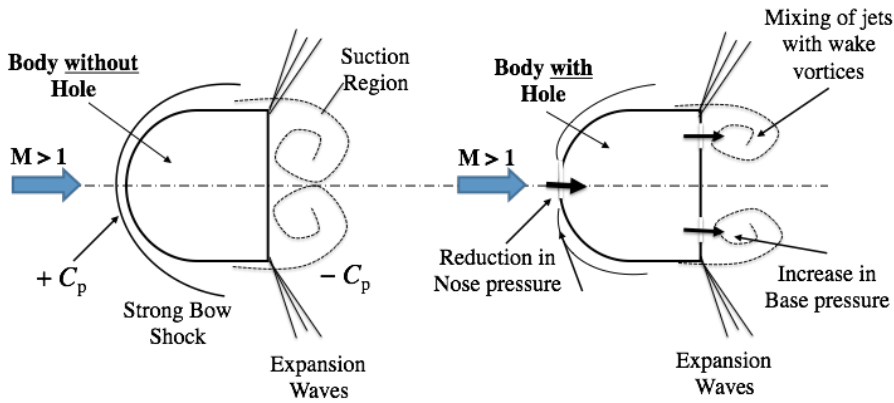


[Figure 1.2. Flow field around breathing blunt nose.]

Ashish and Rathakrishnan [9] described the physics behind this technique which results in the reduction of pressure drag of a blunt nosed body in the form of a breathing nose at a supersonic Mach number, as a passive flow control technique. The drag of a blunt nosed body with and without breathing nose at Mach 1.96 was compared. Imamura et al. [19] investigated this technique on a hemispherical-cylinder forebody and found out that it was effective in reducing the drag by about 10 percent at Mach 7, as depicted in Figure 1.3, with equally valid with the increase in angle of attack.

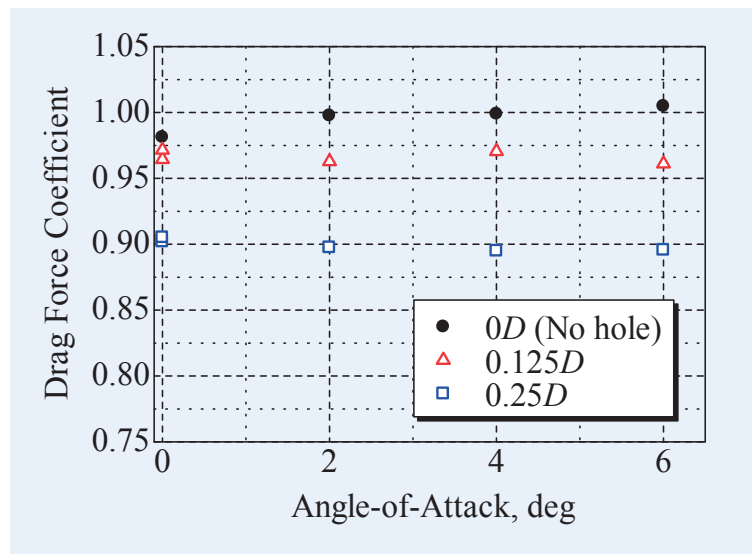


[Figure 1.3 Drag characteristics [19]]

The studies on the breathing blunt nose at supersonic and hypersonic speeds, were conducted only for simple hemisphere-cylindrical forebody model which are essentially non-lifting bodies. Therefore in order to assess its practical feasibility and effectiveness, the present study focuses on the application and investigation of this concept to the lifting body configurations.

### 1.8 Research Objective

There are two objectives for this research. The primary objective is to identify the promising candidates for the passive flow control techniques in a high-speed flow. The secondary objective is to investigate and assess the effectiveness of those techniques on applications to lifting body configurations. The prospective application of these techniques have been considered to be of hypersonic commercial transportation system between two places on earth, by maximizing the payload and the number of passengers, for a safe, economic, reliable and reusable transportation means. The objectives can be summarized as under: -

- Establishing passive techniques capable of favorably modifying the flow field around the nose, lifting surface and entire body
- Investigating the desired flow performance on simple geometries, and extending the study to lifting-body configurations to check for their feasibility and effectiveness
- Carrying out fundamental design study, on selected lifting body configurations, with reference to various key parameters of flow control techniques
- Key focus on the reduction of wave and base drag and consequently increasing (Lift/Drag)-ratio, together with eliminating heat concentration zones

Figure 1.4 illustrates the tree of the doctoral research, as a flowchart, to highlight and clearly explain the flow of research path considered given two problem domains of high wave drag and nose heating, and high base (wake) drag. The two

passive techniques of aerospike and breathing blunt nose, considering the first problem of high wave drag and nose heating, were investigated for two lifting body shapes, namely a hypothesized and a practical shape lifting body configuration. Hypothesized lifting body configuration is a combination of non-axisymmetric two-dimensional toroidal shape stagnation surface (nose) followed by sweptback leading edges forming a delta-type lifting body. Practical shape lifting body consists of an axisymmetric nose, followed by sweptback leading edges forming a delta shape (a simplified configuration derived from that of an X-33 vehicle), symmetric about the longitudinal axis. Breathing blunt nose technique, consisting of nose holes followed by a channel, for the discharge of the high-pressure air, was deemed convenient and useful for the practical body shape in the present study owing to the complexity of channel design. This technique has its importance in reducing the wave drag at the nose of the body and simultaneously increasing the pressure at the base, also reducing the base drag. Therefore this technique was checked for practical body shapes only. As for the forward-facing spike technique is concerned, the investigation has been carried to analyze the effect of the presence of spike on wave drag and heating for both lifting body shapes, whereas to investigate its effect on base drag, only practical body shape has been considered.

In this regard, the conclusions derived from the investigations by understanding the behavior of the two techniques on entire flow field, as applied to lifting body configurations, have been summarized, and then generalized by citing and explaining its applications, together with any limitations or shortcomings, if any, within the parameters of the current study.

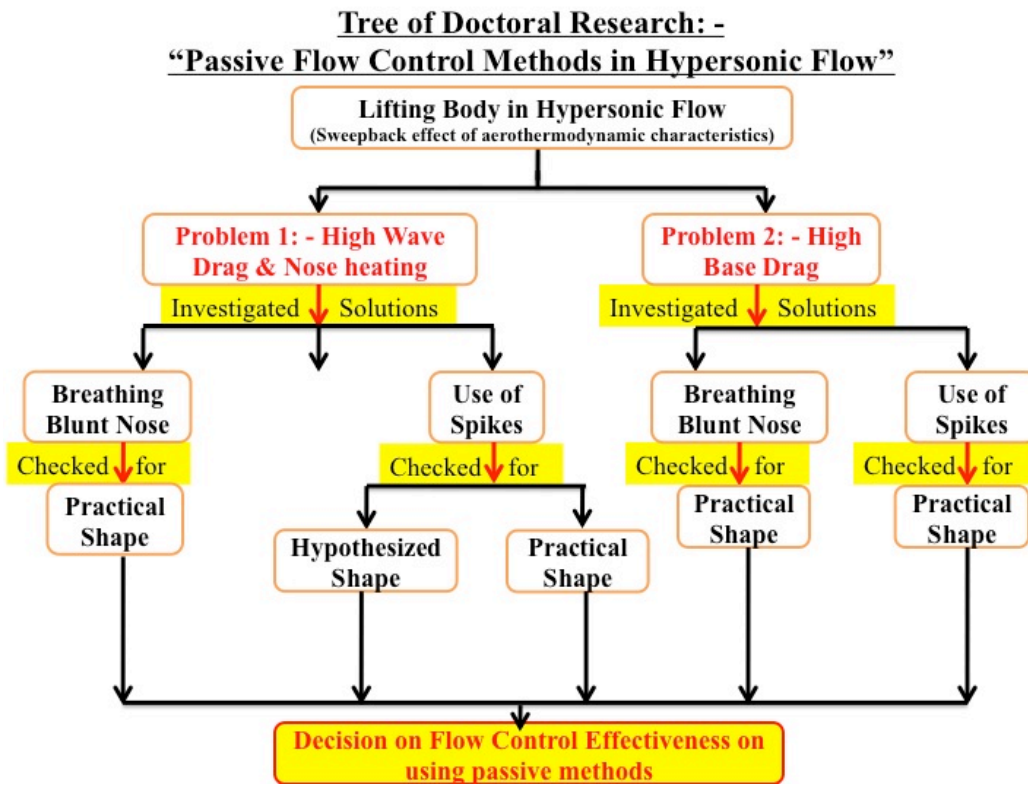


[Figure 1.4. Tree of Doctoral Research]



## CHAPTER 2

# GEOMETRIC CONFIGURATIONS

### 2.1 Lifting Body Configuration

Over the years, a lifting-body configuration design with low drag and low heat characteristics has been focused upon to cater to a large number of prospective applications. Townend [20] concluded that a hypersonic vehicle needs to have a blunt nose with a lifting body configuration.

Mahulikar [21] hypothesized a configuration consisting of a non-axisymmetric bicurvature stagnation surface with swept back leading edge (SBLE) having sweep back angle ( $\Lambda$ ), as shown in Figure 2.1. Mahulikar hypothesized that at  $\Lambda=0^\circ$ , the leading edge essentially behaves as a straight cylinder in cross flow, and at  $\Lambda=90^\circ$  its surface can be approximated as a flat plate. Mahulikar et al. [22] performed experimental investigations on geometries representing hypersonic vehicles in subsonic wind tunnel using the principle of heat transfer characteristics, being independent of direction of heat transfer, by heating the sample with use of heaters placed inside the hollow aluminum samples and the ambient air was used to cool them unlike the usual case where the space shuttle gets heated by the ambient air at hypersonic speeds. Here, the qualitative heat transfer characteristics remain unaffected and hence the importance of blunting and sweepback was emphasized.

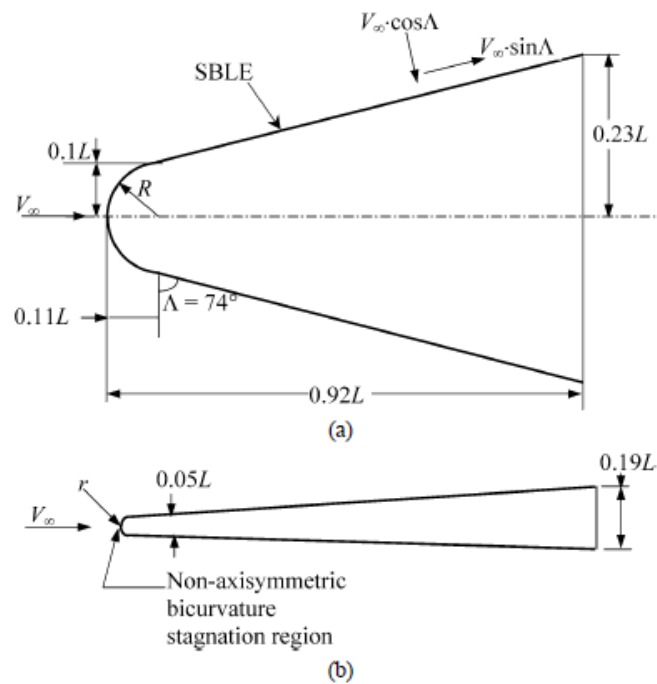


[Figure 2.1. Schematic of lifting body of typical hypersonic vehicle (a) Plan-view (b) Side-view [21]]

### 2.1.1 Non-axisymmetric Nose Delta Configuration

It has been long discussed and corroborated that the heat transfer rate to the body's vehicles surface is deemed as a function of *vehicle's geometry* and *trajectory* of a particular mission.

- Temperature rise in stagnation region flow due to reversible conversion of flow-work to heat
- Insignificant heat generation due to viscous dissipation because of low velocities in stagnation region
- Convection occurs between  $T_w$  & temperature at low velocity boundary layer edge,  $T_0$
- **Bicurvature forward stagnation surface:**

“cylinder of radius  $r$  bent in plane perpendicular to  $r$  by radius  $R$ ”

- Effect of bicurvature is to reduce 2-dimensional thermal resistances

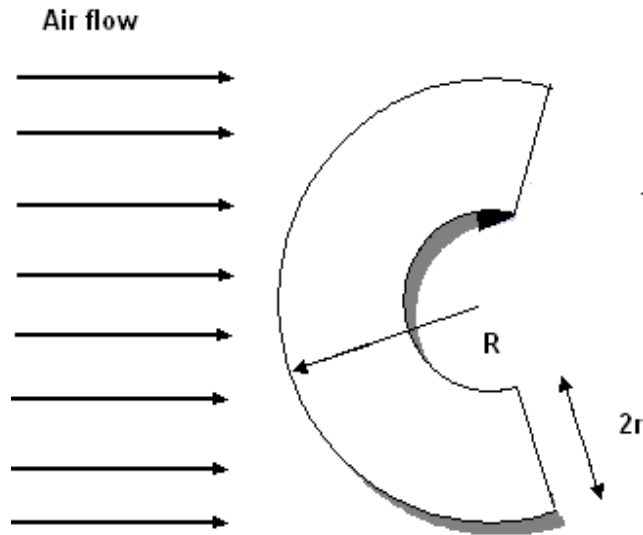


[Figure 2.2. Bicurvature geometry [21]]

- **Temperature Minimized Sweepback Concept** [21] was also proposed for S.B.L.E. geometries, where the Wall temperature decreases with increasing Sweepback, attains a minima and then starts increasing

$$h_{2D,stag} = 1.14 \cdot Pr_l^{-0.6} \cdot C_{p,l} \sqrt{\frac{\rho_l \cdot \mu_l \cdot v_\infty}{D}} \dots\dots\dots(2.1)$$

$$h_{bicurv,stag} = 1.14 \cdot Pr_l^{-0.6} \cdot C_{p,l} \sqrt{\frac{\rho_l \cdot \mu_l \cdot v_\infty}{2} \left( \frac{1}{R} + \frac{1}{r} \right)} \dots\dots\dots(2.2)$$

$$h_{SBLE} = h_{2D,stag} (v_\infty \cos \Lambda) + h_{fp} (v_\infty \sin \Lambda) \dots\dots\dots(2.3)$$

$$\left( \frac{1}{R} + \frac{1}{r} \right) = \frac{1}{R_{bicurv}} \dots\dots\dots(2.4)$$

The hypothesized geometry, based on the investigation conducted by Mahulikar [21] can be seen illustrated in Figure 2.3, which can effectively be described as

- A combination of
  - ❖ a non-axisymmetric forward stagnation region
  - ❖ Cylindrically blunt leading edges
  - ❖ a lifting body having a thick blunt delta structure

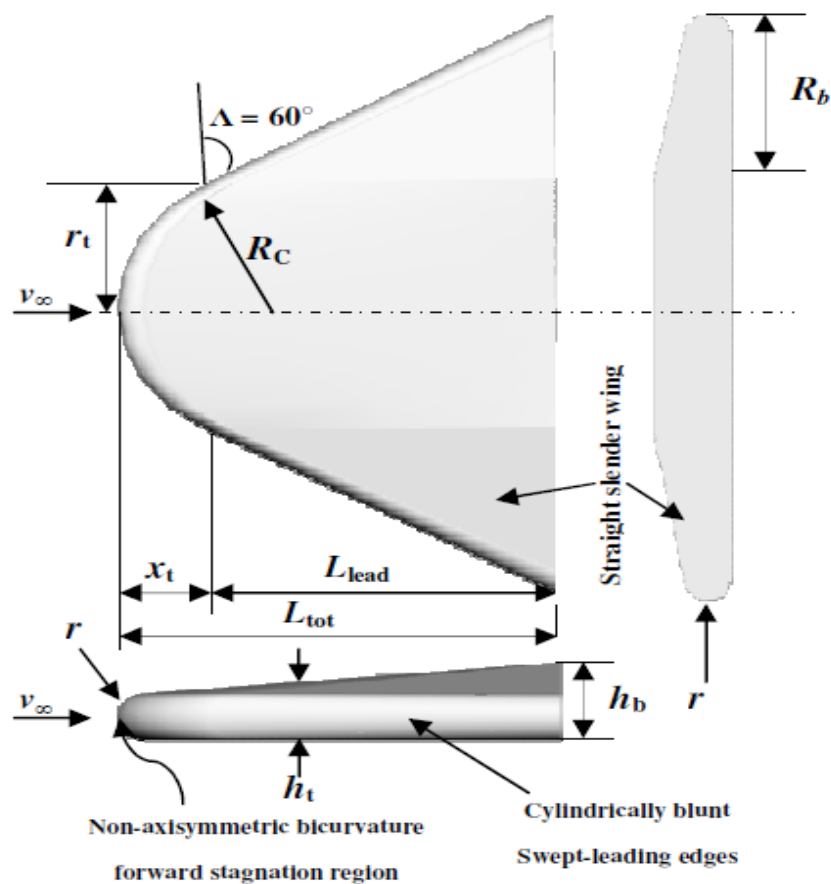


[Figure 2.3 Schematic of hypothesized delta configuration.]

➤ **Geometries for Experiments**

- ❖  $(R_c / r = 6.67)$
- ❖  $\Lambda = 15^\circ - 90^\circ$
- ❖ Constant Leading edge length

The various experimental models for the swept back leading edge

## Chapter 2: Geometric Configurations

---

geometries have been illustrated in Figure 2.4 (i)-(viii), for different  $\Lambda$  ranging from  $15^\circ$ - $90^\circ$ . The change in the aspect ratio of all the geometries with the change in  $\Lambda$  can be clearly seen.



(i)  $\Lambda = 15^\circ$



(ii)  $\Lambda = 30^\circ$



(iii)  $\Lambda = 45^\circ$



(iv)  $\Lambda = 60^\circ$



(v)  $\Lambda = 70^\circ$



(vi)  $\Lambda = 75^\circ$



(vii)  $\Lambda = 80^\circ$



(viii)  $\Lambda = 90^\circ$

[Figure 2.4 Experimental models of configurations.]

### 2.1.2 Axisymmetric Nose Delta Configuration

Another lifting body configurations for the present study was chose to be a simplified X-33 vehicle prototype, which has been the focus of study for NASA and Lockheed Martin Skunk Works' cooperative program [23,24]. The objective of the rocket-based X-33 program was to demonstrate key design and operational features for a single-stage-to-orbit (SSTO) reusable launch vehicle (RLV) for assessing the applications and technicalities of its commercial and private viability. The X-33 concept, consisted of a lifting body shape with integrated linear aerospike rocket engines meant for a flight to sub-orbital trajectory and, assessment of the aerodynamic and aerothermodynamic aspects of ascent, and re-entry phases. Later, as a consequence of increasing weight issues and sustained longitudinal instability, the program was brought to an end. The models of the present investigation were selected to be simplified model representative of the X-33 vehicle shape (shown in Figure 2.5).

The schematic of experimental model, considered for lifting body configuration, is shown in Figure 2.6 (all dimensions in mm). The lifting body consists of a blunt-nose, with leading edges swept back at an angle of  $70^\circ$ . Owing to the unavailability of key parametric features of the geometry (including the nose contours, the nose-cone area and the radius of curvature of the leading edges), the present model was considered to be a simplified one, without including any body flaps and vertical tails of the original model studied. The moment reference location for the models was taken to be 66 percent of the body length from the nose.

[Table 2.1. Reference dimensions.]

Dimension	Full-scale	0.004-scale
Ref. length	19.3 m	77.2 mm
Ref. Base length	10.98 m	43.92 mm
Ref. Nose radius	1.21 m	4.84 mm
C.G. Ref. (66%)	12.36 m	49.44 mm

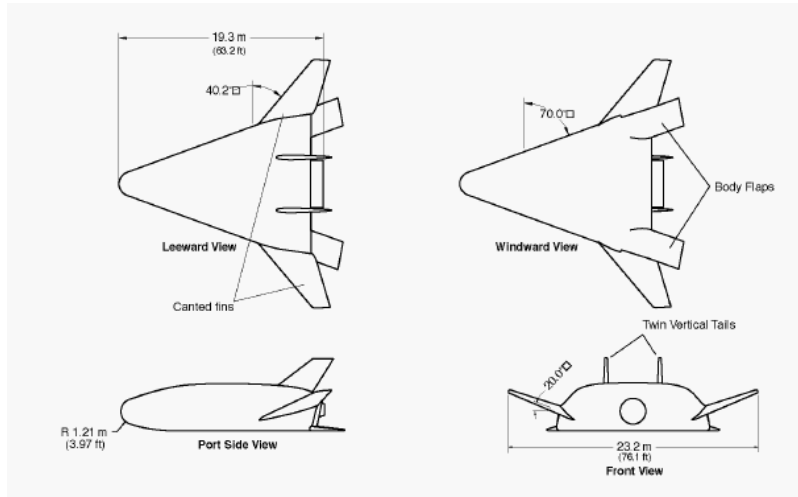


[Figure 2.5 Sketch of full-scale X-33 604B0002F/G configuration [23]]

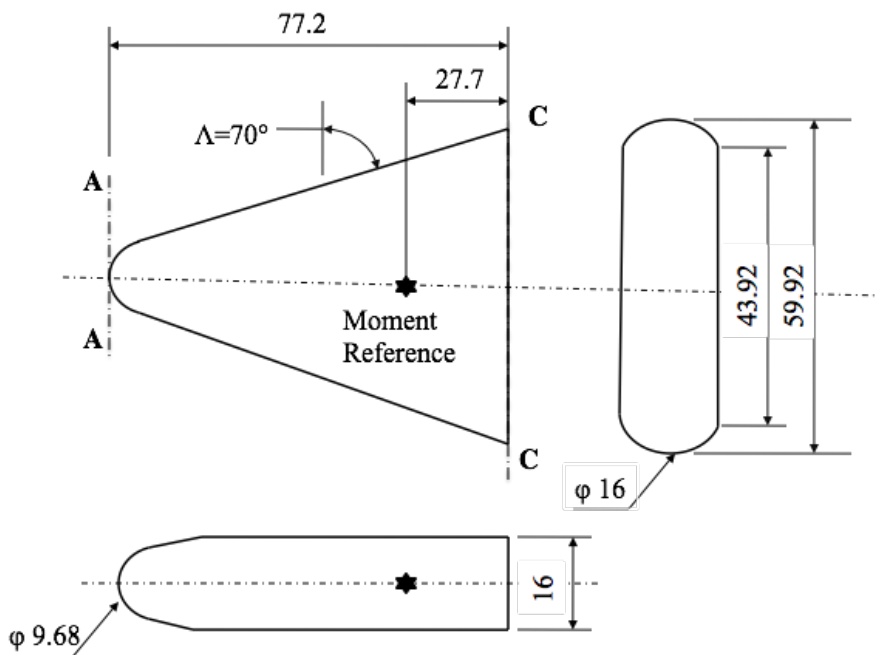


[Figure 2.6. Experimental test model (all dimensions in mm).]

## 2.2 Aerospike Technique

### 2.2.1 Non-axisymmetric Nose Delta Configuration

The representative lifting-body geometry selection for investigation was aimed at keeping in mind the conventional geometries of retiring space shuttles. Mahulikar [21] hypothesized a configuration consisting of a non-axisymmetric bicurvature stagnation surface with swept back leading edge (SBLE) having  $\Lambda$  and considering it, a similar selected base-line (reference) geometry is shown in Figure 2.1. With a large frontal stagnation area, the bicurvature geometry possesses good heat relieving properties. The dependence of  $\Lambda$  on aerodynamic drag coefficient and heat transfer has been proclaimed through experimental results (described in Section 4.1) and looking at its promising scope, the base geometry was considered to be a delta-type lifting body configuration with non-axisymmetric stagnation surface having a hemi-toroidal shape and with two cases of  $\Lambda=60^\circ$  and  $\Lambda=70^\circ$ .

#### 2.2.1.1 $60^\circ$ -Swept Leading Edge Configuration

The reference geometry without spike is shown in Figure 2.7 and with spike is shown in Figure 2.8.

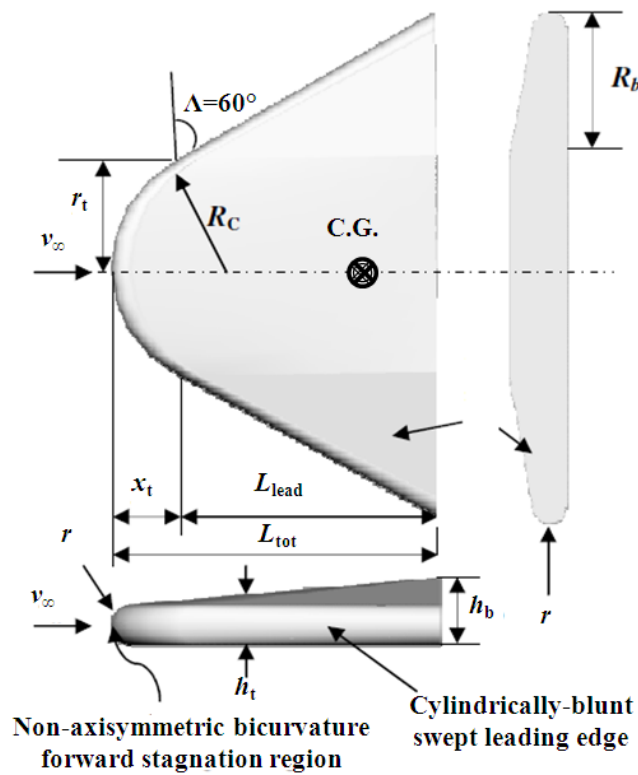


[Figure 2.7 Representative (reference) geometry.]

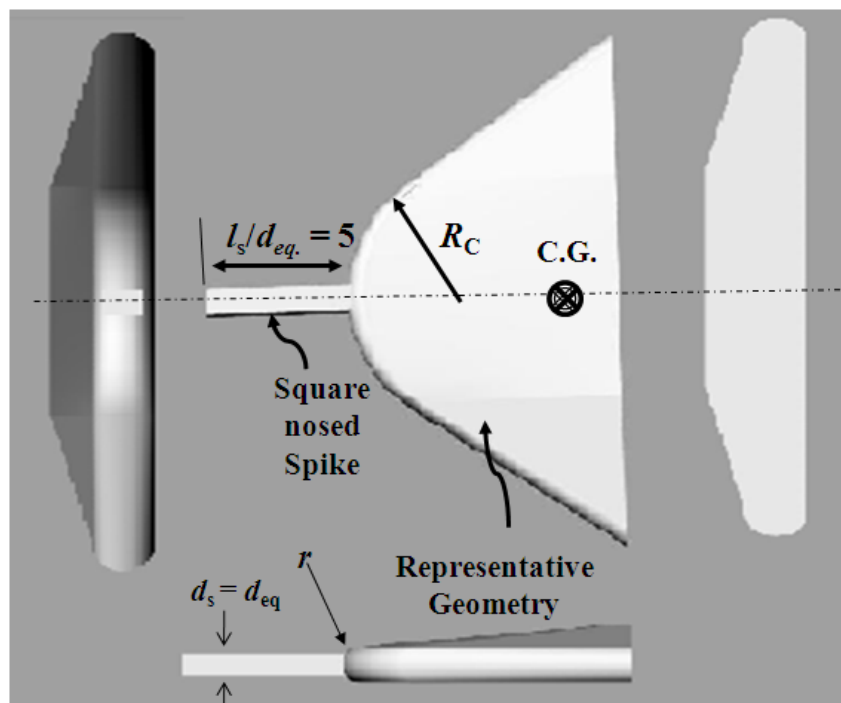


[Figure 2.8 Experimental spiked model.]

2.2.1.1.1 Aerospike-geometry considerations

With reference to the past research on use of spikes in front of axisymmetric nose area, it has been proclaimed that higher the length of the spike, larger is the size of the low-pressure vortex and eventually lower is the drag offered. For a non-axisymmetric nose, there is no reference for the use of spikes for which the equivalent nose diameter is given by  $d_{eq}$ . The value of  $d_{eq}$  for the test geometry is 5.2 mm. Keeping in mind the beneficial features of longer spike and taking into consideration the strength of the spike for the given lifting body with large volume and mass, a characteristic value of (length/nose diameter) for the spike, denoted by  $l_s/d_{eq}$  was kept at 5, i.e.  $l_s/d_{eq} = 5$  ( $l_s = 5.2 \times 5 = 26$  mm). The geometric characteristics of the aerospikes considered have been presented in Figure 2.9. Only one value of  $l_s/d_{eq}$  has been considered for the present study. Conical and hemispherical aerospikes are kept at a root diameter,  $d_s$ , of  $d_{eq}$ , whereas for a flat-faced aerospike, a specific case of square has been considered, where the side of square at its root is kept at  $d_{eq}$ . The choice of a square spike is made to have uniformity in comparison, keeping the geometric root dimension same  $d_{eq}$  as other spikes and to investigate the effect of sharp vertices in restraining the recirculation bubble near the stagnation point. The equivalent radius of curvature for the geometry considered, as hypothesized by Mahulikar, is given by

$$d_{eq} = 2 \times r_{eq} = 2 \times \left( \frac{rR_c}{r + R_c} \right) \dots\dots(3.4)$$

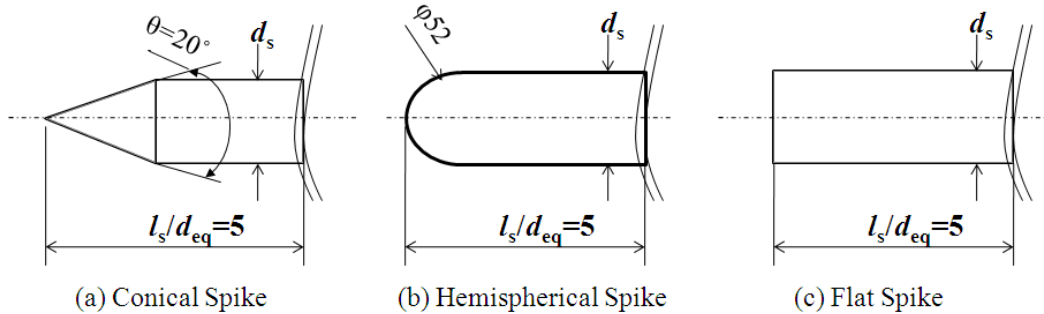


[Figure 2.9 Spike nose configuration.]

### 2.2.1.2 70°–Swept Leading Edge Configuration

The reference geometry without spike is shown in Figure 2.10.

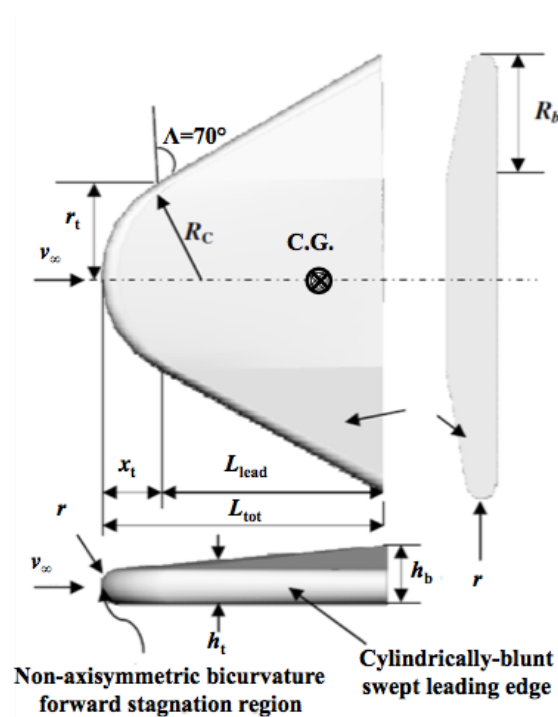


[Figure 2.10 Representative (reference) geometry.]

#### 2.2.1.2.1 Aerospike-geometry considerations

With reference to the past research on use of spikes in front of axisymmetric nose area, it has been proclaimed that longer the length of the spike larger is the size of the low-pressure rotating vortices, and eventually lowers is the drag offered. For a non-axisymmetric nose, there is no reference for the use of spikes for which the equivalent nose diameter is given by  $d_{eq}$ . The value of  $d_{eq}$  for the test geometry is 5.2 mm. Keeping in mind the beneficial features of longer spike and taking into consideration the strength of the spike for the given lifting body with large volume and mass, a characteristic value of (length/nose diameter) for the spike, denoted by  $l_s/d_{eq}$  was considered for three cases of 3, 5 and 7. The geometric characteristics of the aerospikes considered have been presented in Figure 2.11. Conical and hemispherical aerospikes are kept at a root diameter,  $d_s$ , whereas for a flat-faced aerospike, a specific case of square has been considered, where the side of square at its root is kept at  $d_{eq}$ . The choice of a square spike is made to have uniformity in comparison, keeping the geometric root dimension same  $d_{eq}$  as other spikes and to investigate the effect of

sharp vertices in restraining the recirculation bubble near the stagnation point. The equivalent radius of curvature for the geometry considered, as hypothesized by Mahulikar<sup>4)</sup>, is given by

$$d_{eq} = 2 \times r_{eq} = 2 \times \left( \frac{rR_C}{r + R_C} \right) \quad (1)$$

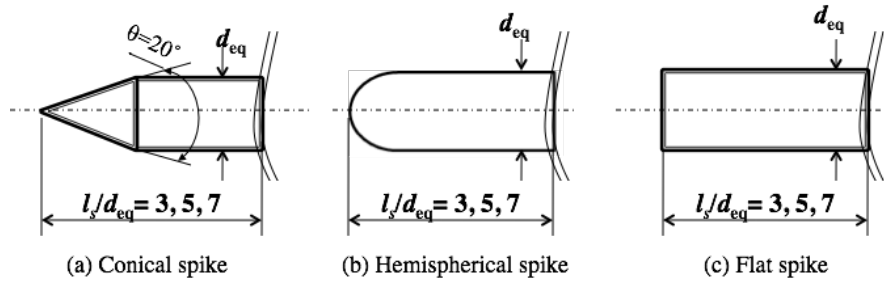


[Figure 2.11. Various spike configurations.]

The experimental lifting body model, mounted inside the wind tunnel section, has been shown in Fig. 2.12.

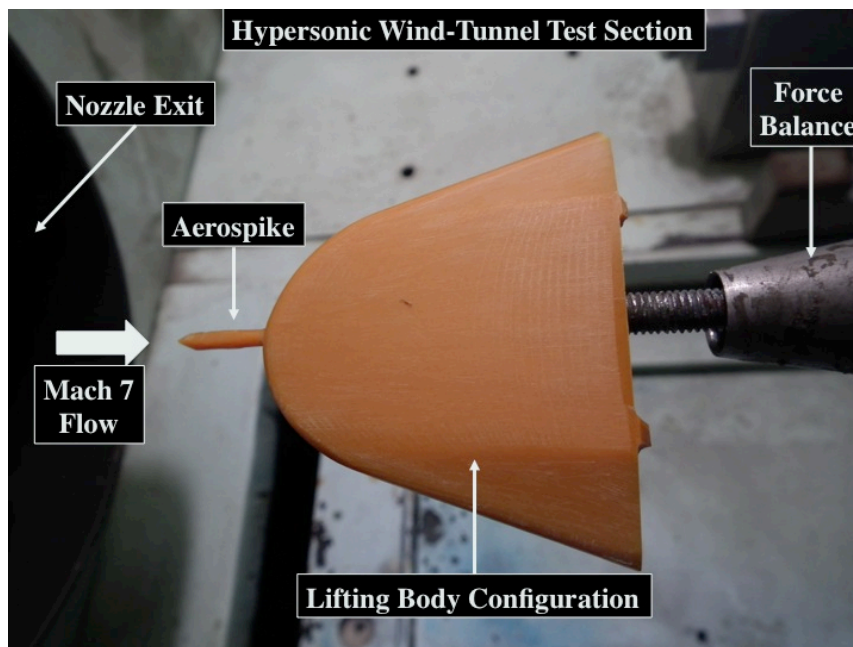


[Figure 2.12. Lifting-body model with conical spike with  $l/d_s=3$ .]

### 2.2.2 Axisymmetric Nose Delta Configuration

Figure 2.13 shows the schematic of the various spike configurations considered during the investigation, namely spikes with conical (with cone angle as  $20^\circ$ ), hemispherical and flat nose. Considering the strength for the spike with respect to the experimental model of main body, the root diameter of the spikes was fixed at about 0.15 times the nose diameter of the body. Also, the experiments were performed for three cases of varying (length of spike/body nose diameter)-ratio of 0.5, 1.0 and 1.5. Figure 2.14 shows a pictorial view of the mounted model inside the test section of the wind tunnel.

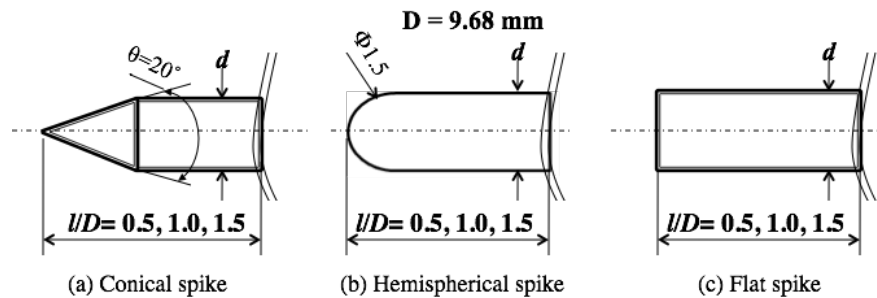


[Figure 2.13. Various spike configurations.]



[Figure 2.14. Lifting-body model with flat-nose spike and  $l/D=1.5$ .]

## 2.3 Breathing Blunt Nose Technique

### 2.3.1 Axisymmetric Nose Delta Configuration

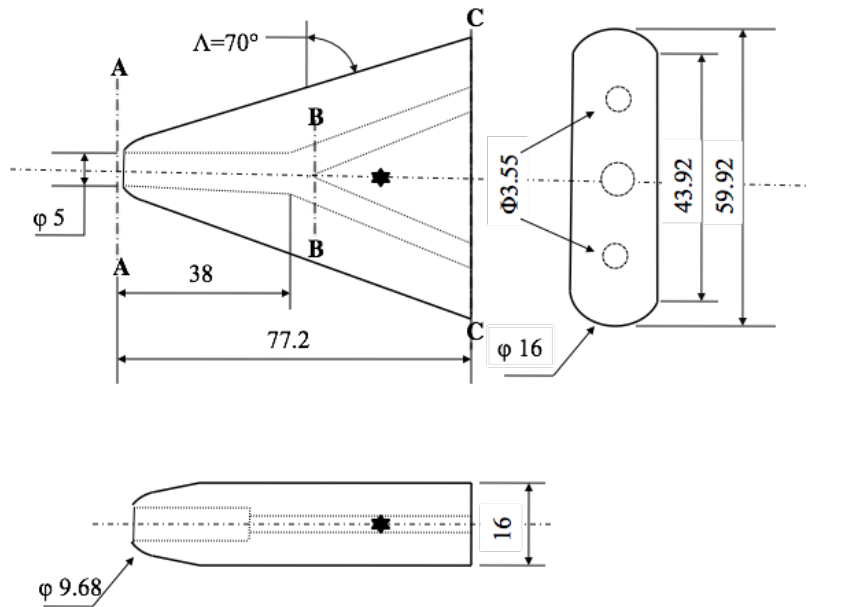
For this technique, 70° swept lifting body configuration has been considered, which has been described in Section 2.1.2.

#### 2.3.1.1 Nose-hole considerations

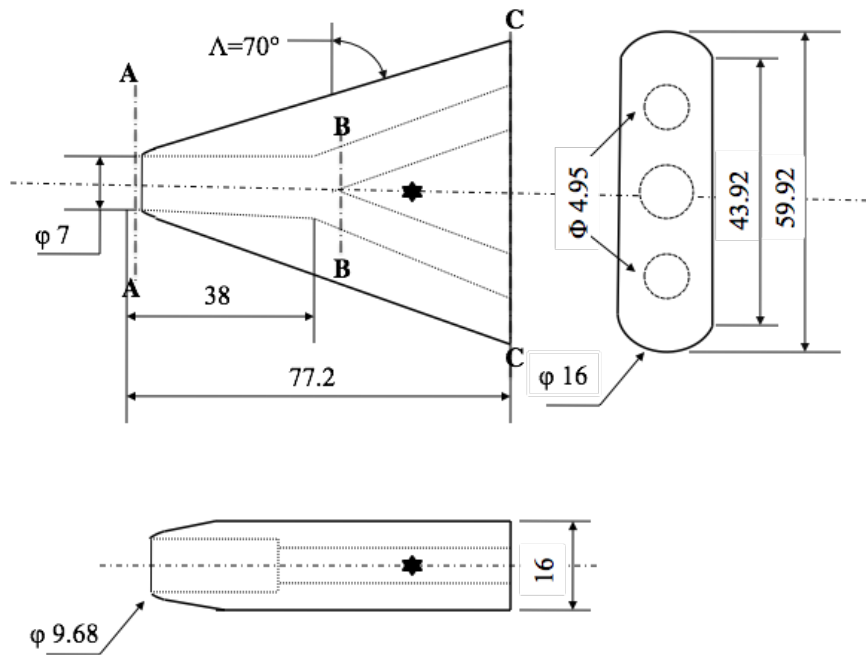
Figure 2.15 shows the schematic diagram of the experiment models considered, with holes for breathing holes, of (a) 5mm and (b) 7mm diameters, respectively (all dimensions in mm). The passage for high-pressure flow extends from the stagnation point up to 38 mm along the length of the body, after which it is divided in two sections parallel to the leading edges. The cross-sectional area of these two sections (for both cases of 5mm and 7 mm holes) is equal to the half of the nose hole area. The flow condition was assumed to be one-dimensional quasi approach from the nose to the base area, that is, the flow rate entering at the nose from specific hole diameter, remains constant at the base.

The effectiveness of the breathing blunt nose concept, with the channels designed inside the main body for the air bled at the nose, can be collectively examined as an effect of flow behavior at two locations for body without hole (location A-A at the nose and location C-C at the base, as in Figure 2.15) and at three different locations for body with  $\phi 5$  mm and  $\phi 7$  mm holes (location A-A at the nose, location B-B at the dividing section of the channel and location C-C at the base, as in Figure 2.15 (a) and Figure 2.15(b) respectively). At location A-A, the presence of shock wave and resulting high-pressure distribution over the stagnation area determines the magnitude of  $C_p$ , which is positive. At location B-B (only for models with hole at the nose), the dividing section behaves as another stagnation zone for the incoming flow bled at the nose. The drag offered at this location will be a function of the incoming flow rate, higher the flow rate; larger will be the contributing drag. At location C-C, that is, the base area, the net pressure at the wake region determines the magnitude of  $C_p$ . For the no-hole body, the low-pressure region behind the wake results in a negative  $C_p$ , but with the discharge of jets (body with holes) at the base the net pressure increases at the base consequently resulting in the increase of  $C_p$ . The mixing of the jets (mixing length) and the streamlines past the expansion fan at the base dictates the resultant pressure distribution and forms the principal phenomena for

the concept. Therefore, the flow field at these 3 different locations along the length of the body will enable the estimation of the net pressure distribution over the entire configuration.



(a) Model with  $\phi 5$  mm nose hole



(b) Model with  $\phi 7$  mm nose hole

[Figure 2.15 Experimental test model with holes (all dimensions in mm).]

Figure 2.16 and 2.17 depicts the nose end and base end views of experimental models manufactured for investigating the breathing blunt nose technique. The presence of nose holes, for breathing, and holes at base, for discharge, can be clearly seen.

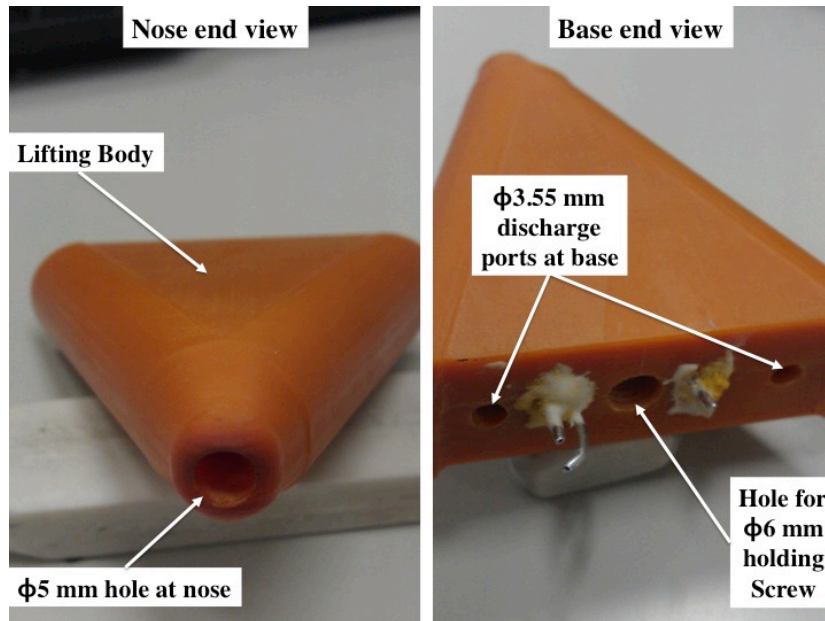


[Figure 2.16 Experimental model with  $\phi 5$  mm nose hole.]

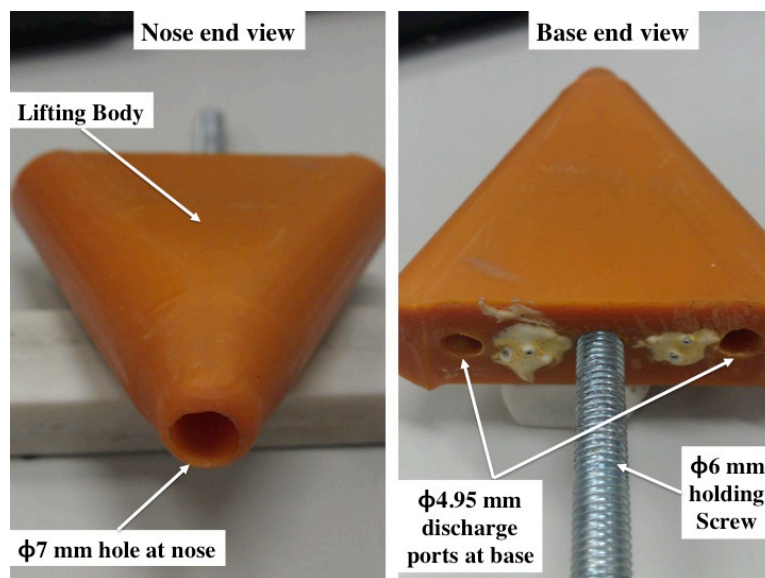


[Figure 2.17 Experimental model with  $\phi 7$  mm nose hole.]

## CHAPTER 3

# METHOD DESCRIPTION

### 3.1 Hypersonic Wind Tunnel Experiments

Hypersonic wind tunnel experiments for the present work were carried out at the Hypersonic and High Temperature Wind Tunnel situated at the Kashiwa Campus of the University of Tokyo (Kashiwa Campus).

#### 3.1.1 Hypersonic Wind Tunnel

The tunnel specifications [25] have been summarized in Table 1. With a very short startup time and turnaround time, of 1 hour providing relatively long test duration of about 60 seconds, the facility serves as a highly frequent data-capturing source. A photograph view of the wind tunnel is shown in Fig. 5. The facility can run at Mach 7 and Mach 8. The nozzle exit is 200 mm in diameter with a uniform flow core of 120 mm diameter. The stagnation pressure is around  $952 \pm 1$  kPa and the maximum attainable stagnation temperature is about 1000 K.



[Figure. 3.1 Hypersonic Wind Tunnel.]

### 3.1.1.1 Wind Tunnel Specifications

[Table 3.1 Wind Tunnel Specifications [25]]

Mach number	7, 8
Nozzle exit	200 mm diameter, free-jet, uniform flow core 120 mm diameter
Stagnation pressure	0.95 MPa
Stagnation temperature	1000 K
Mass flow rate	0.39 kg/s
Allowable Test duration	60 sec
Reservoir	5 MPa (G), 4 m <sup>3</sup> (x1)
Heater	Pebble-type + city gas burner
Exhaust	Vacuum tank (7 m dia.)

### 3.1.1.2 Test Conditions

The typical wind tunnel test conditions that were chosen to investigate the aerodynamic and thermal performance of each configuration have been summarized in Table 3.2. The tests were conducted at Mach number of 7, and the angle-of-attack was varied between  $-4^\circ$  to  $+10^\circ$ , in steps of  $1^\circ$ . The Reynolds number during the experiment was  $2 \times 10^6$  per meter of characteristic dimension. Figure 5 shows a typical time sequence of an experiment run, including the measured time-history of stagnation pressure and temperature readings and the details of respective attitude of model at each time step. The opening of the hot shut-off valve marks the starting of Mach 7 flow. The model is inserted into the flow after about 8 seconds, providing the interval for the flow to get stabilized, after which, the pre-decided variation of attitude of the model is controlled. On the completion of the desired attitude variations for the expected time-span, the model is retracted. Each test run time was around 36 seconds. The data obtained from the wind-tunnel tests include six-component force and moment readings on the breathing blunt nose of the model and the flow-visualization data.

[Table 3.2. Experimental test conditions.]

Mach number	7
Stagnation pressure	950 kPa
Stagnation temperature	480-580 K
Test duration	46 sec
Angle of Attack	-4° to 10°

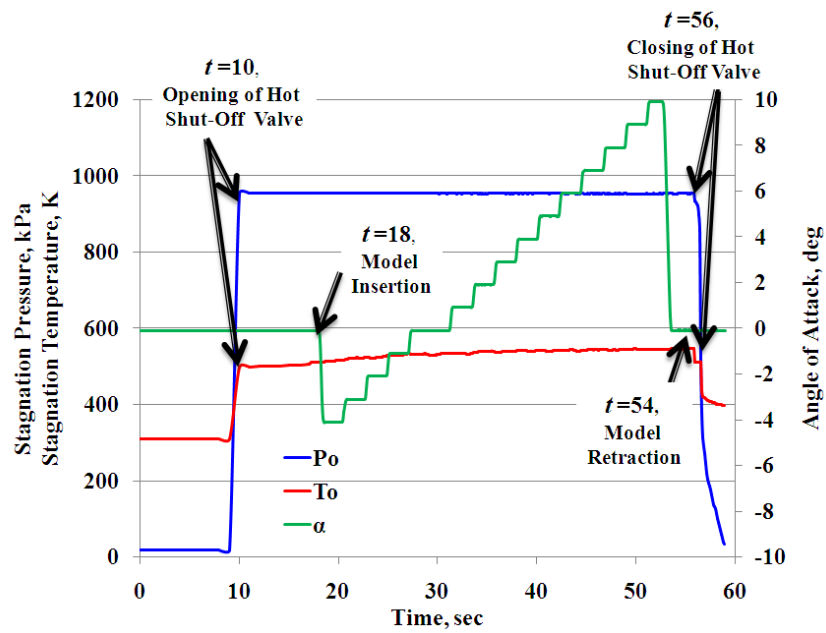


[Figure 3.2. Typical time-sequence.]

### 3.1.1.3 Instrumentation

#### 3.1.1.3.1 Model Manufacturing

The test models for various experiments were manufactured from Bakelite™ material (having good mechanical strength and thermal resistance properties) using PC-controlled Modela MDX-504A (Roland DG Corporation) rapid-prototyping machine, available onsite in the wind tunnel facility. Figure 3.3 shows the installed rapid-prototyping machine, which is connected to laptop with a compatible software to read the three-dimensional drawings and process them towards manufacturing.

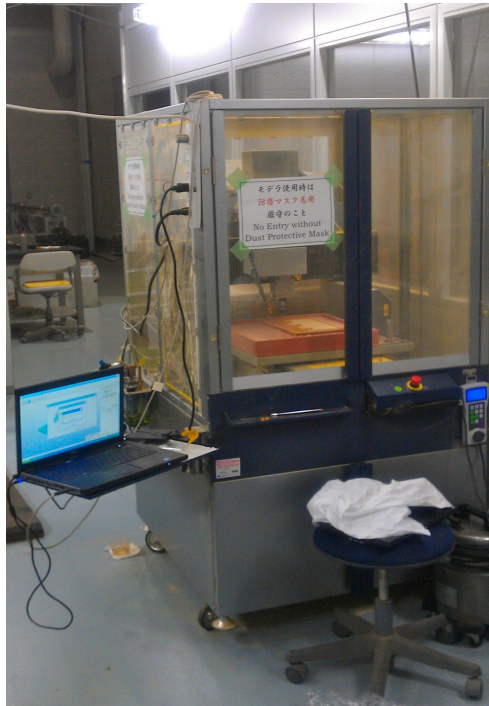


[Figure 3.3 Rapid-prototyping machine]

### 3.1.1.3.2 Force measurements

Pre-calibrated six-force strain gauge balance system, connected with a data recorder (frequency = 10 samples/second), was setup for measuring the aerodynamic forces during the complete run of the experiment. Each model was fixed using a  $\phi 6$  mm screw rod and is attached to the force-measuring sting mounted in the test-section of the hypersonic wind tunnel. Figure 3.4 illustrates the six-strain gauge force balance system and Figure 3.5 depicts the data recorder system.



[Figure 3.4. Six-strain gauge force balance system.]



[Figure 3.5. Data recorder system.]

### 3.1.1.3.3 Heat Transfer Measurements

An Infrared (IR) camera (CHINO Model TP-L0225EN), with center measurement wavelength of  $10\ \mu\text{m}$ , measurement view angle of  $25^\circ \times 25^\circ$  and temperature measurement range from  $-20\ ^\circ\text{C}$  to  $300\ ^\circ\text{C}$  (temporal resolution = 1 picture/second, spatial resolution =  $9.1\ \text{mrad}$  and temperature resolution =  $0.5^\circ\text{C}$ ) was installed inside the test-section in order to generate a 2-dimensional instantaneous temperature distribution over the geometry, throughout the experimental run. Figure 3.6 shows a typical TP-L series thermal imaging sensor used for the experiments.



[Figure 3.6 TP-L series thermal imaging sensor [26]]

#### 3.1.1.3.4 Schlieren System

Flow visualization was carried out, by means of a single-pass schlieren technique. The items of the system includes xenon lamp power supply (model XB10201 AA-A), two parabolic mirrors, a horizontal knife edge and a SONY CCD-IRIS color video camera (model DXC-107A, at a frame rate of 30 fps and a resolution of 768 x 494 pixels), to accurately capture photographs for examining flow-field features including the shock re-attachment characteristics for various configurations, with a video camera to record the movements of the geometries during the experiment to assess any possible misalignment during the wind-tunnel operation. The two recording cameras are connected to a distant computer, aided with monitor and storage device, via analog A/V connectors. Figure 3.7 depicts xenon lamp and reflecting mirror, Figure 3.8 depicts the knife-edge section and video source and Figure 3.9 shows a typical model setup inside test section.



[Figure 3.7. Xenon lamp and reflecting mirror.]



[Figure 3.8. Knife-edge section and video source.]

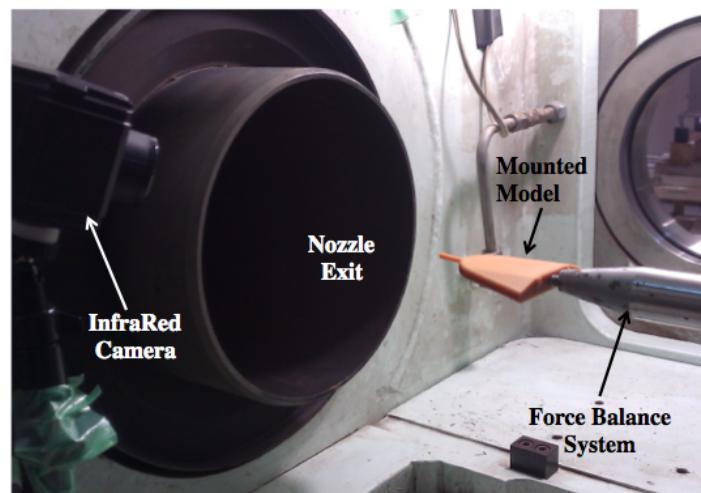


[Figure 3.9. A typical model setup inside test section.]

### 3.1.1.4 Experimental Data Uncertainty

The uncertainty in the measurement of the force results in the hypersonic wind tunnel has been estimated to be within  $\pm 5$  percent for all the aerodynamic forces and moments. This has been depicted in respective force coefficients charts. Also, owing to high volumetric efficiency of the model compared to mounting sting column, the models during the experiments suffered a slight negative pitching moment resulting in the decrease of positioned angle of attack. Therefore, the actual angle of attack values was estimated at various places, by subtracting the angle of deflection of the model

(measured from Schlieren pictures) from the set value, and considered for appropriate and corresponding force coefficient estimation and plotted in the charts.

## CHAPTER 4

# RESULTS AND DISCUSSIONS

### 4.1 Non-axisymmetric Nose Delta Configuration

The results of the experimental investigation, performed at Kashiwa Hypersonic and High Temperature Wind Tunnel, at Mach 7, are summarized under the following sections: -

#### 4.1.1 Schlieren visualization

The Schlieren videos were captured throughout the conduct of the experiments for all the geometries with the help of Schlieren Camera. Figure 4.1 shows a typical picture recorded for the geometry with  $\Lambda=70^\circ$  at  $\alpha=0^\circ$ . It can be seen that a Bow Shock stands in front of the nose of the geometry.

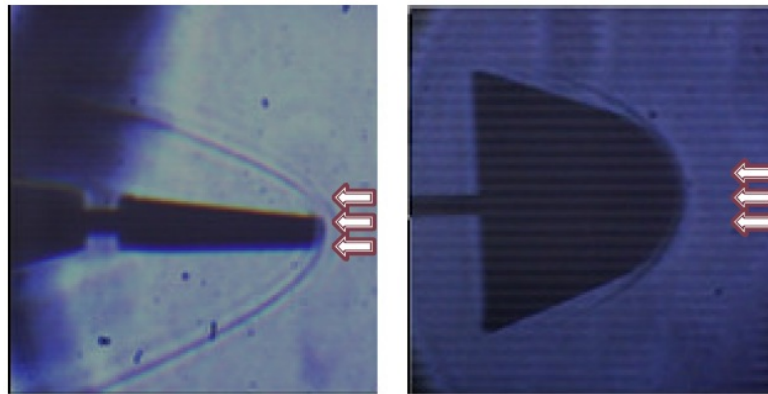


[Figure 4.1 Schlieren picture for  $\Lambda=70^\circ$  at  $\alpha=0^\circ$ ]

#### 4.1.2 Force Measurements Results

Instantaneous aerodynamic characteristics were analyzed at Mach 7 for the all the configurations and have been plotted as graphs for the  $C_L$ ,  $C_D$  and (*Lift/ Drag*) variation with respect to the Angle of attack ( $\alpha^\circ$ ).

i) Figure 4.2 represents  $C_L$ -variation with  $\alpha$  over the range  $-10^\circ$  to  $+10^\circ$ .  $C_L$  has been evaluated based on *planform area* for the configuration. On observing the graph, it can be inferred that  $C_L$  achieves a maxima for  $\Lambda=70^\circ$ , owing to small aspect ratio and a significant contribution from a large equivalent fuselage and wing area (that is

planform area). Moreover, as a result of non-axisymmetric design, although  $C_L$  is negative at  $\alpha=0^\circ$  unlike conventional geometries representing a *negative-lift geometry*. For  $\Lambda=60^\circ$ ,  $75^\circ$  and  $80^\circ$ , the  $C_L$ -variation provides a wide spectrum of  $\Lambda$  for further design modifications.

ii) Figure 4.3 represents  $C_D$ -variation with  $\alpha$  over the range  $-10^\circ$  to  $+10^\circ$ .  $C_D$  has been calculated based on *planform area* for the configuration. On observing the graph, it is inferred that with increase in  $\Lambda$ ,  $C_D$  decreases constantly, achieves a minima for  $\Lambda=90^\circ$ . With increasing  $\Lambda$ , the leading edges tend to get more restrained inside the Mach cone resulting in the decrease in  $C_D$ , which is a consequence of the decrease in obstruction offered to the flow by the extended wings' reference area of the delta geometry. At  $\Lambda=90^\circ$ , owing to no wing condition, poses minimum obstruction to the flow.

iii) With  $C_L$  tending to increase and  $C_D$  tending to decrease at higher  $\alpha$  (as is evident from Figure 4.2 and Figure 4.3), it provides a possible scope for further study to conduct experiments at significantly high values of  $\alpha$  to analyze the aerodynamic performance. The decrease in  $C_D$  at higher  $\alpha$ , unlike conventional geometries, is attributed to its non-axisymmetric nature where the increase in  $\alpha$  results in possible detachment of shock wave from the upper surface of the geometry, responsible for offering maximum drag, and ultimately results in decrease in net obstruction offered to the flow.

iv) Figure 4.4 shows the (*Lift/ Drag*) variation with  $\alpha$  for various configurations. Although,  $(L/D)_{MAX}$  condition is obtained for  $\Lambda=70^\circ$ , the range with  $\Lambda=60^\circ$ - $80^\circ$ , also provides a reasonable value for overall aerothermal design consideration, and selection of the configuration at high swept back

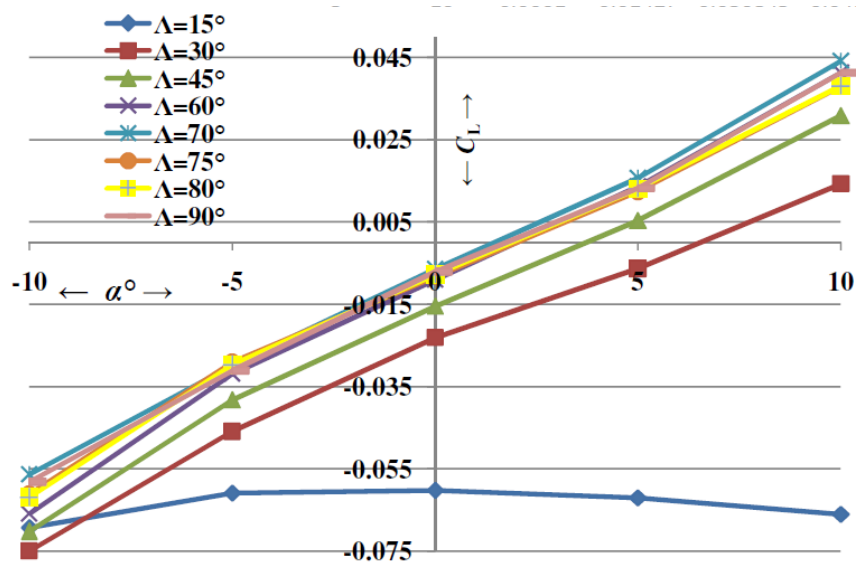


[Figure 4.2  $C_L$  v/s  $\alpha$  variation for various  $\Lambda$ ]

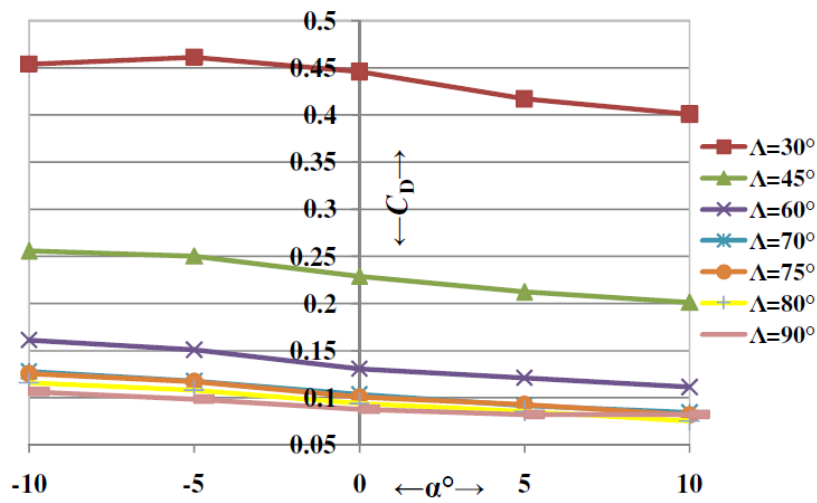


[Figure 4.3  $C_D$  v/s  $\alpha$  variation for various  $\Lambda$ ]

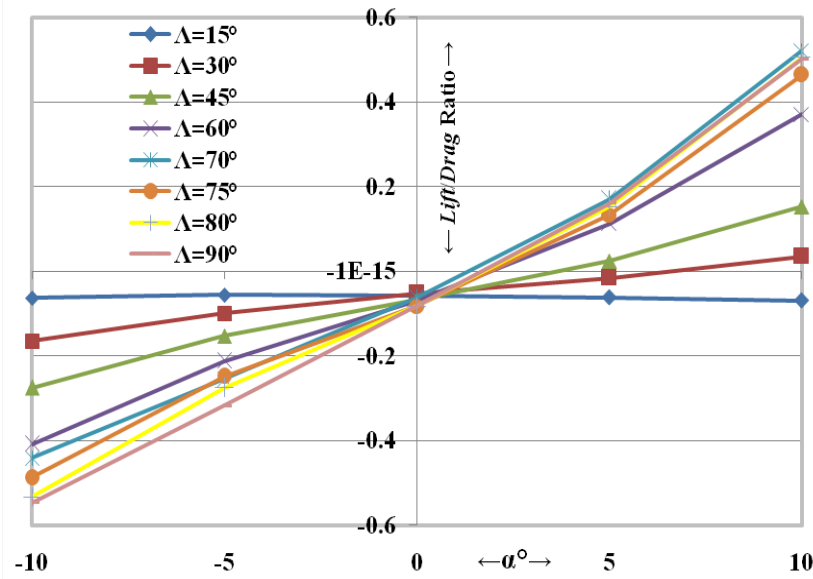


[Figure 4.4 (*Lift/Drag*) ratio v/s  $\alpha$  variation for various  $\Lambda$ ]

### 4.1.3 Heat Transfer Measurement Results

In order to study the aerodynamic heating performance of geometries with different  $\Lambda$ , instantaneous two-dimensional temperature distribution over the geometries has been generated by employing the Infra-Red Camera, installed inside the test chamber, as shown in Figure 4.5 for  $\Lambda=70^\circ$  at  $\alpha=0^\circ$ . The data is stored as an  $x$ - $y$  distribution of temperature ( $^\circ\text{C}$ ) in the system and the results have been plotted as instantaneous wall temperature v/s dimensionless parameter ( $x/L$ ), where  $x$  runs along  $L$  on the leading edge, for different  $\Lambda$  and are discussed as follows: -

- i) Figure 4.6 depicts the heat transfer plot (in terms of Stanton number) against  $x/L$  variation for various  $\Lambda$  at  $\alpha=0^\circ$ . With increase in  $\Lambda$ , the wall temperatures goes on decreasing, achieves a minima at  $\Lambda=70^\circ$  and then increases again. This is attributed to decrease in heating due to  $h_{2-D,stag}$  component and increase in  $h_{fp}$  heating as explained in equations (2.1-2.3), with increase in  $\Lambda$  thereby reaching an optimum value corresponding to temperature minimized condition and then again increases.  $\Lambda=70^\circ$  and  $\Lambda=75^\circ$  offers a range for optimization, signifying that minimum wall temperatures for current configuration lies between these values of  $\Lambda$ .
- ii) Figure 4.7 illustrates the instantaneous two-dimensional temperature distribution over the geometries, for different  $\Lambda$  at  $\alpha=10^\circ$ , and Figure 4.8 depicts the heat transfer plot against  $x/L$  variation, which indicates the presence of higher and an optimum  $\Lambda$

for further design considerations.

(iii) Figure 4.9 illustrates the instantaneous two-dimensional temperature distribution over the geometry  $\Lambda=70^\circ$  at different  $\alpha$  ( $-10^\circ$  to  $+10^\circ$ ) and Figure 4.10 shows heat transfer plot against  $x/L$  for. It can be observed that with the increase in  $\alpha$ , the wall temperature variation follows a similar trend along the leading edge and increases in magnitude.

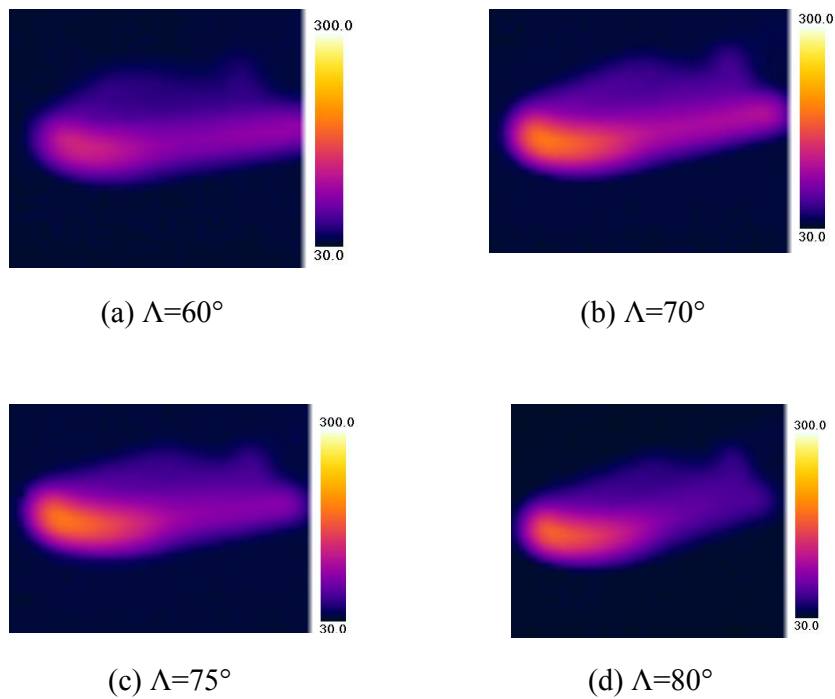


[Figure 4.5 Instantaneous temperature ( $^\circ\text{C}$ ) distribution at  $\alpha=0^\circ$  for different  $\Lambda$ ]

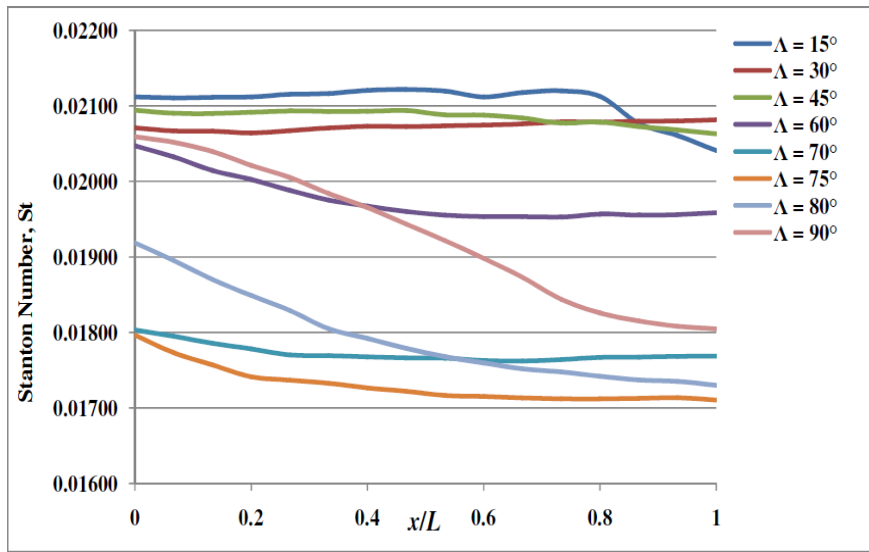


[Figure 4.6 Heat transfer along leading edges with  $x/L$  for different  $\Lambda$  at  $\alpha=0^\circ$ ]

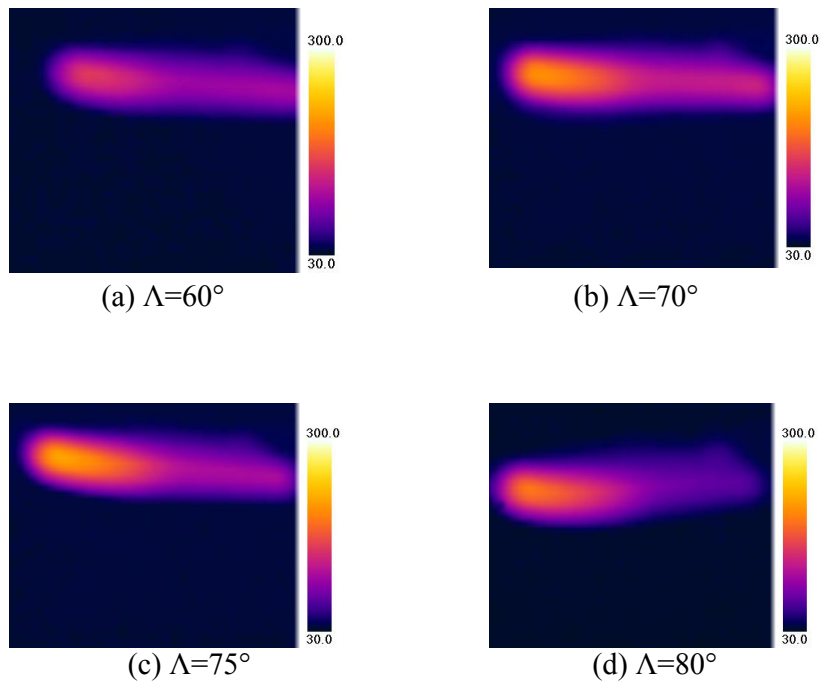


[Figure 4.7 Instantaneous temperature ( $^\circ\text{C}$ ) distribution at  $\alpha=10^\circ$  for different  $\Lambda$ ]

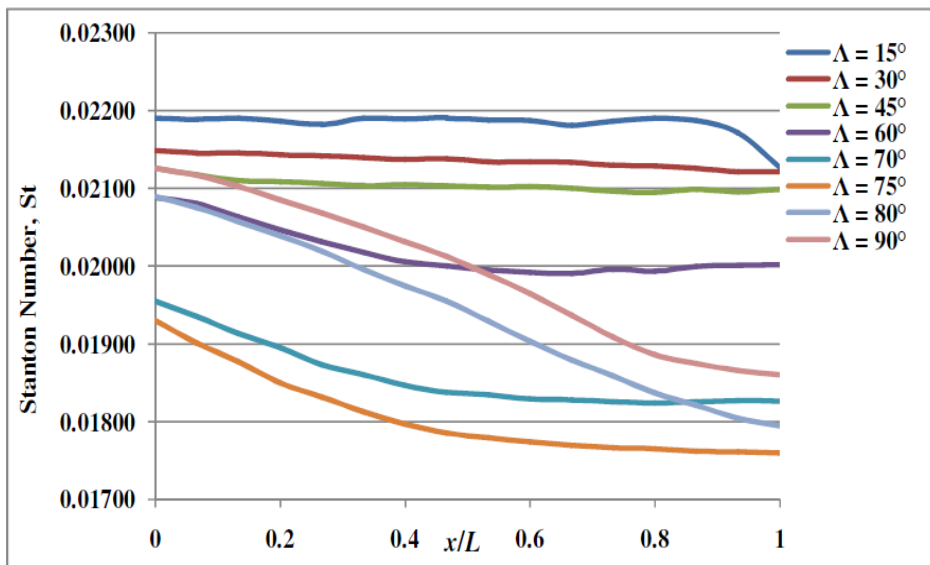


[Figure 4.8 Heat transfer along leading edges  $x/L$  variation for various  $\Lambda$  at  $\alpha=10^\circ$ ]

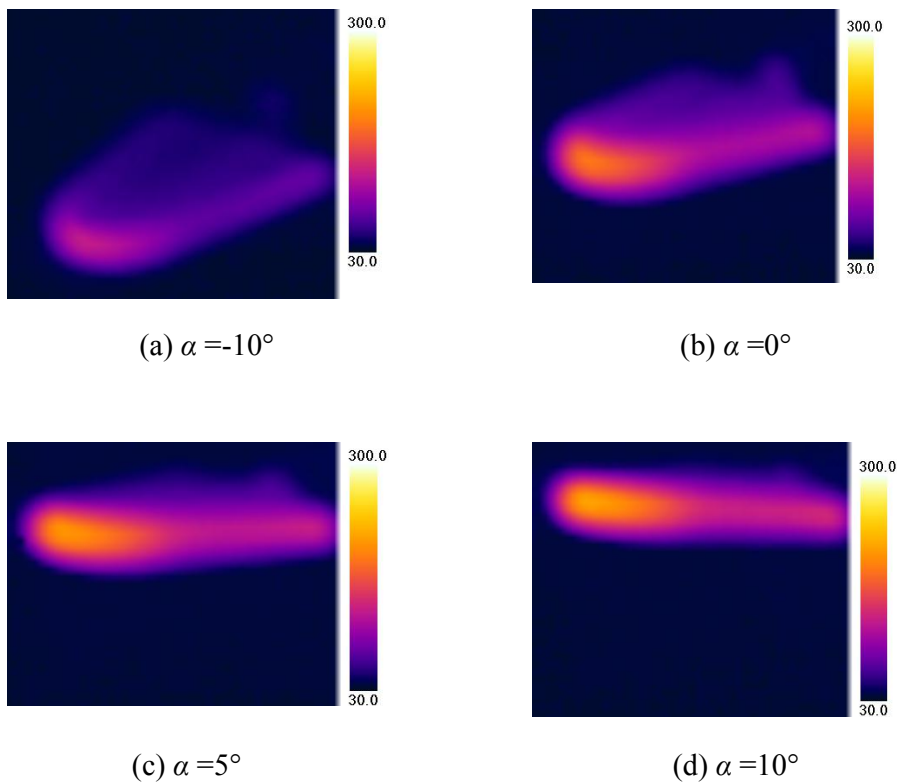


[Figure 4.9 Instantaneous temperature ( $^\circ\text{C}$ ) distribution for  $\Lambda=70^\circ$  at different  $\alpha$ ]

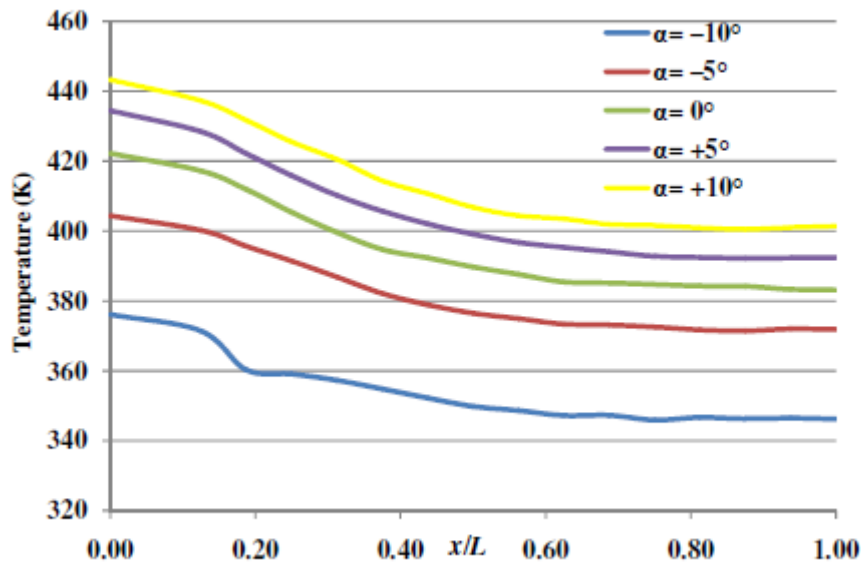


[Figure 4.10  $T_{\max}$  v/s  $x/L$  variation for  $\Lambda=70^\circ$  at different  $\alpha$ ]

## 4.2 Aerospike Investigation

### 4.2.1 Hypersonic Wind Tunnel Investigation

The experiments were performed at the Hypersonic and High Temperature Wind tunnel (specifications mentioned in Table 3.1) situated at the University of Tokyo (Kashiwa campus), with a set of predetermined test conditions as summarized in Table 3.2.

#### 4.2.1.1 Non-axisymmetric Nose Delta Configuration

The delta configuration with a toroidal shape non-axisymmetric nose has been described in Section 2.2.1 of Chapter 2, having leading edges swept at an angle  $\Lambda$  to the direction of flow.

##### 4.2.1.1.1 $60^\circ$ Swept Leading Edge Configuration

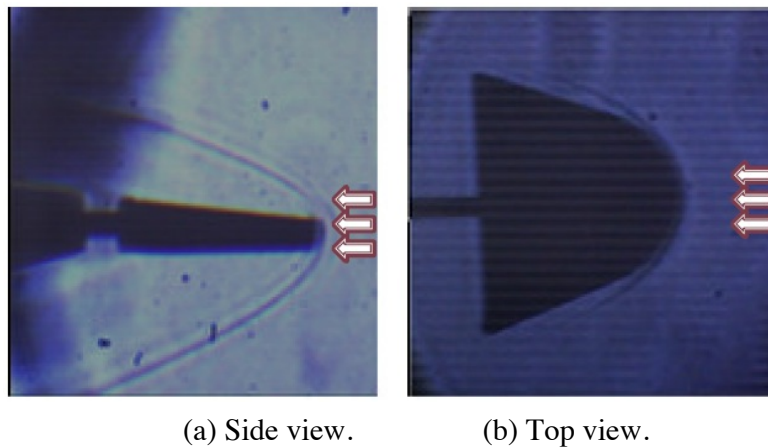
The geometry considered in this investigation has its leading edges swept at an angle of  $60^\circ$  to the direction of wind, as described in Section 2.2.1.1.

#### 4.2.1.1.1 Schlieren Visualization

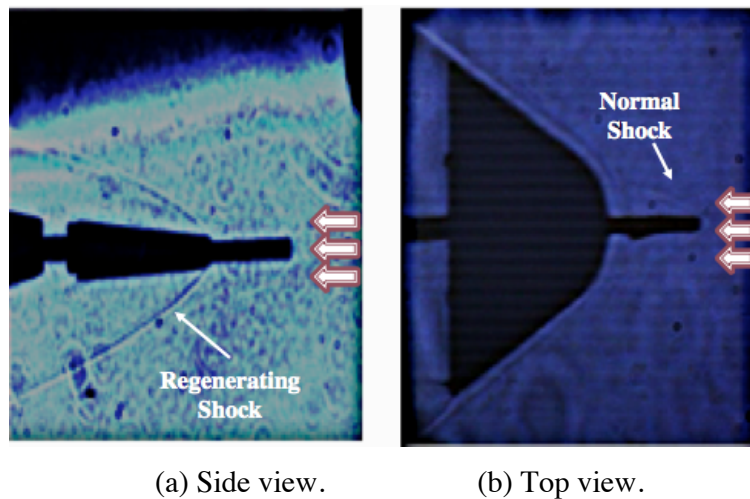
Figure 4.11 shows the schlieren pictures for the reference geometry without spike from side and top view and Figure 4.12-4.14 shows the schlieren pictures of geometry with flat, hemispherical and conical spikes of  $l_s/d_{eq}=5$  at  $\alpha=0^\circ$  respectively. As discussed before, the extremely thin layer of foreshock emerging from the nose of the spike can be observed on carefully looking at the schlieren pictures. The corresponding flow direction in these pictures is from right-to-left. Owing to the non-axisymmetric nature of the nose, it becomes mandatory to capture the flowfield from both views (side and top). It can be seen from Figure 4.11-4.14 that the shock is asymmetric in nature. For a no-spike body (Figure 4.11), the bow shock is positioned detached from the nose. The presence of a spike on the nose of the body shifts the position of the shock onto the spike-nose. For a conical spike, an oblique shock wave, standing close to the nose, is generated while for hemispherical and flat spike, the shock wave stands detached. The high-pressure regime from the large nose-area of the body is transferred onto the small nose-area and a weak oblique shock is observed on the body. The hemispherical and flat spikes generate weak detached and normal shocks respectively (as is evident from Figure 4.12-4.13(b)) and a separation zone (which is a function of  $l_s/d_{eq}$ ); reattaching downstream on the main body with the recompression shock. Figure 4.12-4.14(a) illustrate a recompression shock originating from the main body. The fact of reattachment of the shock on the main body is supported by elevated temperatures as visible from  $T_w/T_0$ -variation in Figure 4.22 and  $C_h$ -variation in Figure 4.23 and is also recorded as bright spots on the body nose by IR camera in Figure 4.24(b).

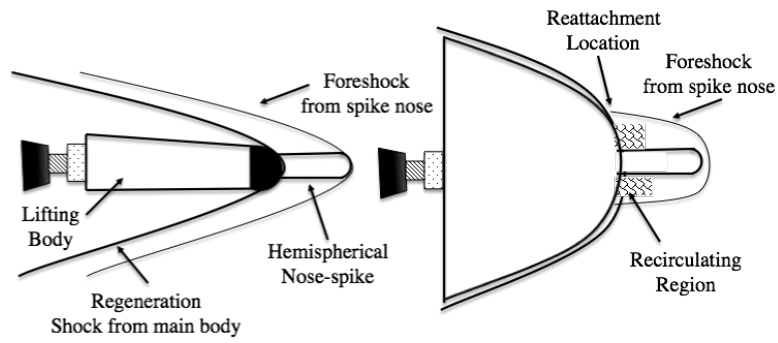
Figure 4.15 shows the schlieren pictures (side view) of no-spike body for  $\alpha=4^\circ$  and  $\alpha=10^\circ$ . Figure 4.16 shows the schlieren pictures (side view) of flat faced spike body for  $\alpha=4^\circ$  and  $\alpha=10^\circ$ . With increasing  $\alpha$ , the stream-tubes encounter an increase in area on the leeward side thereby facing isentropic expansion, turning towards the flow, and hence resulting in a pressure drop. On the contrary, the windward side witnesses a compression due to reduction in area, with the stream tubes turning away from the flow. The recirculation zone formed in the vicinity of the body nose and the flow separation initiated from the spike nose seems to be a function of  $l_s/d_{eq}$ ,  $\alpha$  and nose-spike configuration. With the increase in  $\alpha$ , the recirculation bubble formed near

the stagnation point and spike root is pushed on the leeward side, resulting in a positive pressure gradient in the upward direction, thereby maintaining the linear increase in  $C_L$ , as is clear from Figure 4.17. Consequently, with the movement of the bubble from the stagnation point, the axial force component acting on the body becomes stronger due to increase in the pressure near the spike root. This results in suppressing of the decrease in  $C_D$ , with the introduction of the spike, as can be observed from Figure 4.18.



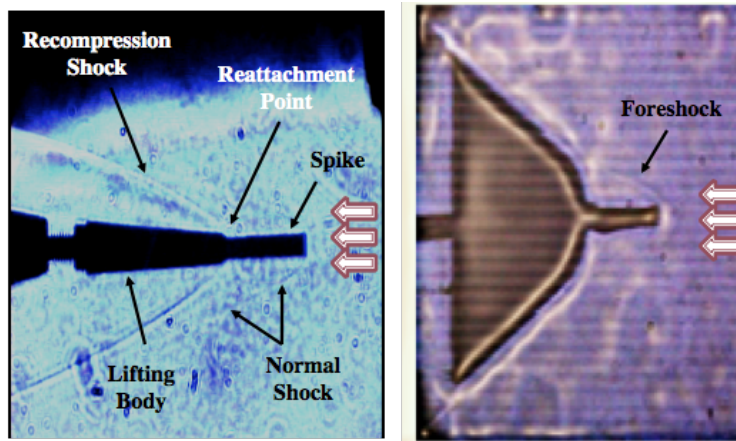
[Figure 4.11 Schlieren pictures for no-spike body at  $\alpha=0^\circ$ .]





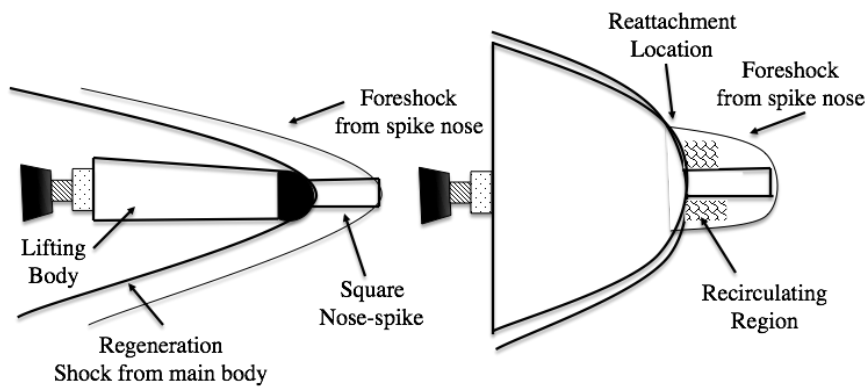
(c) Schematic representation.

[Figure 4.12. Schlieren pictures and schematic diagram for hemispherical spike at  $\alpha=0^\circ$ ]



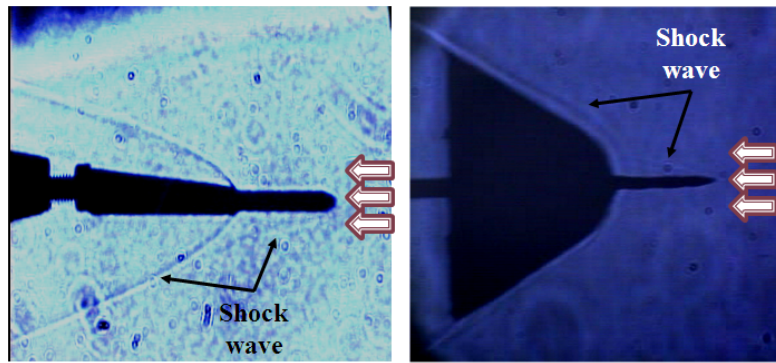
(a) Side view.

(b) Top view.



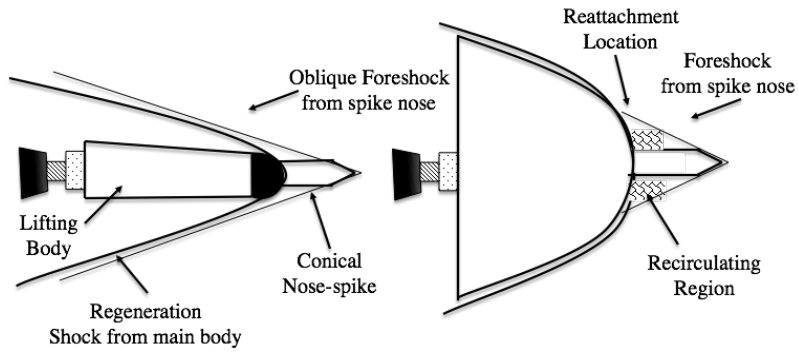
(c) Schematic representation.

[Figure 4.13. Schlieren pictures and schematic diagram for flat faced spike at  $\alpha=0^\circ$  .]



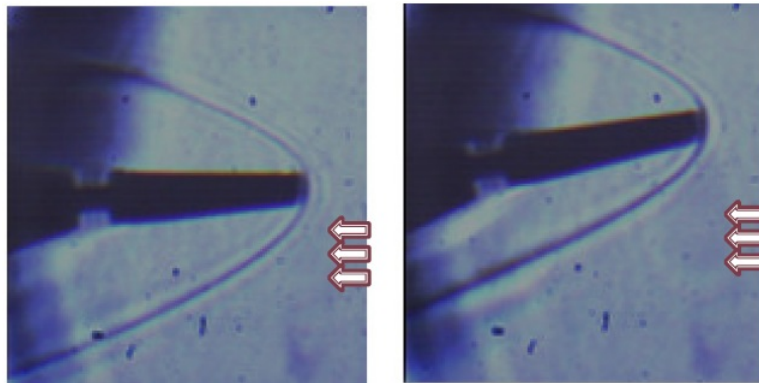
(a) Side view.

(b) Top view.



(c) Schematic representation.

[Figure 4.14. Schlieren pictures and schematic diagram for conical spike at  $\alpha=0^\circ$ ]



(a) At  $\alpha=4^\circ$ .

(b) At  $\alpha=10^\circ$ .

[Figure 4.15. Schlieren pictures (side view) for no-spike body.]

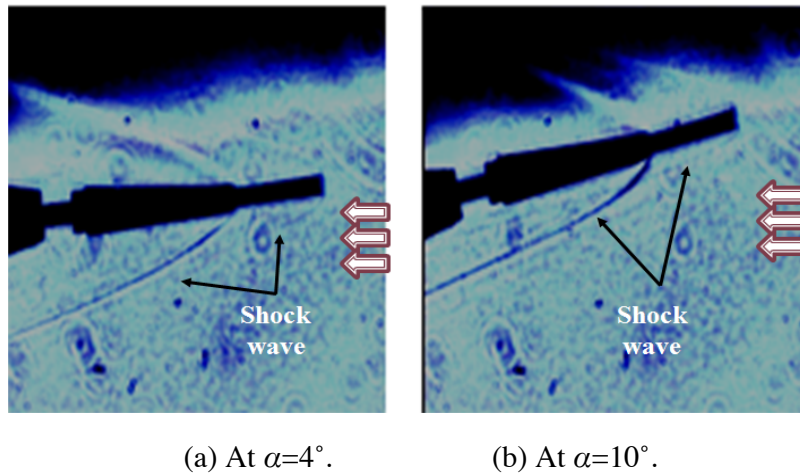


[Figure 4.16. Schlieren pictures (side view) for flat-faced spike.]

#### 4.2.1.1.2 Force Measurement Results

The aerodynamic measurements have been performed using strain gauge balance. The results have been summarized as follows: -

- a) Figure 4.17 and 4.18 show the measured  $C_L$  and  $C_D$ -variation with  $\alpha$  for various spikes. The increase in  $C_L$  and decrease in  $C_D$ , being expected advantages on introducing spike, can be analyzed from the plots. It can be observed that for flat and hemispherical spike,  $C_L$  continues to increase linearly with increasing  $\alpha$  and the maximum increase stands out at  $\alpha=4^\circ$  over the reference geometry without spike, falls with increasing  $\alpha$ , but still remains beneficial for use at high angles. The reason for this seems to be that the low-pressure recirculation bubble inside the weak shock envelope moves downstream above the leeward side of the vehicle body, thereby increasing the positive pressure gradient in the upward direction. With the introduction of a conical-nose spike, the weak foreshock emanating from the nose stays closer to the leeward and windward surface (as clear from Schlieren picture), and the geometry being asymmetric, the pressure flow field is affected. The baseline positive pressure over the nose is aggravated (more than the basic geometry) with the weak foreshock thereby decreasing  $C_L$  at  $\alpha=0^\circ$ . With the increase in  $\alpha$ , the effect due to the generated small recirculation region, near the spike root, comes into picture and  $C_L$  increases monotonically. Moreover,  $C_D$  decreases with the introduction of spike confirming the existence of a low-pressure region ahead of the nose. It can be seen that drag reduction occurs

at lower  $\alpha$  for hemispherical and flat aerospikes with  $C_{D,\min}$  occurring at  $\alpha=0^\circ$ , as compared to a no-spike body. In spite of marginal increase in  $C_D$  at higher  $\alpha$  due to flow separation, it is still advantageous to use. This might be partially due to enhanced flow separation beyond  $\alpha=4^\circ$ . However, with the increase in  $\alpha$ , the flow above the leeward surface encounters expansion thereby decreasing the pressure. For the conical nose spiked model, as observed from Fig. 4.17-4.18, the approaching streamline of the flow gets deflected and remains close to the spike, thereby creating an extremely narrow zone of low pressure region, resulting in lesser drag reduction as compared to hemispherical and flat spikes. The related flow physics needs to be analyzed in detail by employing numerical codes.

- b) Figure 4.19 shows Lift/Drag-variation with  $\alpha$  for various spikes. Lift/Drag-ratio increases linearly with  $\alpha$  with the maximum increase for the flat and hemispherical respectively at  $\alpha=4^\circ$ . Although the Lift/Drag-Ratio continues to increase even at higher  $\alpha$  (registering an increase for all spike configurations), the percentage-increase over a no-spike case gets suppressed, as a consequence of increase in drag from possible flow separation.
- c) Figure 4.20 shows  $C_m$ -variation, evaluated at C.G. (assumed to be at 75% of vehicle length), with  $\alpha$  for various spikes. It can be inferred that the use of spike doesn't significantly affect the trend in the measured values of  $C_m$ , that is, the  $dC_m/d\alpha$  trend (for longitudinal static stability) is measured to be positive, same as base geometry. At lower  $\alpha$ , introduction of spike brings stability to the test configuration (as observed from Figure 4.20 till  $\alpha=5^\circ$ ) beyond which, owing to large normal force component  $C_m$  increases for hemispherical and flat spikes. Although the magnitude is very small, it should not be neglected and proper consideration needs to be incorporated.

The error bars, in the representation of aerodynamic characteristics, have been set based on uncertainty in the measurement of respective parameter, obtained from the uncertainty analysis, performed for the experimental investigation.

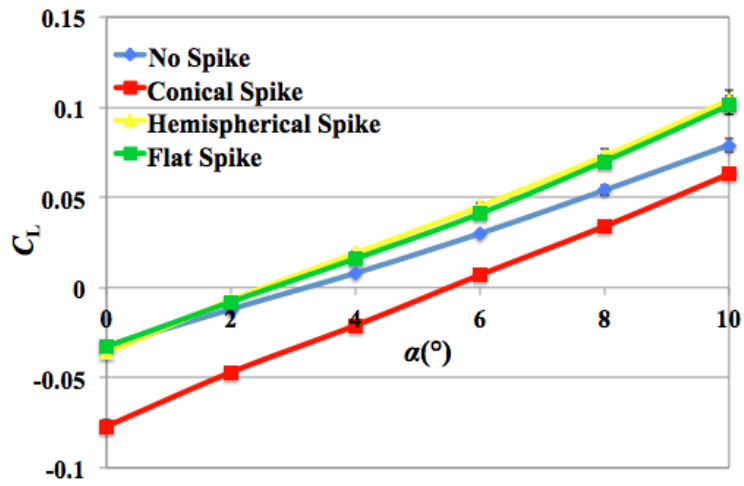


[Figure 4.17. Coefficient of lift comparison with angle of attack]

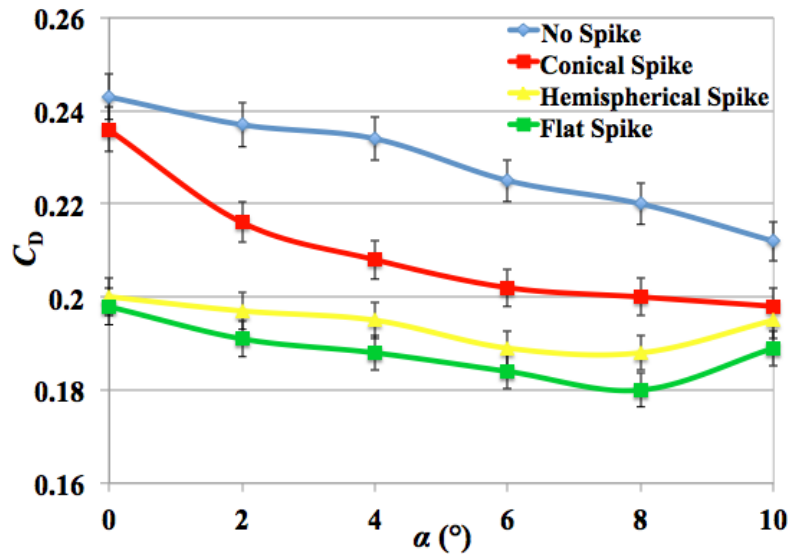


[Figure 4.18. Coefficient of drag comparison with angle of attack]

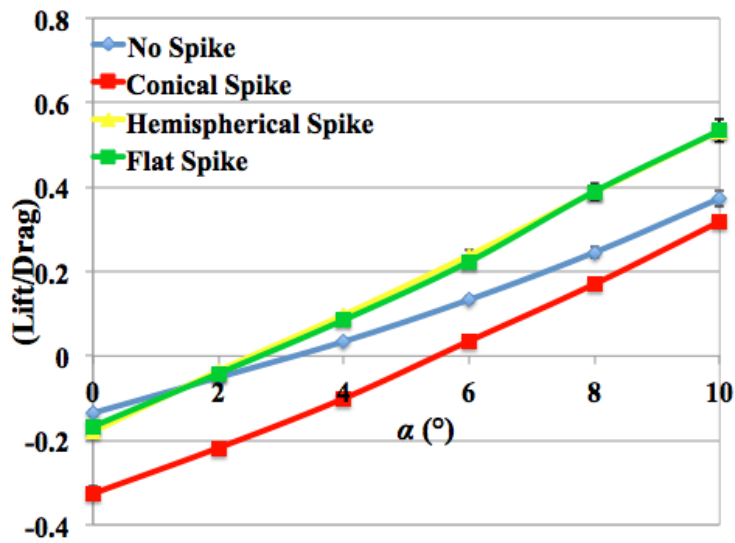


[Figure 4.19. Lift/Drag-ratio comparison with angle of attack]

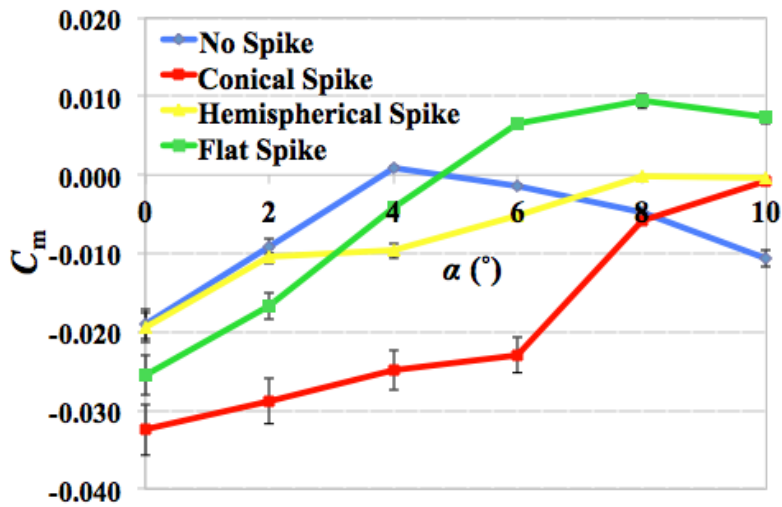


[Figure 4.20. Coefficient of pitching moment comparison with angle of attack]

#### 4.1.1.1.1.3 Heat Transfer Measurements

The thermal analysis was performed from the data captured and provided by the IR camera, installed inside the test section, during the conduct of the experiment. Table 4.1 summarizes the variation in the stagnation temperature ( $T_0$ ) for the different

experimental test cases. Figure 4.21 illustrates the time-history of the variation of surface temperature during the experiments. The model is inserted into the flow at  $t=18$  sec and retracted back at  $t=48$  sec, as is clearly visible from Fig. 4.21 depicting abrupt rise and fall in temperature respectively. For image processing, the option of the maximum value indication was selected in the IR camera application software for mapping the zone over the nose area.

Table 4.1.  $T_0$ -variation for different cases.

Experimental case	$T_0$
no spike	480-510 K
conical spike	580-600 K
hemispherical spike	600-620 K
flat spike	570-600 K

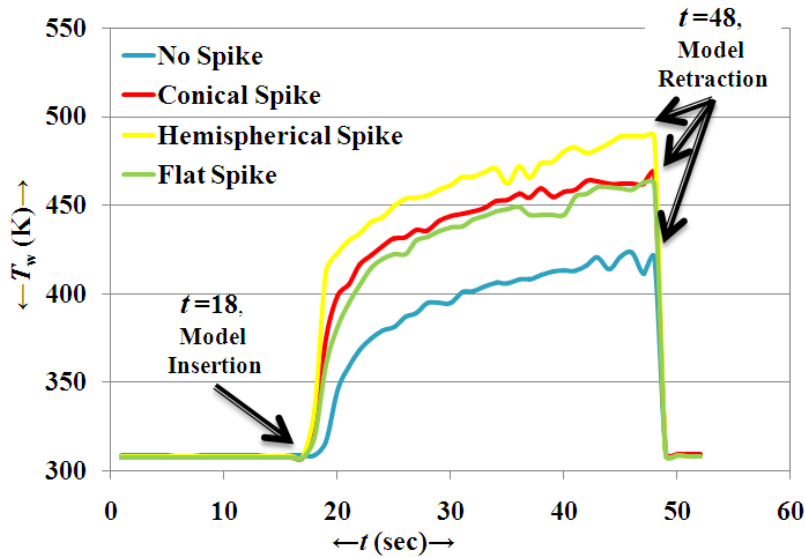


[Figure 4.21. Time-history of maximum surface temperature ( $T_{w,max}$ )]

Figure 4.22 shows  $T_w/T_0$ -variation and Figure 4.23 shows heat transfer to the geometry as a function of normalized parameter, i.e.  $C_h$ -variation at  $\alpha=0^\circ$ , calculated from instantaneous temperature profile, with non-dimensional  $x/R_c$ , where  $x$  runs on the nose curvature from the stagnation point ( $x=0$ ) towards the shoulder (as illustrated

on the graph). The heat transfer data reduction model employed the assumptions of one-dimensional heat conduction and time-invariant heat transfer distributions over the model surface applicable to Bakelite™ material, with good thermal insulation properties [27]. Its thermal product, as relevant to the data reduction model<sup>15)</sup>, is the square root of material's (specific gravity  $\times$  heat capacity  $\times$  thermal conductivity),  $\sqrt{\rho c K}$ , which, for Bakelite™, has a value of  $20.88 \text{ kJ m}^{-2} \text{ K}^{-1} \text{ s}^{-1/2}$ . The heat transfer rate [28] is then related to the surface temperature rise,  $\Delta T$ , measured over a time  $\Delta t$ , as Eq. (4.1) and presented in a non-dimensional heat transfer coefficient, denoted as  $C_h$ , defined in Eq. (4.2), where the symbols stand for standard abbreviation.

$$\dot{q}_s = \frac{(\sqrt{\pi \rho c K} \Delta T(t))}{2\sqrt{\Delta t}} \dots\dots\dots(4.1)$$

$$C_h = \frac{\dot{q}_s}{[\rho_\infty u_\infty C_p (T_0 - T_w)]} \dots\dots\dots(4.2)$$

Here,  $(T_0 - T_w)$  represents the difference between the total temperature of the flow and the initial model surface temperature. The instantaneous data from the IR camera is stored in the form of temperature mappings and temperature values of the entire field-of-view of the camera, throughout the experimental run, which are utilized for the evaluation of heat transfer rate over the model surface. Owing to low spatial resolution, the present results from IR camera used, holds true only for qualitative analysis. This graph signifies that a spike is beneficial in reducing the heat transfer near the stagnation point of the body. The  $T_w/T_0$ -variation and  $C_h$ -variation for spiked bodies follows a rounded curve profile on moving away from stagnation point, attains a maxima at about  $x/R_c=0.6$  and then decreases on moving further away towards the shoulder, for all the spike cases. For hemispherical spike, a detached shock wave standing in front of the spike-nose deflects the streamlines towards the nose shoulder, whereas for a flat spike streamline passing through the normal shock close to the spike nose traverse downstream. For a conical nose spike, the deflection is through a weak oblique shock that remains close to the body, and hence the elevated temperatures near the spike root are justified (as can be observed from Figure 4.8-4.9). On moving towards the shoulder of the body, this distribution shows that the local heat transfer is more than no-spike body indicating the reattachment of shear

layer. The reattachment occurs nearly at the same location for all the spikes, as confirmed by the increased heat transfer for the spike cases on the shoulder. Figure 4.10(a) shows the burnt part near the stagnation point, resulting from high heat transfer at possible reattachment location on the nose, which is corroborated by Fig. 4.10(b), showing illuminated bright spots as a sign of elevated temperatures. The wall temperature variation in time, at any given attitude of the model during the experiment, was examined to be negligible compared to respective stagnation temperature and hence the qualitative trend remains valid.

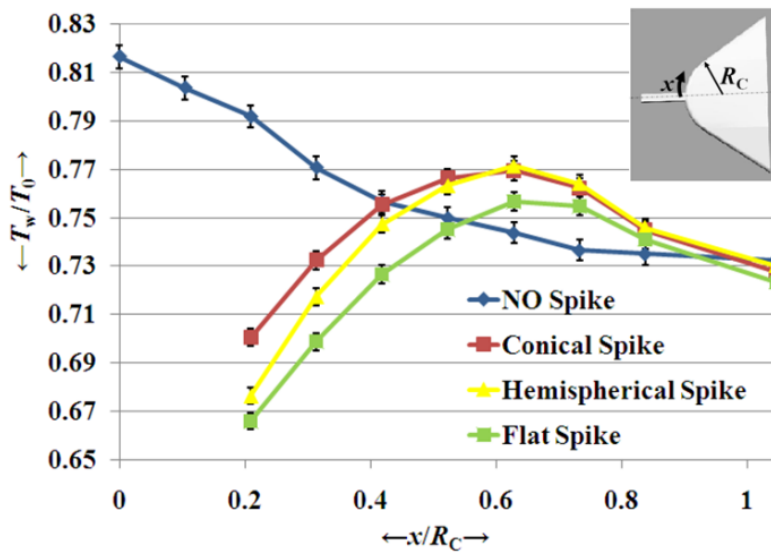


[Figure 4.22  $T_w/T_0$ -variation with non-dimensional length along nose curvature at  $\alpha=0^\circ$  and  $t=33$  sec.]

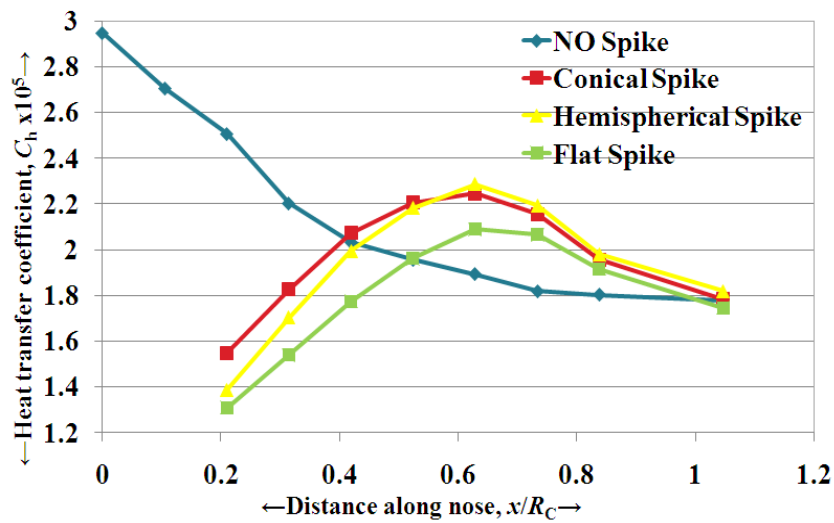
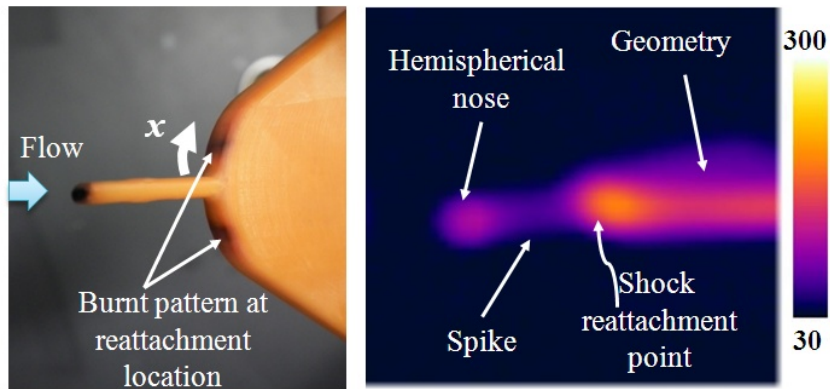


[Figure 4.23. Normalized heat flux comparison with non-dimensional length along nose curvature at  $\alpha=0^\circ$  and  $t=33$  sec.]



(a) Model after experiment (b) Instantaneous temperature profile ( $^\circ\text{C}$ )

[Figure 4.24. Model inspection after the experiment.]

#### 4.2.1.1.2 70°-Swept Leading Edge Configuration

The geometry considered in this investigation has its leading edges swept at an angle of  $70^\circ$  to the direction of wind, as described in Section 2.2.1.2.

##### 4.2.1.1.2.1 Force Measurements Results

The variation of Lift/Drag with angle of attack has been shown in Figure 4.25 consolidated for spike with  $(l_s/d_{eq})=3$ . It is interesting in the sense that the aerodynamic efficiency is strongly influenced by the spike characteristics (spike nose

and geometric length), with the maximum effect in terms of increasing the (lift/drag)-ratio for the hemispherical nose spike over the basic configuration.

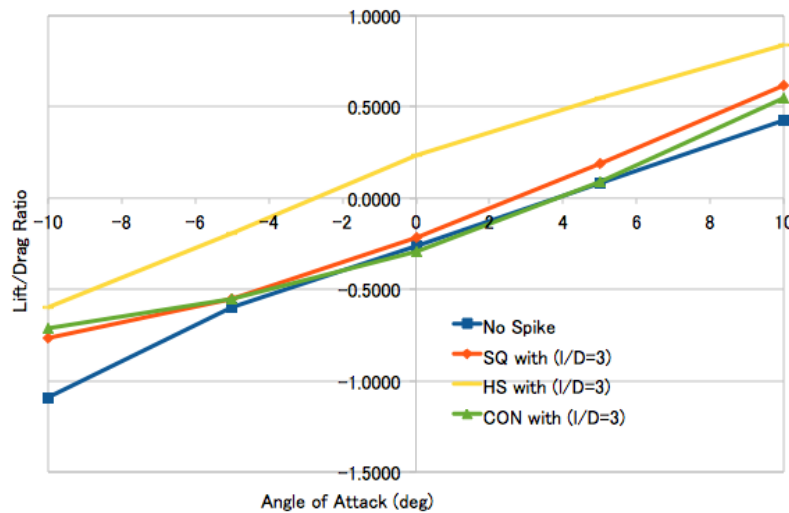


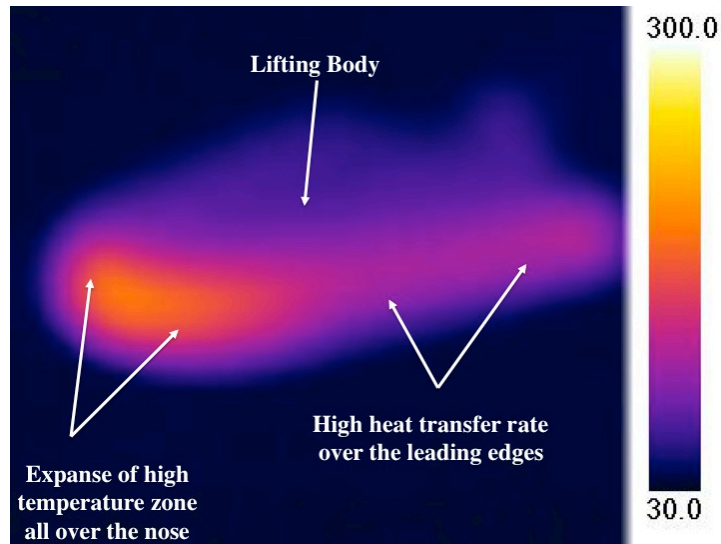
[Figure 4.25. Lift/Drag Ratio variation with angle of attack.]

The experiments demonstrated that, (1) the location and stand-off distance of the shock in front of the nose is changed from the main body towards the spike nose, as is clear from the schlieren images. (2) The model with aerospike resulted in increased lift coefficient and reduced drag coefficient compared to the model without spike, resulting in an increase in the aerodynamic efficiency (Lift/Drag), the highest being for a hemispherical nose spike. (3) An additional normal force component at the spike nose affects the overall longitudinal stability, invoking consideration for additional control surfaces at elevated angles of attack.

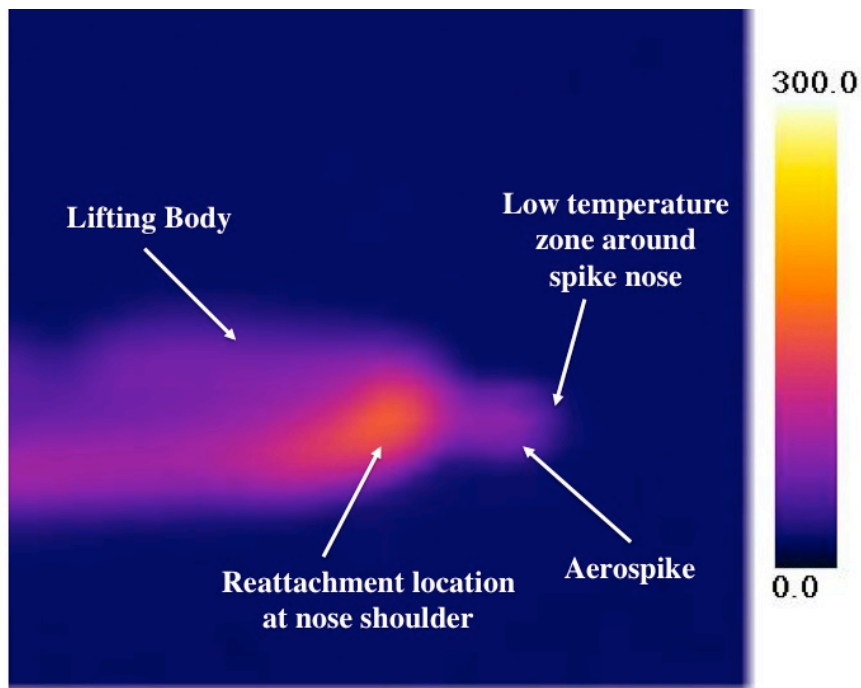
#### 4.1.1.1.2.2 Heat Transfer Measurement Results

Figure 4.26 illustrates large expanse of high heat transfer all around the nose area, for a no spike case body, followed by the leading edges. Figure 4.27 illustrates large expanse of high heat transfer around the nose area, for a spiked body case, followed by the leading edges, as a result of possible entropy layer reattachment. Measurements, from two-dimensional temperature distribution generated by an installed InfraRed camera, at freestream Mach number 7 revealed 1) significant reduction of locally heat-concentrated zones from body nose to small area of spike nose, 2) provides an understanding about the reattachment of entropy layer over the shoulder region of forebody whose location can be controlled by appropriately

selecting the type of aerospike (suitable nose-type and geometric parameters), 3) and; thereby indicating their worthiness towards practical feasibility for eventual future applications to high-speed vehicles from thermodynamic point of view.



[Figure 4.26. Instantaneous temperature profile over model without spike captured by InfraRed camera at  $\alpha=0^\circ$ . (temperature scale in  $^\circ\text{C}$ )]



[Figure 4.27. Instantaneous temperature profile over model with spike captured by InfraRed camera at  $\alpha=0^\circ$ . (temperature scale in  $^\circ\text{C}$ )]

## 4.2.1.2 Axisymmetric Nose Delta Configuration

### 4.2.1.2.1 Schlieren Visualization

The flow features around the models during the experiments were visualized using the Schlieren technique. Figure 4.28 and 4.29 shows the change in the flow field around the reference geometry (without spike) and that with a hemispherical nose spike at angle of incidence of  $0^\circ$  respectively. It can be clearly inferred from the figures that with the introduction of a forward-facing spike in front of the body nose, the change in location of main bow shock, in front of the body-nose is altered to weak foreshock generated from spike nose which reattaches itself at the body shoulder. The emphasis hereby lies to find an optimum spike-configuration (nose and length), to ensure weak foreshock to become just tangential to the body nose, without any reattachment points avoiding built up of pressure as well as localized heat concentration zones from shear layers. The full-length paper will encompass the detailed discussion from schlieren pictures for all the tested models.

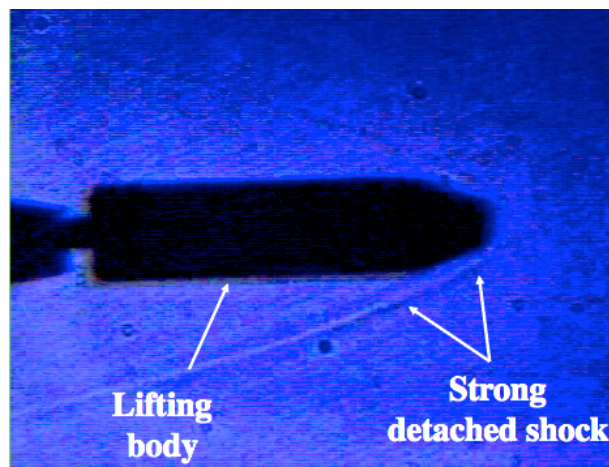


[Figure 4.28. Schlieren pictures for model without spike at  $\alpha = 0^\circ$ .]

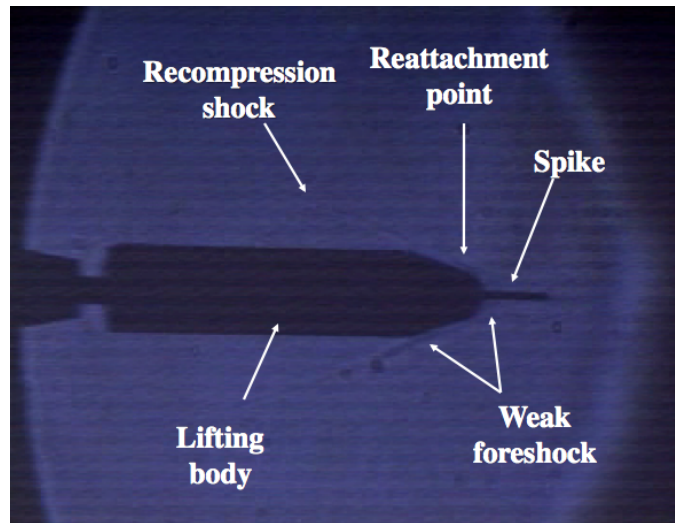


[Figure 4.29. Schlieren pictures for model with hemispherical nose spike with  $l/D=1.5$  at  $\alpha = 0^\circ$ .]

#### 4.2.1.2.2 Force Measurements Results

Some representative and consolidated results measured from the present study, investigating the flow field around a spiked lifting body have been presented in Figs. 4.30 and 4.31.

The variation of Lift/Drag with angle of attack is shown in Figure 4.30 with different spike cases consolidated for a comparison at  $l/D=1.5$ . It is interesting to see that the aerodynamic efficiency is strongly influenced by the spike nose configuration. The Lift/Drag-ratio increases almost linearly with  $\alpha$ , with  $(\text{Lift/Drag})_{\text{MAX}}$  condition being obtained for the case of hemispherical spike with  $l/D=1.5$ , over all range of  $\alpha$  as a consequence of the maximum reduction in effective pressure envelope around the geometric model for hemispherical spike resulting in higher  $C_L$  and reduced  $C_D$ .

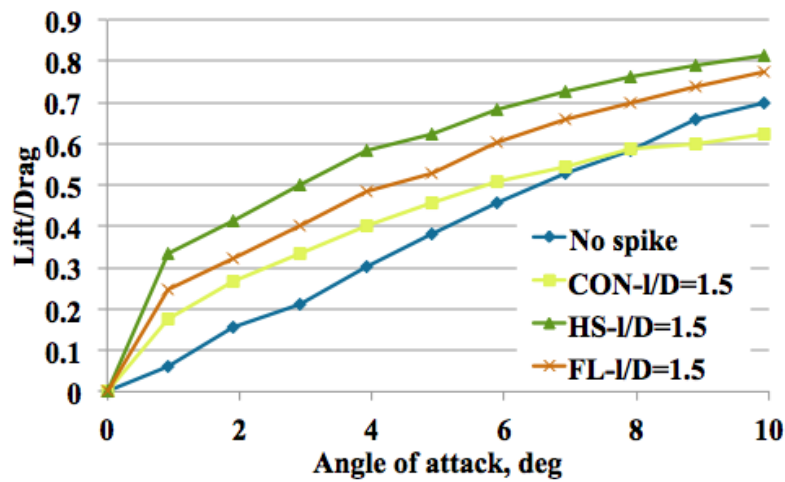


[Figure 4.30. Lift/Drag-ratio variation with angle of attack.]

The consolidated plot of pitching moment coefficient variation with angle of attack has been shown in Figure 4.31. It is observed that the stability of the basic body is significantly influenced by the presence of a spike at the nose of the body (from an additional normal force component at the spike nose), the most adversely for conically nosed one. The  $(dC_m/d\alpha)$  trend is measured to be positive and  $C_m$  increases with higher angles of attack.

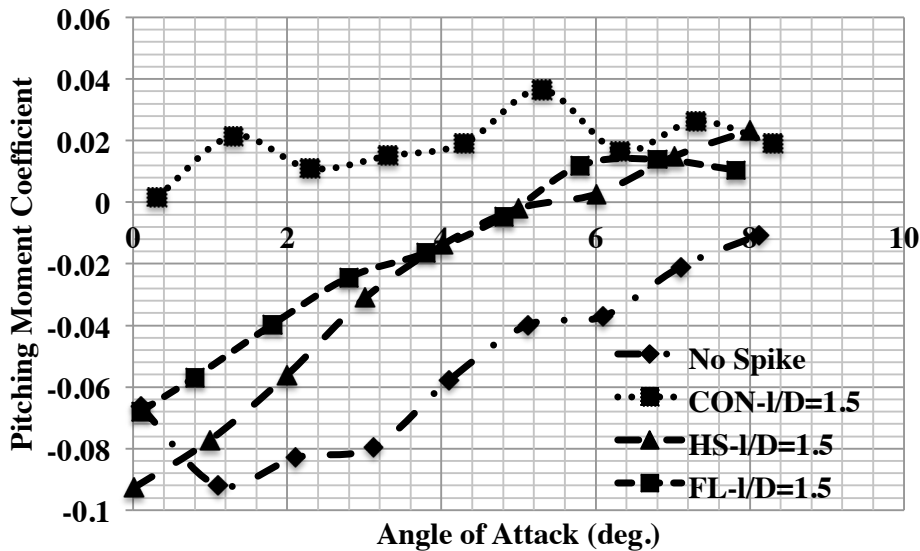


[Figure 4.31. Variation of pitching moment coefficient with angle of attack.]

The experiments using 0.004-scale simplified X-33 representative model, with and without spikes of different configurations, were conducted in the hypersonic wind tunnel for studying the change in flow-field and aerodynamic characteristics with its introduction on the nose and assessing their practical feasibility on lifting bodies.

The experiments and the consequent analysis of the results demonstrated that, (1) the location and stand-off distance of the shock in front of the nose is changed from the main body towards the spike nose, as is clear from the schlieren images, (2) the expanse of high-pressure envelope surrounding the lifting body nose and shoulder is restricted over a small area of spike nose, (3) the model with aerospike resulted in increased lift coefficient and reduced drag coefficient compared to the model without spike, resulting in an increase in the aerodynamic efficiency (Lift/Drag-ratio), the highest being for a hemispherical nose spike, and (4) An additional normal force component at the spike nose affects the overall longitudinal stability, invoking consideration for additional control surfaces at elevated angles of attack.

#### **4.1.1.2.3 Heat Transfer Measurement Results**

Some representative and consolidated results from the present study and analyzed by InfraRed camera have been presented in Figure 4.32-4.33. The temperature distribution around the lifting body without spike, have been shown in Figure 4.32, obtained from the InfraRed Camera. It can be clearly seen with blunt nose, the peak heat concentration at the nose is exhibited (due to the presence of strong bow shock as clear from Figure 4.28) with the elevated temperatures around the stagnation region.

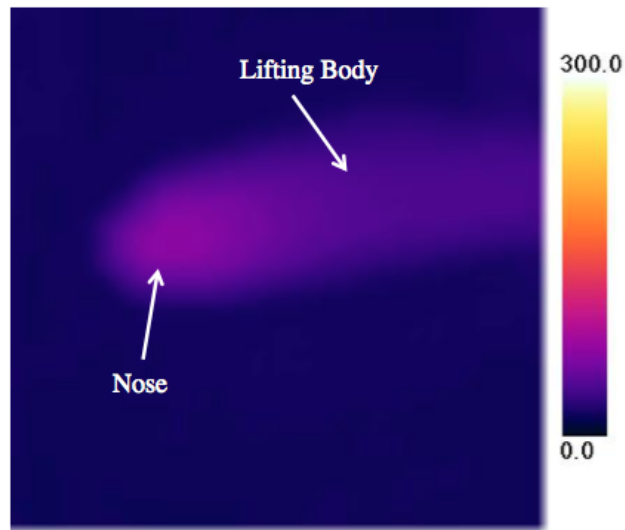


[Figure 4.32. Temperature distribution around body without spike at  $\alpha = 0^\circ$  (temperature in  $^\circ\text{C}$ ).]

The results in Figure 4.33 demonstrates that the change in the flow field together with the shifting of heat concentration zone from the body nose to body shoulder. The spike nose can be seen with elevated temperature owing to the weak foreshock presence from where the shear layer gets reattached at the body shoulder resulting in hot spots (highly heat concentrated zones), which indicated by the cell location and temperature data generated in matrix form from the InfraRed camera measurement. The heat transfer coefficient measurements with other cases (including flat spike and hemispherical spike) indicates the avoidance of shear layer reattachment owing to weak normal shock with remains tangential to the body shoulder, bringing the entire geometry under controlled heat envelope.

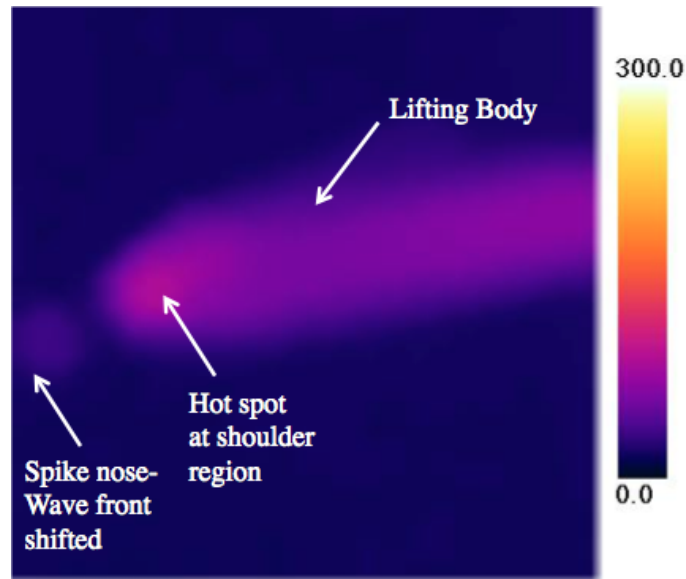


[Figure 4.33. Temperature distribution around body with conical nose spike ( $l/D=1.0$ ) at  $\alpha = 0^\circ$  (temperature in  $^\circ\text{C}$ ).]

The experiments using 0.004-scale simplified X-33 representative model, with and without spikes of different configurations, were conducted in the hypersonic wind tunnel for studying the change in flow-field and aerodynamic characteristics with its introduction on the nose and assessing their practical feasibility on lifting bodies.

The heat transfer results demonstrated that, (1) the location and stand-off distance of the shock in front of the nose is changed from the main body towards the spike nose, as is clear from the schlieren images, (2) the model with aerospike resulted in lowering the heat envelope around the main body and altering it with small area of spike nose resulting in decrease in heat transfer, the maximum reduction obtained for a hemispherical nosed spike case with  $l/D=1.5$ , and (3) the dependence of heat transfer characteristics on spike's geometric characteristics have been established, with the shock envelope standing much farther away from the body with the increase in spike length.

### 4.3 Breathing Blunt Nose Investigation

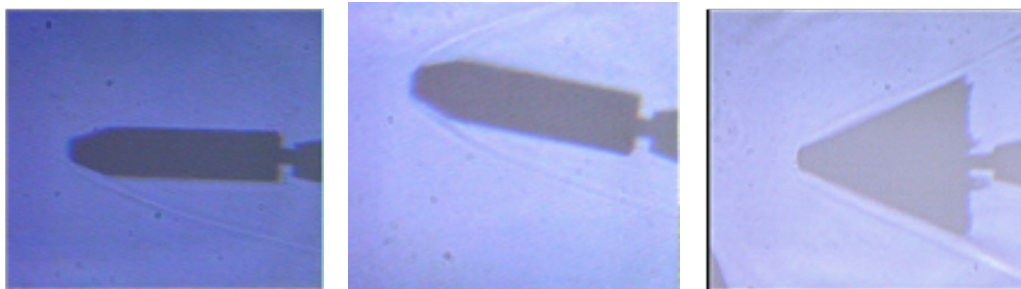
This section describes the results obtained from the investigation by employing breathing blunt nose technique.

#### 4.3.1 Axisymmetric Nose Delta Configuration

The geometry considered for the investigation using this technique has been considered to be a  $70^\circ$  swept back leading edge delta shape, with an axisymmetric nose, as described in Section 2.3 of Chapter 2.

#### 4.2.1 Schlieren Visualization

The flow features around the models during the experiments were visualized using the Schlieren technique. Figure 4.34-4.36 shows the shock around the model at angle of incidence of  $0^\circ$  and  $8^\circ$  from side view and at  $0^\circ$  from top view for all the configurations, with and without hole. It can be seen that with the increase in nose hole diameter, the shock wave comes closer to the nose with the increase of the bleed hole diameter, infact being bled more towards the nose and the shock wave shape becomes concave at the center for larger bleed hole diameter.



(a) Side view at  $\alpha = 0^\circ$       (b) Side view at  $\alpha = 8^\circ$       (c) Top view at  $\alpha = 0^\circ$

[Figure 4.34. Schlieren pictures for model without nose hole.]

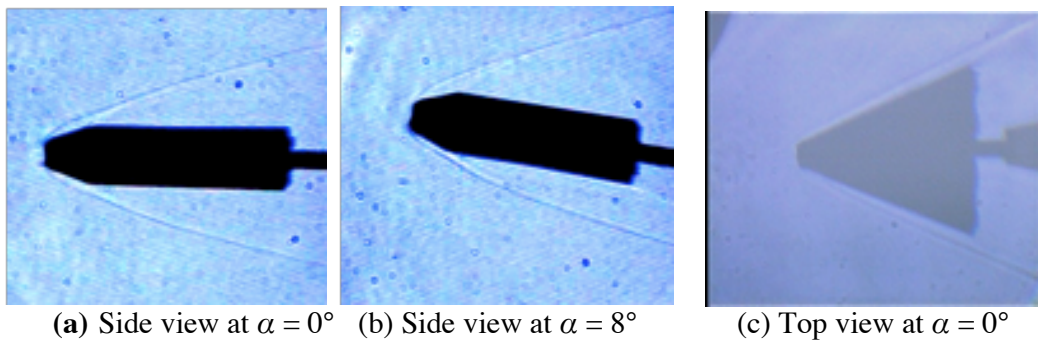


[Figure 4.35. Schlieren pictures for model with  $\phi 5$  mm nose hole.]

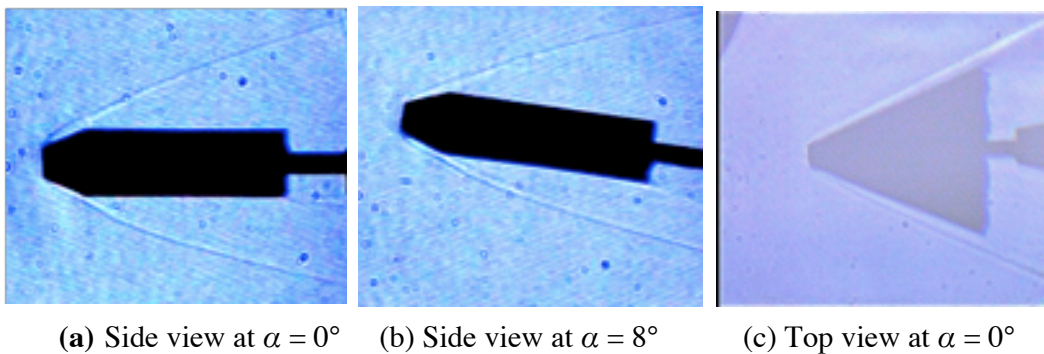


[Figure 4.36. Schlieren pictures for model with  $\phi 7$  mm nose hole.]

### 4.3.2 Force Measurements Results

The representative results, from aerodynamic investigation, of the present study have been depicted in Fig. 4.37-4.40. The variation of lift coefficient with angle of attack, shown in Figure 4.37, demonstrates that the size of the hole has a dictating effect on the lift coefficient. With the weakening of shock wave located nearer the stagnation area for geometry with hole, the entire flow field gets is altered. With increase in hole diameter, the shock zone over the leeward side of the model gets closer to the body surface, thereby resulting in the decrease of lift coefficient. With the increase in the angle of attack, for all the cases, increases monotonically with the angle of attack, compared to the case of the model without nose hole. The non-zero values at  $\alpha=0^\circ$  for no hole and 7 mm hole body are possibly attributed to a combination of surface burrs and change in alignment of model during the experiments, owing to high volumetric efficiency.

The breathing hole ( $\phi 5\text{mm}$ ) is capable of reducing the drag compared to basic configuration without hole. The reduction in drag continues even with the increase in  $\alpha$  for the present case and presents a maximum decrease at  $\alpha=8^\circ$ . However, the decrease of drag is strongly influenced by the hole size. It appears that decreasing the size of the hole could result in considerable decrease of drag, from the fact that the corresponding diameter of the channel and the leaving jet at the base encounters instantaneous expansion and hence higher the hole size, larger the wake area at the flow exit. This is clear from the trend depicted by breathing hole ( $\phi 7\text{mm}$ ) emphasizing on the Limit of Bleeding for drag reduction.

In order to clearly understand the flow physics inside the channel, a parallel investigation considering two-dimensional water channel flow visualization technique was performed, described in Case D of Appendix, which provided results and explanations through qualitative and comparative analysis, and corroborated the results obtained through hypersonic wind tunnel investigation.

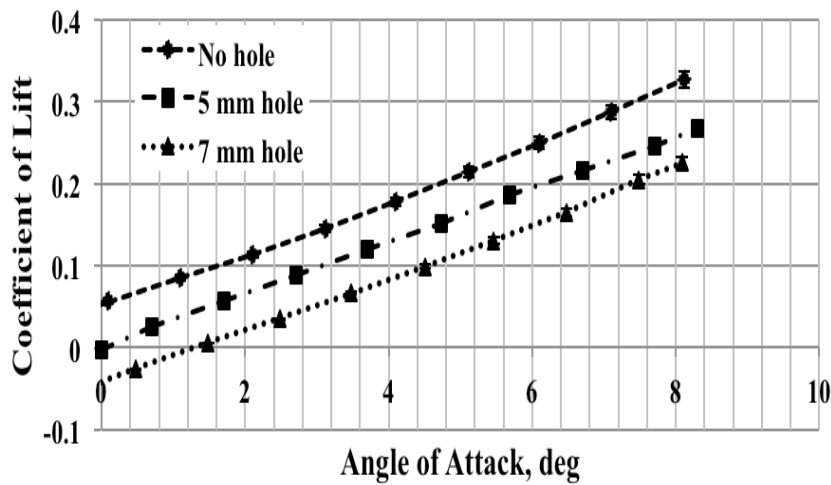


[Figure 4.37.  $C_L$ -variation with  $\alpha$ .]

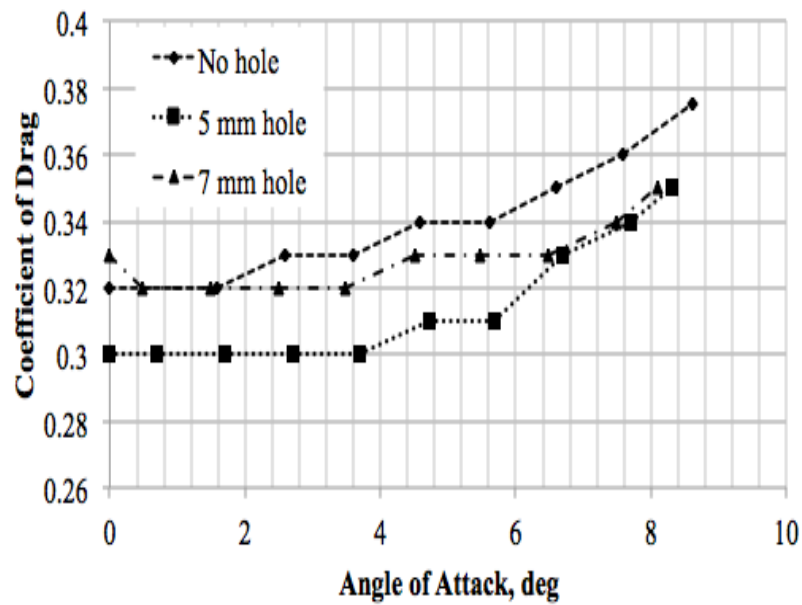


[Figure 4.38.  $C_D$ -variation with  $\alpha$ .]

The variation of (Lift/Drag)-ratio with angle of attack shown in Figure 4.39 is interesting in the sense that the aerodynamic efficiency is strongly a function of the hole size. Even though the drag reduction achieved with decrease of hole size is higher, the aerodynamic efficiency comes down considerably with hole size increase, for the present cases of 5 mm and 7 mm holes studied. The breathing blunt nose concept, therefore, find its application where drag reduction problem is of key interest.

The pitching moment coefficient variation with angle of attack, shown in Figure 4.40, is heartening that the stability of the basic body is not adversely influenced by the breathing hole at the nose of the body. The unstable basic representative configuration becomes more stable with the introduction of the hole at the nose and the discharge of the jets at the base. This can be regarded as a specific advantage compared to the spikes where the longitudinal stability is affected adversely.

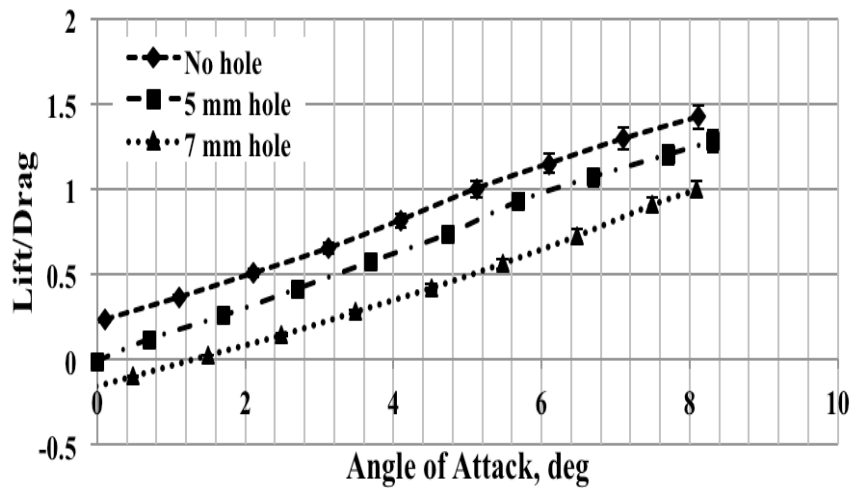


[Figure 4.39. (Lift/Drag)-Ratio variation with  $\alpha$ .]

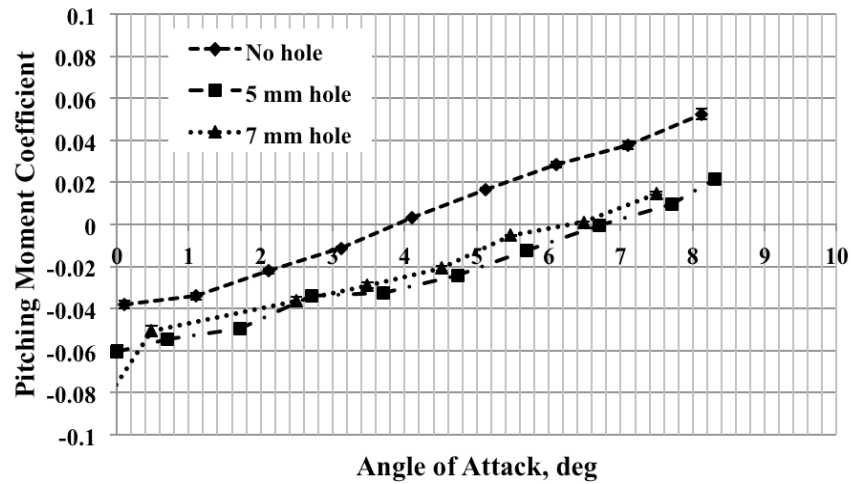
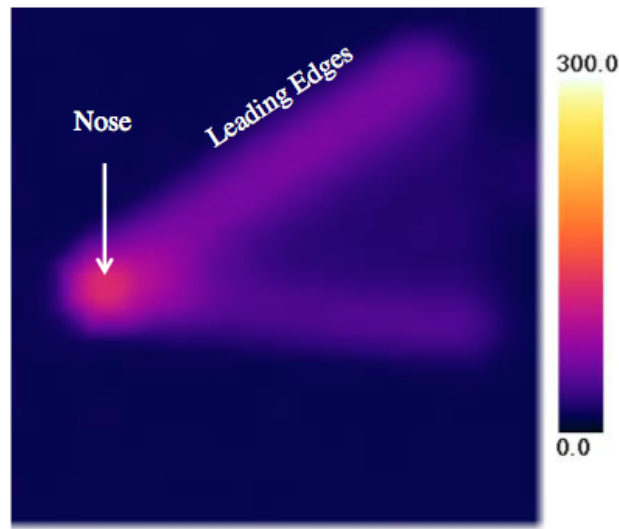


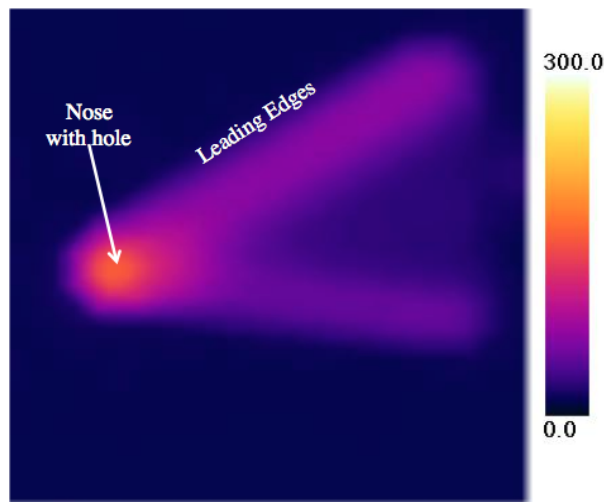
[Figure 4.40.  $C_m$ -variation with  $\alpha$ .]

### 4.3.2 Heat Transfer Measurements Results

Some representative and consolidated results, obtained from top side, from the present study and analyzed by InfraRed camera have been presented in Figure 4.41. The temperature distribution around the lifting body without hole, have been shown in Figure 4.41(a), and that with a 5mm hole shown in Figure 4.41 (b).



(a) Without nose hole



(b) With 5 mm hole

[Figure 4.41. Instantaneous temperature ( $^{\circ}\text{C}$ ) distribution around the lifting body configurations]

It can be seen that that the presence of a blunt nose on the basic reference geometry generates a bow shock in front of it, resulting in a uniformly distributed heat concentration zone (Figure 4.41(a)), whereas the presence of hole (consequently with sharp edges on the nose surface), as can be seen in Figure 2.16 and Figure 2.17, results in the locally heat concentration zones (as is clear from the explicitly bright areas around the nose seen in Figure 4.41(b)). This is a major concern in this technique wherein the design at the entry side of the channel (that is nose) and the

channel itself, carrying the high pressure and high temperature air from the nose towards the base, requires special attention.



## CHAPTER 5

# CONCLUSIONS

### 5.1 Aerospike Technique

Six-component force and temperature measurement study have been successfully carried out at Mach 7 hypersonic wind tunnel on spiked, lifting-body configurations in order to study the effects of spike on drag reduction phenomena and passive thermal protection. The major conclusions deduced from the current investigation are as follows: -

- a) A spike attached to the forward stagnation surface (nose) of the vehicle geometry is capable of changing the flowfield structure in its vicinity by creating a low pressure recirculation bubble around the stagnation point and hence can be used as a 'passive-control device' for possible flowfield modification.
- b) The experimental results demonstrated a flat-faced (square) spike and a hemispherical spike appears to be effective options among studied models for consideration for a non-axisymmetric nose lifting body configuration, but needs to be validated through numerical analysis.
- c) The experimental results demonstrated a hemispherical spike appears to be the best option studied for consideration for an axisymmetric-nose lifting body configuration for its capability to appropriately keep the weak foreshock, emanating from its nose, sufficiently tangential to the body shoulder.
- d) The use of spike is justified for high angles of attack also, as there is a significant increase in Lift/Drag-ratio with increasing  $\alpha$  but only a marginal increase in drag and pitching moment has been observed.
- e) A spike has been proved to be capable of reducing the local heat transfer near the stagnation point, but an optimum spike configuration (in terms of nose and  $l_s/d_{eq}$ ) is required to be researched on, in order to avoid the reattachment of shock wave on the nose (unlike the present case), in order to alienate any high-heat

concentration points. For making the best use of a spike, extensive study needs to be performed to find an optimum solution with respect to spike length and spike-nose configuration, and its use will be dictated by the application and mission requirements.

- f) The emphasis is to ensure that the suction created by the vortex is just enough to make the shock become tangential to the shoulder of the body for optimum reduction of the pressure field over the body-nose, thereby resulting in significant reduction of pressure drag. This will also ensure the alleviation of any locally high heat concentrated zones due to possible reattachment of the shear layer onto the shoulder.
- g) The data from the experimental investigation of aerothermodynamic parameters for flow around an aero-spiked body has been examined in terms of accuracy. The present force and heat test results are expected to provide useful information as a database for the validation of outcomes from CFD codes, which will reveal the effects of the spike on the flow field around the lifting body that cannot be clarified by the experiments.

## 5.2 Breathing Blunt Nose Technique

The experimental investigation, conducted in the hypersonic wind tunnel, employing breathing blunt nose technique was performed on axisymmetric-nose lifting body with  $70^\circ$  sweepback angle, (simplified X-33 representative model), with and without nose holes, for studying the effect of air bleeding, through the nose, on aerodynamic characteristics.

The experiments demonstrated that,

- (1) The shock distance in the front of the nose decreases with the increase in hole diameter, as is clear from the schlieren images.
- (2) The model with bleeding holes resulted in reduced drag coefficient compared to the model without nose hole. The reduction in the drag is attributed to the combined effect of reduced shock strength and increase in the base pressure with the discharge of high-pressure air through the nose hole.
- (3) The visualization results, depicting the flow field, from the water channel are identical to the ones around the main body geometry as captured from the Schlieren pictures, in spite of the limitation of the former for incompressible flows.

(4) The results from water channel visualization, on a qualitative and comparative measure, corroborates to the finding from the wind tunnel investigation, highlighting the existence of a limit on bleeding from the nose.

(5) The heat transfer study performed on models with and without holes, provided an insight towards locally heat concentrated zones on the sharp edges of the holes, and towards the complexity in the design of the channel.

(5) The application of breathing blunt nose concept does hold true validity for practical applications, where drag reduction is the prime objective rather than increase in (Lift/Drag)-ratio (aerodynamic efficiency).

### **5.3 Consolidated Results**

The experimental investigation from current research on passive flow control techniques (of an aerospike and a breathing blunt nose), by extending their studies to lifting body configurations, has provided a deep understanding about their practical feasibility and effectiveness in order to curb the effects of high temperature air and pressure, safeguarding the inner load carrying structure and contributing towards improving the overall economic efficiency.

Though both the techniques looks promising in enhancing the aerodynamic performance of the vehicle, they are accompanied with stability issues and the complex design of inner channels respectively, which must be subjected to further study in order to arrive at a final conclusion about their applicability as a flow control mechanism on futuristic high-speed vehicles. The research conducted in here, investigating several cases by varying the geometric parameters is valid within the parameters and pre-decided testing conditions considered here. A general conclusion about the applicability of the passive flow control techniques hasn't been attained.

Table 5.1 illustrated the consolidated results and conclusions summary from the extensive experimental investigation, with respect to key factors of investigation. The results have been specifically marked into three different colors in order to highlight its importance, red depicting a negative result on use, green depicting a positive and advantageous result on use and orange depicting the application.

[Table 5.1: Conclusions in a consolidated manner]

S.No.	Properties	Aerospike Method	Breathing Blunt Nose Method
1	Coefficient of Lift	<b>Increases</b>	<b>Decreases</b>
2	Coefficient of Drag	<b>Decreases</b>	<b>Decreases</b>
3	Aerodynamic Efficiency	<b>Increases</b>	<b>-- (Mainly for drag reduction)</b>
4	Longitudinal Stability	<b>Affected significantly</b>	<b>Not affected significantly</b>
5	Localized Heating Spots	<b>Yes (To be avoided by proper selection of spikes)</b>	<b>Near Stagnation Region</b>
6	Disadvantages	<b>Extra Normal Force Component – Longitudinal Instability</b>	<b>Channel Design inside the main body – Design complexity</b>

## **APPENDIX A**

### **WATER CHANNEL EXPERIMENTS**

This section consists of, and highlights on the various experiments performed on simple cylindrical bodies, with and without spike, in varying test conditions and flow regimes, that deepened the understanding of flow behavior and generation of specific flow field around spiked bodies with the vortices (deemed as the sole reason for pressure reduction), and extended the same towards lifting body configurations.

Two-dimensional Rectangular Water flow Channel serves as an extremely Low-cost device with quick Response for flow field visualization. It has been used as an auxiliary device for providing an insight into flow physics around various employing Hydraulic Analogy, and as a supportive technique. The only limitation with this method is that it being meant only for Inviscid and two-Dimensional flow simulation. This implies that the results obtained through this technique find their application only in qualitative understanding.

#### **A.1 Theory**

The various analogies involved in correlating a two dimensional gas flow with that of a two-dimensional water flow are summarized in the Table A.1. Hydraulic analogy has been devised for analogously simulating two flow field conditions, of a two-dimensional gas flow into a two-dimensional shallow water flow, with the free surface of water generating the flowfield around a typical geometric configuration. This technique has been deemed of high importance owing to its capability of simulating flow features in an inexpensive manner, pertaining to complex and practical problems in high-speed flows involving shocks, expansion waves, unsteadiness, internal flows etc. requiring sophisticated and expensive wind tunnels, instrumentation and techniques. A thorough literature review proclaimed that the explanation behind the analogy have been dealt and explained in theory but its significance and validity haven't been investigated indepth through experiments,

thereby citing and highlighting the analogous flow features and additional observations, if any. Additionally the discussions and conclusions about the fair amount of inaccuracies and limitations incorporated, by simulating a three-dimensional viscous flowfield using a two-dimensional incompressible inviscid medium, needs to be carefully assessed. Hence, in the current research, experiments employing the analogy were performed, in a two-dimensional water channel, to understand the physics and the working principle behind the analogous simulated flowfield of a Mach 7 flow (at an equivalent Froude number of 7) around breathing blunt nose geometries (discussed in Chapter 4) and around spiked cylindrical bodies (discussed in this chapter, Case 3), in a shallow rectangular two-dimensional water channel, manufactured in-house in the laboratory, using the free surface of water for flow visualization, and fabric-color dyes as visualizing elements. The study revealed analogous flow features of hydraulic jumps (characterized similar to shock waves in supersonic flow), together with weak expansion waves, vortices-identification and visualization, which was otherwise not possible in case of high-speed wind tunnel experiments. The effect of ignoring surface tension and vertical accelerations, by neglecting water depth for two-dimensionality, adds further error in quantitative comparison by shifting the position of hydraulic jumps further away from the geometries especially in low-speed simulations. Simulating high-speed flows results in accumulation of water in front of the geometrics, leading to increase in water depth in the immediate vicinity. Consequent hydraulic jumps results in a fringe-pattern of disturbances, generated as a result of assuming the disturbance, at a high-water depth ahead of it, as an auxiliary body, and consequently dies out where the water-depth difference in the stream becomes negligibly smaller. Hence the applicability, of hydraulic analogy to qualitative as well quantitative visualization, will be discussed.

[Table A.1 Hydraulic analogy.]

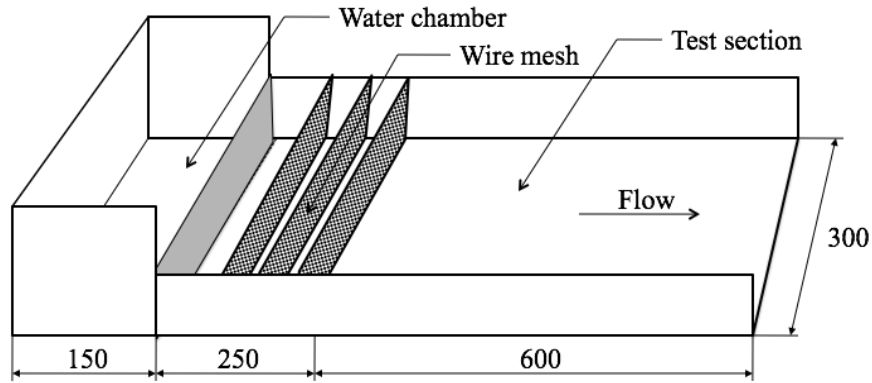
Item	Two-Dimensional Gas Flow	Liquid Flow with Free Surface in Gravity Field
Nature of the flow medium	Hypothetical gas with $\gamma=2$	Incompressible fluid (e.g. water)
Side boundaries geometrically similar	No specific boundary	Side boundary vertical, bottom horizontal
Analogous magnitudes	Velocity, $V/V_\infty$	Velocity, $V/V_\infty$
	Pressure, $p/p_\infty$	Square of the water depth ratio, $(h/h_0)^2$
	Temperature, $T/T_0$	Water depth ratio, $h/h_0$
	Density ratio, $\rho/\rho_0$	Water depth ratio, $h/h_0$
	Speed of sound, $a$	Velocity, $(gh)^{1/2}$
	Mach Number, $V/a$	Froude Number, $V/(gh)^{1/2}$
	Subsonic flow	Streaming water
	Supersonic flow	Shooting water
	Compressive shock	Hydraulic jump

## A.2 Methodology

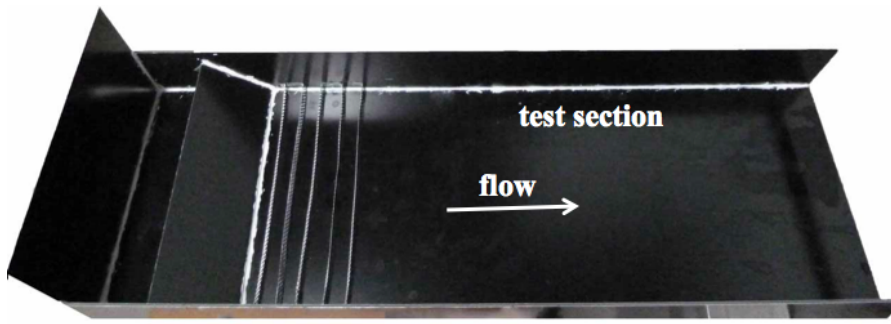
In the current investigation, the flow around the geometries was visualized using a rectangular water flow channel in the Suzuki K. Laboratory, The University of Tokyo. This two-dimensional visualization technique has been performed with the aim of obtaining an insight of the flow physics around the lifting body, its nose area with and without holes, the flow inside the channels and the discharge at the wake region. This employs hydraulic analogy to simulate and thereby producing the condition to compare a typical gas flow around an object with that of an incompressible flow (water, in this case), around a representative model of the geometry. For the present experiments and comparison with hypersonic wind tunnel results obtained at Mach 7, the flow velocity and conditions were set equivalent to that of Froude number (given by  $v/(gh)^{1/2}$ ) equal to 7, which presents the condition for possible comparison as per Hydraulic Analogy. The flow behind the shock wave, bled from the nose passing through its channels and getting discharged at the base, is assumed to be inviscid, thereby providing sufficiently valid results for comparison.

### A.2.1 Test Conditions

Schematic diagram and a pictorial view of the channel are shown in Figs. A.1(a) and A.1(b), respectively.



(a)



(b)

[Figure A.1 (a) Schematic diagram of the experimental set-up (dimensions in mm), (b) pictorial view of the set-up.]

Water from the chamber, spills over the inclined plate and is conditioned using an array of wire-meshes, before reaching the downstream of the test-section. The flow quality is ensured to be fairly uniform in the test-section. The velocity of the flow is measured using the floating-particle method technique. Time taken to traverse over the length of the test-section by the particle (a small bit of paper) gives an indication of the flow velocity. The average of a set of 5 samples of measured velocities is taken as the representative velocity of the flow. The axis of the models were aligned parallel to the flow direction at the middle of test-section for every test. The flow field in the test-section was ensured to be parallel and uniform by observing parallel streak lines

of dye injected upstream of the empty test-section. Then the model was placed in the test-section. For the water-channel experiments, the velocity of the uniform flow in the water channel, before the conduct of the experiments, was measured by floating-particle method, by placing a small bit of paper on the surface of the flow and noting the time taken to traverse the length of the test-section. A set of 5 readings were taken, and the cumulative average of the same is taken as the representative value of velocity for the particular test case to evaluate the flow Froude number, for this research to be conducted at flow equivalent to Mach 7.

### **A.2.2 Instrumentation**

The following devices and instruments have been employed during the conduct of the experiments.

#### **✦ Video & Still Camera**

- ✦ To capture the video and taking still pictures respectively during the experiments, shown in Figure A.2

#### **✦ Ruler and Stop Watch**

- ✦ For estimating the distance traversed and time taken for velocity measurement by Particle-flow method
- ✦ Average of a set of 5 readings was taken as the representative velocity of the flow

#### **✦ Fabric Dye Colors**

- ✦ Contrast fabric dye colors to be used as visualizing elements, to trace out the streamlines in flow, thereby depicting the flowfield around various configurations



[Figure A.2. Still camera for capturing pictures]

### A.2.3 Data Acquisition and Processing

The flow field was recorded on a video camera (PANASONIC, Model DMC-ZX3) with resolution of 1280 x 720 and at 30 frames per second. The captured images from the videos serves as a source of visualization at different time intervals. The pixel length and density, for a particular flow phenomena measured from the still picture, when non-dimensionalized, serves as a source of visualization.

#### A.2.3.1 Data Uncertainty

The error in the measurement of the velocity was estimated to be within  $\pm 4$  percent. The accuracy in the evaluation of characteristic lengths of the vortex zones from the captured videos near the nose and at the base, at a conservative estimate of  $\pm 2$  pixels, stood at  $\pm 5$  percent.

In this regard, various experimental cases pertaining to the different flow conditions around geometric configurations (spiked and having breathing hole at the nose respectively) were performed, to obtain only a comparative and qualitative understanding of flow behavior, which would be difficult to be obtained from wind tunnel experiments at hypersonic speeds.

**Case A: - Flow field variance with change in Reynolds Number**

An experimental visualization study was performed to investigate the dependence of the pressure hill height and the influence zone expanse for flow past a spiked body with different nose configurations, over a Reynolds number range from 2278 to 4405. It is found that, the spike reduces the radius of curvature of the approaching streamline, and the deflection of the streamline is towards the shoulder of the basic body, resulting in a narrow zone of the positive pressure hill at the body nose. It is also observed that, the pressure hill length and the influence zone expanse decreases with the introduction of spike over the range of Reynolds Numbers. For  $Re < 2700$ , conical nosed spike is found to be efficient in reducing the pressure. For higher Reynolds numbers ( $Re > 2700$ ), it is found that, the size of the vortex at the junction of the spike and basic body is the largest for the spike with hemispherical nose, and emerges as a potential candidate for application.

There is an urgent need to understand the process associated with the flow over the basic body, with and without spike, for optimizing the spike geometry, resulting in an efficient drag reduction. To gain an insight into the essential features of the flow physics associated with the drag reduction, it is essential to measure these parameters (illustrated in Figure A.3), if possible, directly. As a first step in this direction, flow past the desired blunt-nosed body, with and without spikes, was visualized in a simple two-dimensional water channel, at a specific Reynolds number of 3070 by Khurana et al. (2012) [29]. The objective here was essentially to gain an insight into the important features governing the flow physics, without going into the application aspects governing the hypersonic flows, successfully capturing and visualizing the changes in flow field with the introduction of a spike, by flow parameter quantification. In continuation to the previous work, efforts were focused to understand the functional dependence, and consequently the variation of these parameters on Reynolds number, which is expected to enhance the understanding of vortices shed by the spike at the root and the body in the wake. An experimental investigation was carried out with water flow past the hemispherical fore-body, with and without spikes, and the parameters were measured in the range of 2278 to 4405. Also, this *Re*-range will certainly provide key details in assessing the applicability of

an aerospike in low-speed regime involving flow around stationary structures and its wind resistant design, unlike the research focused on its use in supersonic and high-speed flows until now.

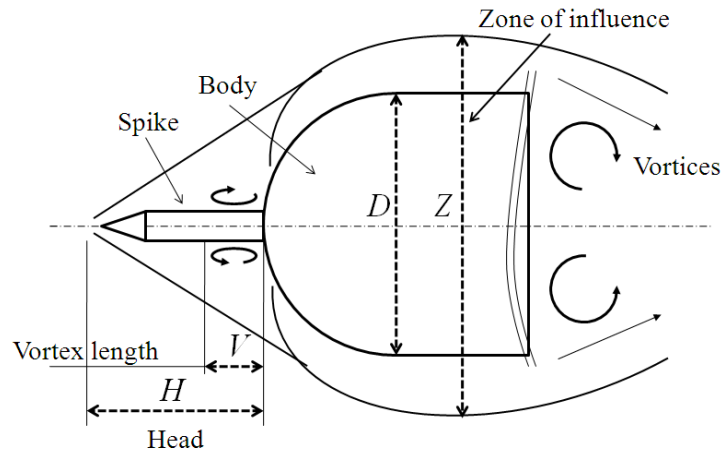


[Figure A.3. Flow field nomenclature]

The axis of the model was aligned parallel to the flow direction, placed at the middle of test-section for every test. The model consists of a hemisphere-cylindrical fore-body, as shown in Figure A.4, with cylindrical spikes having hemispherical, conical and flat nose configurations, having a spike root diameter  $d$ , and a specific case of spike of square cross-section with side or equivalent diameter equal to  $[(\pi/4)^{0.5}d]$ . The tests of the present study were carried out over a Reynolds number range from 2278 to 4475 (summarized in Table A.2), based on the main body diameter. After ensuring proper alignment of the model, some time was given for the flow to develop properly. The model was then placed in the test-section and the flow field during each experiment was recorded on a video camera (PANASONIC, Model DMC-ZX3) with resolution of 1280 x 720, and at 30 frames per second. The videos recorded clearly exhibit the zone of influence ( $Z$ ), head ( $H$ ) and the vortices ( $V$ ) at the base. Watercolor fabric dye was used as the visualizing element in the experiments.

[Table A.2. Reynolds Number for the test cases.]

Case Number	Flow Velocity, $\nu$	Reynolds Number (based on body diameter), $Re_D$
1	0.0572 m/s	2277.6
2	0.0673 m/s	2683.8
3	0.0797 m/s	3176.1
4	0.0931 m/s	3708.7
5	0.1105 m/s	4405.34

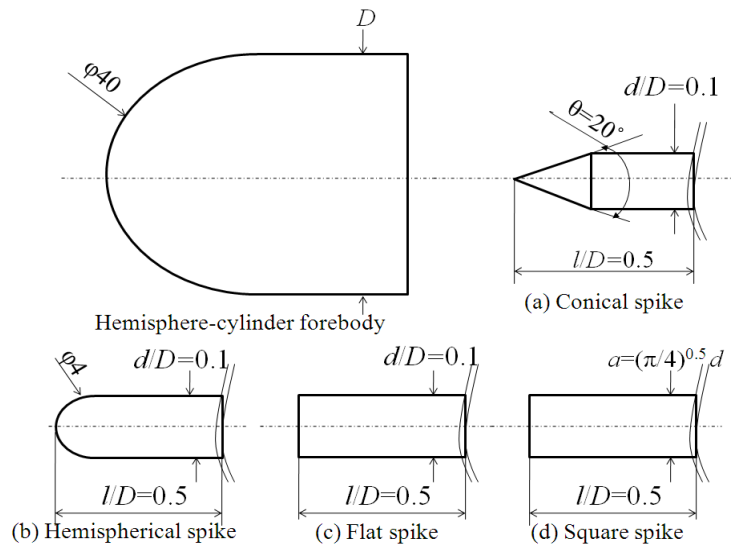


[Figure A.4. Test geometry with spike configurations.]

## Results and Discussion

It has been well established (Ahmed et al. 2011 [7]) that the positive pressure at the nose and the negative pressure at the base, together, cause the large drag associated with blunt nosed bodies meant for high-speed applications. Therefore, it is essential to reduce the positive pressure at the nose and the negative pressure at the base to bring down the drag over the blunt nosed body. In the present investigation, with the sole aim of addressing these two parameters, namely the pressure hill (positive pressure zone at the nose) and the zone of influence of the flow field around blunt-nosed body of geometry, with and without spikes, were studied directly, using the flow visualization techniques.

Some representative visualization pictures of the flow over the body without spike, and with conical, hemispherical and flat-nosed cylindrical spikes and a flat-nosed square spike, captured in this study at  $Re = 2278$ , are shown in Figure A.5. These pictures of the flow field clearly exhibit the zone of influence  $Z$ , the head  $H$  and the vortex length  $V$ . These parameters were measured by projecting the visualization pictures on screen, for all the models studied, from the videos recorded. For every case, the average of a set of measurements has been taken as the representative values of the parameters  $H$ ,  $Z$  and  $V$ . The vortex length  $V$ , owing to its small size and small area of confinement in comparison to  $H$  and  $Z$ , has been separately visualized, quantified and studied using different dyes, by injecting the same at the spike-root location, for all the cases, rather than injecting upstream of the model in the water channel. Figure A.6 shows the visualization pictures of the flow over the body, with hemispherical spike, in the Reynolds number range from 2278 to 4405. The point to note here is that the white arced lines appearing in the region of the body nose in the images of Figures A.5 and A.6 are in fact the reflection of the model on the surface of water flow as a result of light source.

The pressure hill head  $H$ , non-dimensionalized with the diameter of the blunt nosed body, is plotted for the basic body and the body with spikes, in Figure A.7, as  $H/D$ -variation. Variation of  $H/D$  with Reynolds number is plotted in Figure A.8. The plotting of  $H/D$ ,  $Z/D$  and  $V/D$  has been done separately with respect to spike-nose and  $Re$  to independently investigate their dependence on these parameters. It is seen that, at low Reynolds numbers, the body without spike experiences the smallest pressure hill height, followed by the conical spike. With increase in  $Re$ ,  $H/D$  drastically shoots up for both no-spike body and body with conical spike. This increase continues monotonically for the basic body without spike, and drops to the minimum value for the spike with conical nose, before attaining maxima amongst all the cases. Reynolds number 2700 can be considered as a transition of the flow phenomena for the conical spike, below which it can be considered effective in reducing the pressure height. The spike with hemispherical nose has a larger  $H/D$ , which remains constant over the entire experiment range of  $Re$ . Furthermore; the pressure hill heights for the flat-nosed spike with cylindrical and square stem are comparable. It has to be realized that the pressure hill height acts on the nose of the body for the case without spike, and on the spike nose for the body with spike. It is worthy to note that, although  $H/D$  for the spike cases is larger than the no-spiked body, the actual high pressure concentration

zone is limited only to the spike-head thereby leading to significant reduction of the pressure over the nose area, unlike the former where it exists as high-compression zone uniformly distributed over the entire nose area. One key aspect observed is that the effect of Reynolds number on the pressure hill is sensitive to the spike nose configuration in front of the body. Thus the combination of the geometrical and flow parameters strongly governs the flow field around the blunt body.

Another important parameter is the zone of influence; the extent of this zone can be regarded as a direct indication of the drag caused by the positive pressure field at the face of the body. To gain an insight into this important parameter's dependence on spike geometry, at a specified Reynolds number, the zone of influence  $Z$ , as non-dimensionalized  $Z/D$ -variation, for the blunt nosed body, with and without spike, is shown in Figure A.9, and as a function of  $Re$  in Figure A.10. At low  $Re$ , the zone of influence  $Z/D$  is nearly the same for all the cases, but with the increase in  $Re$ , the spike with hemispherical nose reduces the zone of influence drastically from 1.67 to less than 1.47. This may be envisaged as a direct indication of reduced positive pressure over the nose of the basic body. It can be interpreted that, the radius of curvature of the approaching streamline is reduced; the deflection of the streamline is towards the shoulder of the basic body, resulting in a narrow zone of the positive pressure-hill at the nose. Therefore, integral of this positive pressure over the nose of the body with spike of hemi-spherical nose assumes lesser magnitude, compared to the positive zones for the spikes with conical or flat face, resulting in relatively smaller drag. With further increase of  $Re$ , although  $Z/D$  continues its increase for conical and flat-nosed spike, the hemispherical spike is successful in diminishing the pressure distribution over the body. To authenticate this inference, the non-dimensionalized size of the vortex ( $V/D$ ) prevailing at the attached end of the spike, schematically illustrated in Figure A.11, has been quantified and compared for the different spikes at various  $Re$  of the present study, in Figure A.12. It is eminent that, larger the size of the vortex higher the suction caused by it. In accordance with this, the spike positioning a larger vortex is capable of reducing the positive pressure to a greater extent, compared to the spikes, which create smaller vortices. It is interesting to see that, the vortex size for the hemispherical nose, over the entire  $Re$ -range, is the largest. The cylindrical spikes with flat and square nose are also capable of positioning vortices of significant magnitude at the spike root. This clearly supports

the inference of the reduced expansion zone visualized. Therefore, it may be presumed that the hemispherical nosed spike is the best candidate for reducing the drag of the blunt-nosed body, compared to the conical and flat nosed spikes.

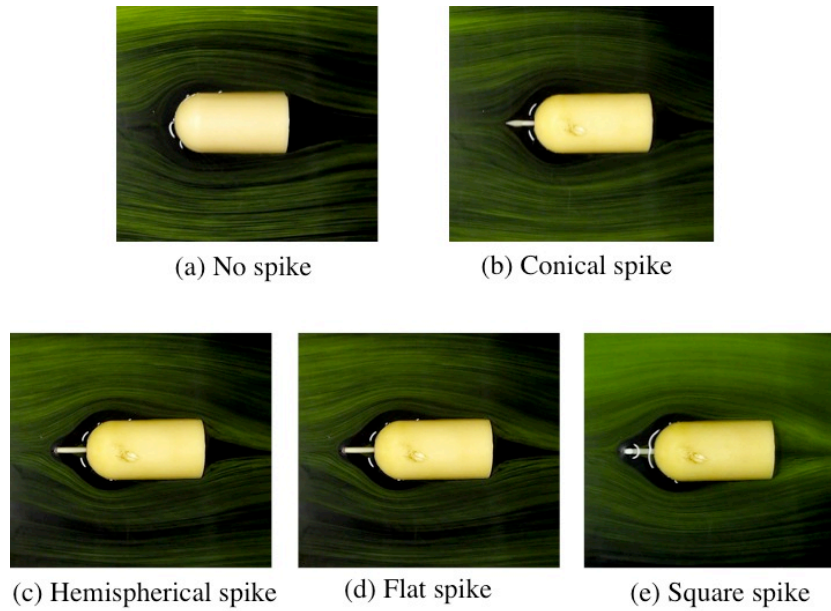


[Figure A.5. Flow field around the test models at  $Re=2277.6$ ]

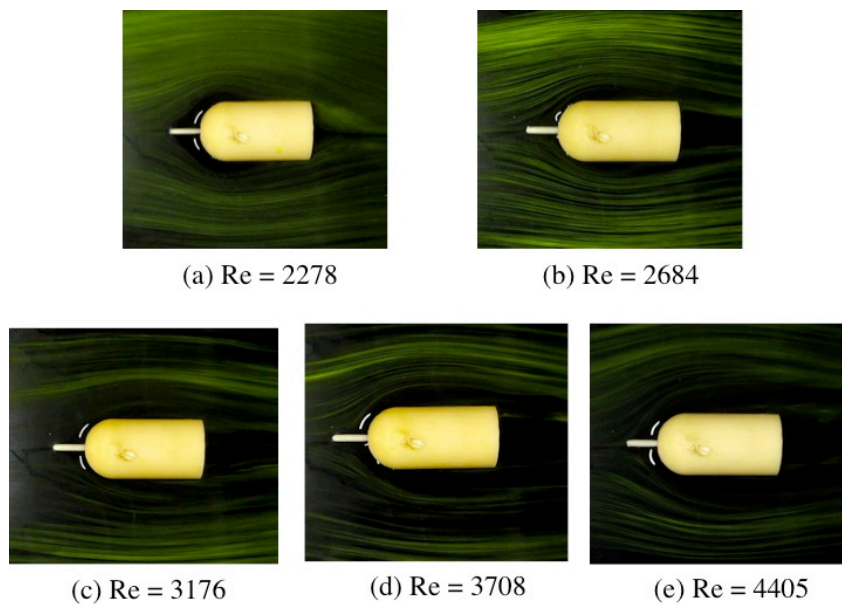


[Figure A.6. Flow field around the hemispherical spiked models at varying  $Re$ .]

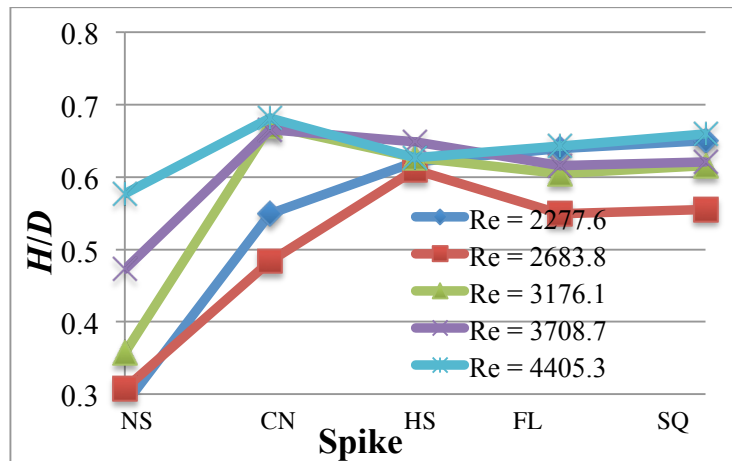


[Figure A.7.  $H/D$ -variation for various spikes.]

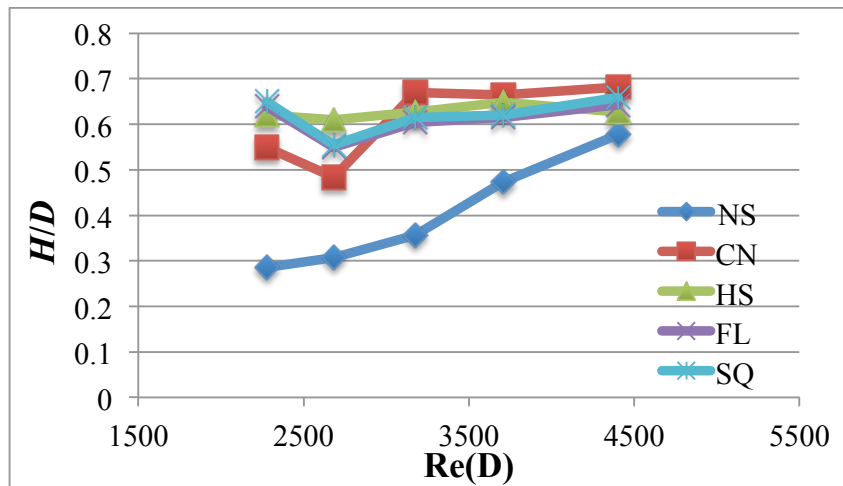


[Figure A.8.  $H/D$ -variation with  $Re$ .]

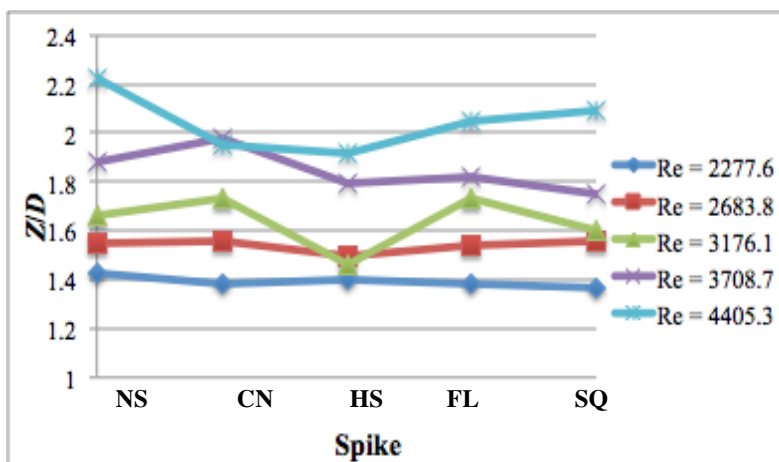


[Figure A.9.  $Z/D$ -variation for various spikes.]

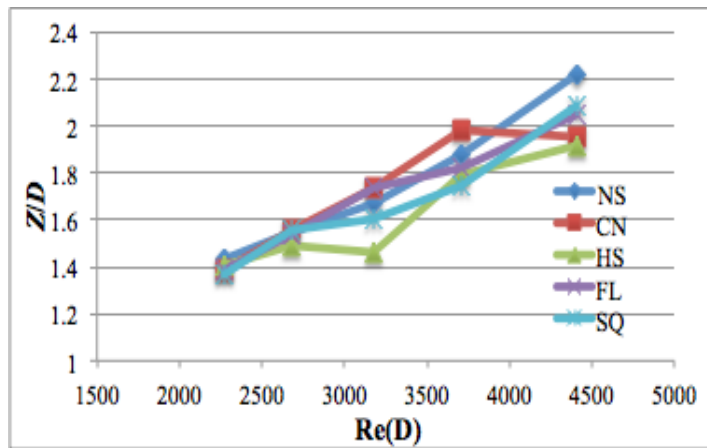


[Figure A.10.  $Z/D$ -variation with  $Re$ .]

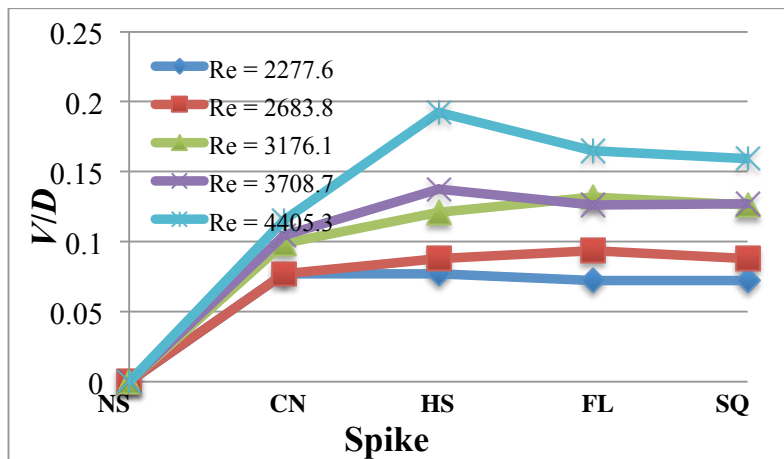


[Figure A.11.  $V/D$ -variation for various spikes.]

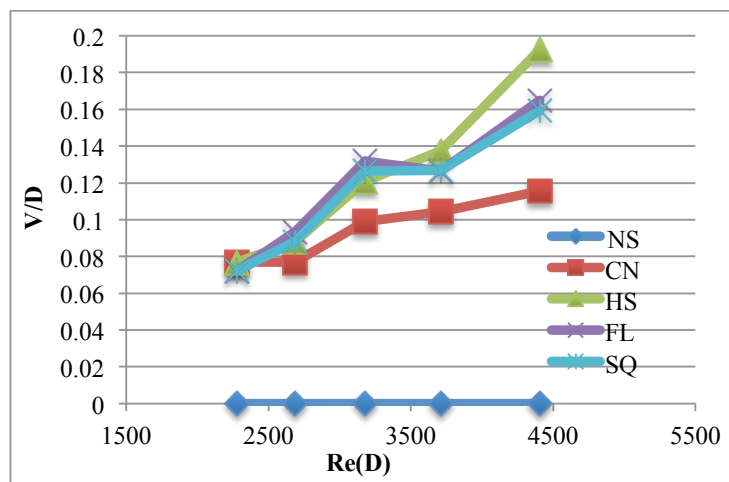


[Figure A.12.  $V/D$ -variation with  $Re$ .]

Flow around a blunt-nosed body with and without spikes of conical, hemispherical and square nose were visualized using a water flow channel over a range of  $Re = 2278$  to  $4405$ . The vortices at the attached end of the spikes were captured in the visualization. The flow field clearly exhibits the important features of the zone of influence  $Z$ , the head  $H$  and the vortex length  $V$ , at different Reynolds numbers. The pressure hill for the spike of hemispherical nose is found to be smaller, compared to the other shapes of the spike nose studied, at higher  $Re$ . Furthermore, the pressure hill heights for the flat-nosed spike with cylindrical and square stems are almost the same. The results clearly show that, hemispherical nosed spike is a potential candidate from drag reduction point of view for high speed flows pertaining to large Reynolds number, compared to the conical and flat nosed spikes, together with the effective utilization of a conical spiked nose for low speed applications, which haven't been discussed before.

**Case B:** -

Forward-facing spike has been identified as a passive flow control technique to render the strong pressure envelope at the nose to become weaker, thereby resulting in reduced pressure over the nose, as a consequence of vortices positioned at the root end, leading to drag reduction. Attention is focused on understanding this aspect of the flow process at low Reynolds number (incompressible flow). It is known that the vortices at the attached end of the spike are responsible for reducing the high-pressure over the nose, leading to drag reduction. These vortices at the root of the spike would also influence the vortices at the base. It would be of great significance for drag reduction if the functional dependence of the size of these vortices on the Reynolds number can be established. Therefore, in this study, emphasis is focused on ascertaining the dependence of the size of the vortices, at the root end of the spike attached to the nose of a blunt-nosed body and at the base of the body, on the flow Reynolds number and spike geometry, by visualizing the flow past a blunt-nose body with and without spike at Reynolds number  $3170$ . It is found that there is a specific length-to-diameter ratio for every spike nose-configuration, resulting in the largest vortex at the spike base and at body base, for a given Reynolds number, leading to significant reduction of drag.

The drag reduction of a blunt-nosed body plays an important role in both low-speed and high-speed applications. This assumes a lot of importance especially in the case of hypersonic flying objects because of the extremely high drag caused by the high-pressure zone at the nose, owing to the blunt nature of the nose geometry. In spite of this hostility the blunt shape is essential for the nose of the hypersonic vehicles to safeguard the body from ablation caused by aerodynamic heating. Considerable numbers of research articles are published in open literature with both experimental and computational studies on spiked blunt-nosed bodies at hypersonic Mach numbers (Ahmed et al. [7]). For reducing the drag, secondary objects projecting ahead of the blunt nose (forward-facing) has been found to be an effective method. These secondary objects are termed spikes, in general. When a spike is fixed to a blunt nose, it essentially shifts the forward stagnation point away from the surface of the blunt nose. Because of this, the extent of the positive pressure zone over the blunt nose comes down, leading to reduced drag. The flow process associated with the shifting of the stagnation point upstream of the blunt nose would result in weakening of the detached shock, and reduction of the extent of the zone influenced by the detached shock. However, for quantifying the dependence of the influence zone and the positive pressure zone over the nose, no information is available in the open literature. All the reasons given for the drag reduction, with the spikes, at hypersonic speeds are based on speculations about the zone of influence and the positive pressure zone over the nose, based on the end results obtained, mostly from direct measurements of force with wind tunnel balances. Therefore, there is an urgent need to understand the process associated with the flow over the basic body, with and without spike, for optimizing the spike geometry, resulting in efficient drag reduction. To gain an insight into the essential features of the flow physics associated with the drag reduction, it is essential to measure these parameters, if possible, directly. The present work is an attempt in this direction to assess and measure the extent of vortices near the fore-body stagnation area and in its wake, with and without spike, by direct means. For this, flow past the desired blunt-nosed body, with and without spikes, was visualized in a simple two-dimensional water channel, at a specific Reynolds number. The objective here is essentially to gain an insight into the important features governing the flow physics with the introduction of spike in front of the body nose, and its functional dependence on spike characteristics together with looking into the prospective application aspects governing the hypersonic flows.

Numerous researches in the past have proven that the positive pressure at the nose and the negative pressure at the base, together constitute the large drag associated with blunt nosed bodies meant for high-speed applications together with low-speed ones. Therefore, it is essential to reduce the positive pressure at the nose and the negative pressure at the base to bring down the drag (net force in the flow direction) over the blunt nosed body. Vast quantity of studies, reported in literature, investigated these aspects of positive pressure at the nose and the negative pressure at the base, in isolation. For example, the first report in open literature, which addresses both the nose and base fields, is the work by Takama et al. [30]. However, there is no direct address to the magnitude of the positive pressure at the nose and the base pressure at the rear, in this study. Also, the recent work of Kalimuthu [16], though addressed drag reduction of blunt-nosed body, focuses mainly on reducing the positive pressure at the nose. It has been found that there is an optimum length for a spiked blunt-nosed body at a specified Mach number, resulting in maximum drag reduction. However except for the optimum length of the spike no information about the flow characteristics, causing the maximum drag reduction, was presented. From vortex dynamics, it is known that larger the vortex the higher is the suction caused by it. This feature is largely considered as the reason for the modification of the pressure flow field, resulting in maximum drag reduction. It can be visualized that if the suction caused by the vortex at the base end of the spike is large, the oblique shock formed at the spike tip and traveling towards the body nose will be attracted towards the body. If the suction created by the vortex is just enough to make the shock become tangential to the shoulder of the body, as illustrated in Figure 1, it would result in the optimum reduction of the pressure field over the body-nose, resulting in significant reduction of pressure drag. Khurana et al. [29] performed the shallow water visualization experiments in a two-dimensional water channel around a blunt-nosed body, with and without spike, at Reynolds number 3070 and successfully captured the changes in flow field with the introduction of a spike, by quantification of different parameters namely zone of influence, pressure head and nose vortices.

To gain an insight into the flow process resulting in larger vortex at the root end of the spike, leading to increased suction resulting in weaker shock from the spike nose and reduced positive pressure magnitude and extent at the body-nose, it is essential to assess the dependence of the vortex size on the spike nose geometry. Furthermore, the impact of introducing a spike on the flow field at the base area of the body also

required to be addressed. Better the pressure field distributed over the nose area with spike at stagnation surface compared to concentrated zones, the weaker will be the suction at the body base. This would result in considerable reduction of drag. Therefore, it will prove to be of great value and importance to understand the flow process responsible for total drag reduction (including nose and base) achieved with spike. Moreover, visualizing the vortex at the spike base at higher velocities is difficult because of extremely high inertia. Keeping this in mind, in the present work, vortex-size variation with spike-nose geometry and length-to-diameter ratio has been investigated in a water flow channel at Reynolds number 3170, for different spike geometries shown in Figure A.13. Here  $a$  represents the side of the spike with square nose,  $d$  the spike diameter at its root,  $D$  the main-body diameter,  $l$  the spike length from nose till root,  $\theta$  being the spike nose-cone angle and  $\phi$  representing the characteristic diameter.

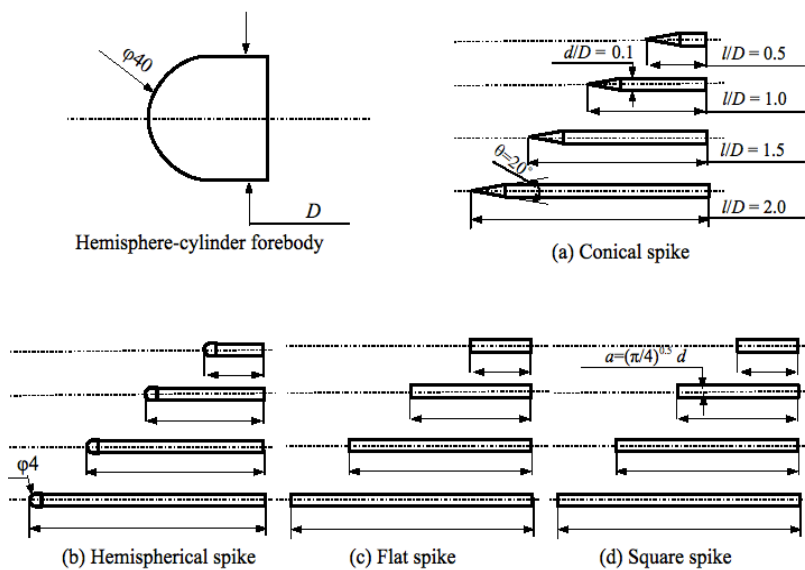


[Figure A.13. Schematic of the basic body and spike configurations.]

The videos recorded clearly exhibit the flow field comprising the vortices generated ( $V$ ) at the body nose (spike base) and in the wake region (body base), as illustrated as flow field nomenclature in Figure A.14. The various quantified parameters in a typical flow field around a spike body can be characterized as  $H$  representing the pressure head in front of the fore-body nose,  $V$  representing the

vortex length near forebody nose (at the root end of spike),  $Z$  depicting the zone of influence, that is the extent of flow turning around the forebody shoulder and  $W$  the vortex length or the expanse of wake zone at the rear of the body from the trailing edge towards the mid-section at the downstream.

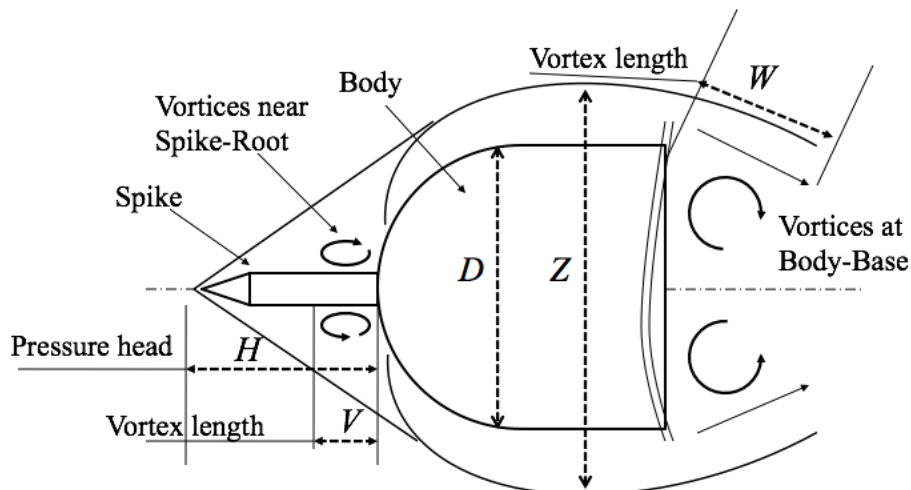


[Figure A.14. Flow field nomenclature.]

The testing models have been prepared for the two-dimensional flow visualization; with the nose of the body (with and without spike) facing the flow in the plane of the channel, together with the height of the model ( $z$ -dimension) more than the depth of the flow. This shall enhance the visualization procedure determining all the necessary flow features by utilizing the free surface of the wave in the channel. The visualization results from the shallow water experiments have been presented in Figures A.15-A.18, with and without spike, for the varying length-to-nose-diameter ratios ( $l/D$ ) from 0.5 to 2.0. Figure A.15 shows the flow field for the blunt-nosed body, with different spikes, for  $l/D=0.5$ . The change in the streamlines deflection caused by the spike in front of the nose can be easily seen. The high-pressure area that envelops the nose of the basic body has been narrowed down considerably by the streamlines deflected towards the body, by the spike. The streamlines that get deflected towards the shoulder of the body are again get deflected towards the low-pressure region of the wake. The flow field with different spikes, in front of the forebody for  $l/D = 1.0$ , is given in Figure A.16. With the increase in spike  $l/D$ -ratio, the deflection of the streamlines from the spike nose gets nearer to the shoulder of the forebody, confirming the higher suction created by the formation of the larger vortices

around the attached end of the spike. Also, the flow gets attracted towards the base of the body owing to the low-pressure location in the wake. On further increasing the  $l/D$ -ratio to 1.5 (Figure A.17), it is seen that, the flow is nearly tangential to the forebody shoulder, signifying an optimum value of  $l/D$ , for the generation of sufficiently larger vortices, which attracts the flow towards the nose-shoulder, thereby reducing the positive pressure level and extent over the nose. Beyond  $l/D = 1.5$ , the deflected streamlines of flow starts drifting away at the spike nose and then re-attach near the spike root location resulting in negligible size of vortices as is clear from Figure A.18. Contrary to this fact, the flow downstream of the forebody stays near to body base in the wake region, as the extent of vortices (low pressure region) behind the body decreases with increasing  $l/D$ -ratio.

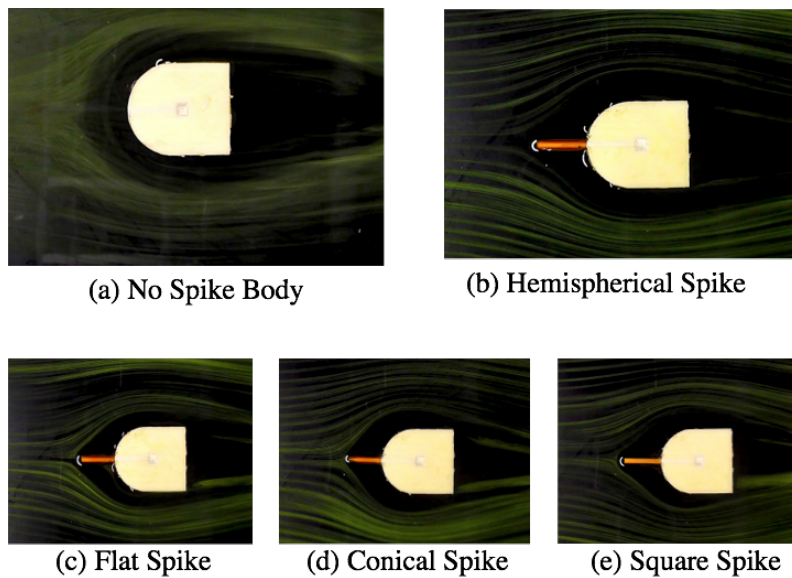


[Figure A.15. Flow field for various test cases for  $l/D = 0.5$ .]



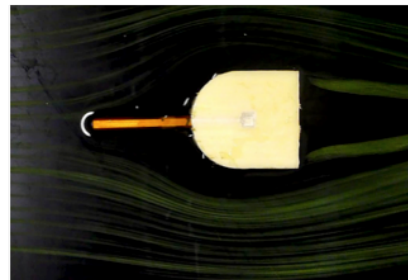
(a) Hemispherical Spike



(b) Flat Spike



(c) Conical Spike



(d) Square Spike

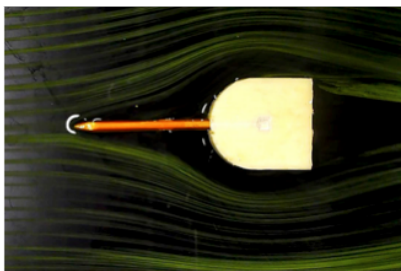
[Figure A.16. Flow field for various test cases for  $l/D = 1.0$ .]



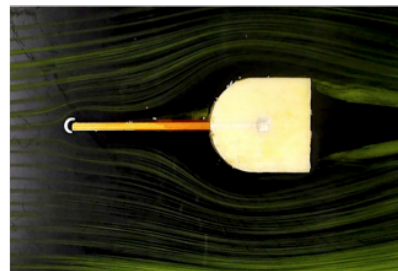
(a) Hemispherical Spike



(b) Flat Spike



(c) Conical Spike



(d) Square Spike

[Figure A.17. Flow field for various test cases for  $l/D = 1.5$ .]

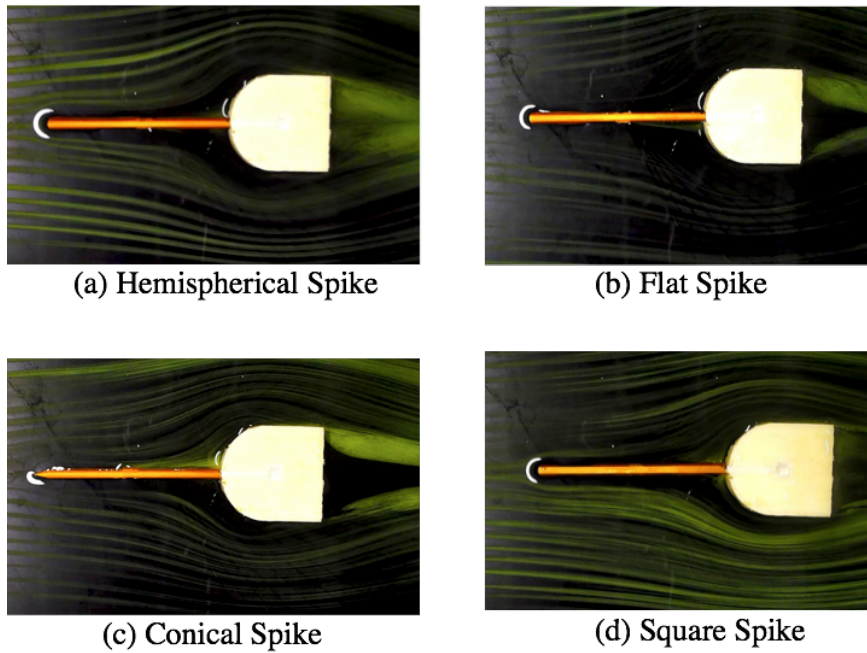


[Figure A.18. Flow field for various test cases for  $l/D = 2.0$ .]

The quantification of flow field parameters (schematically described in Figure A.14) has been performed from the visualization pictures (Figure A.15-A.18). Figure A.19 shows the variation of pressure-head, non-dimensionalized as  $H/D$ , around the nose of the basic body, for various spike configurations and spike  $l/D$ . The ordinates of these graphs represent the non-dimensional lengths and the abscissa represents the type of spike-nose. For ease in identification and reference purpose, the key spike configurations have been abbreviated as NS for no spike body, CN for body with conically nosed spike, HS for body with hemispherical nosed spike, FL for body with flat nosed spike, and SQ for body with squared nose spike.

It is clearly seen that, introduction of the spike increases the pressure head in front of the nose monotonically with increase in  $l/D$ , from a characteristic value of 2.1 to about 0.7. The point to be noted here is that the pressure head ( $H/D$ ) is estimated from the nose of the body and not from the nose of the spike (as shown in Figure A.14), therefore the characteristic value is more than the basic configuration without spike, but decreases with the introduction of the former. The actual quantified value for the pressure head ahead of the spike nose is significantly lesser as compared to that in case of no-spiked body in front of the nose. Moreover, as can be understood from the captured pictures, the spike completely alternates the high-pressure region spread over a large area of the nose and shoulder of the basic body without spike, to a very small

pressure envelope existing only in front of the spike nose. The flow after turning from the spike nose, when reaches the downstream encounters a recirculation resulting in the generation of vortices at the spike root.

Zone of influence (non-dimensionalized as  $Z/D$ ) has been plotted in Figure A.20 around the nose for the base geometry and with various spike configurations and is plotted as a function of spike  $l/D$ . As anticipated, the zone of influence is proved to be dependent on the extent of flow turning at the nose. Spike causes the flow to turn with a smaller radius of curvature. This makes the flow to move towards the shoulder of the body resulting in the decrease in magnitude of zone of influence.  $Z/D$  witnesses a sudden drop in value, with the test cases of spiked configurations registering a minimum for hemispherical spike. The cylindrical spike with flat end seems equally worthy in bringing down the extent of  $Z/D$ , unlike the spikes with square and conical nose. This trend continues till  $l/D = 1.5$ , beyond which the flow gets dissipated owing to significant reduction in pressure envelope, which can be seen as an unusual reduction in  $Z/D$ .

Quantification of nose vortices around the spike root and stagnation area and those generated in the wake region have been carried out, by measuring these values from the visualized pictures. Figures A.21 and A.23 show the flow field around the near-nose region with ( $l/D = 1.5$ ) and without spike, and the flow field in the wake region with ( $l/D = 2.0$ ). These pictures of the flow field clearly exhibit the vortex length  $V$  and  $W$ , respectively, which were measured by projecting the visualization pictures on screen, for all the models studied. Figures A.22 and A.24 depicts the non-dimensional ( $V/D$  and  $W/D$ , respectively) plots of vortex size variations, with spike-nose configurations for spikes of different  $l/D$ -ratios, over the nose and wake region. The ordinates of these graphs represent the non-dimensional lengths and the abscissa represents the type of spike-nose.

Considering the vortex-size variation around the nose, the representative and optimum  $l/D$ -ratio has been estimated to be 1.5 for the present case of Reynolds number. From Figure A.22, it can be seen that, a conical aerospike, irrespective of  $l/D$ -ratio, is not capable of generating vortices near the spike root, whereas a hemispherical spike reduces the zone of influence drastically (bringing the deflected flow near the shoulder). This may be envisaged as a direct indication of reduced positive pressure over the nose of the basic body. The generation of the vortices near the spike root results in low-pressure recirculation region, which attracts the deflected

flow, thereby keeping it near the shoulder. The radius of curvature of the approaching streamline is reduced; the deflection of the streamlines is towards the shoulder of the basic body, resulting in a narrow zone of the positive pressure hill at the nose. Therefore, integral of this positive pressure over the nose assumes lesser magnitude, compared to the positive zones for the spikes with conical or flat face, resulting in relatively smaller drag.

The wake-region behind the forebody is directly influenced by the magnitude of the pressure on its nose and the deflection of the flow. The higher the magnitude of positive pressure on the nose, the stronger the deflection and larger the wake region, consequently resulting in increased drag. Figure A.23 focuses on the flow field showing the wake region with ( $l/D = 2.0$ ) and without spikes, and Figure A.24 quantifies the magnitude of the vortex lengths by taking an average of the left and the right vortices (depicted in Figure A.23), generated on either side of the mid-span, to avoid inaccuracy in case the wakes are not symmetrical. The equivalent vortex length is given by  $\{(W_{\text{right}}+W_{\text{left}})/2\}$ , which is plotted as a non-dimensional length ( $W/D$ ) against the spike type, for various  $l/D$ -ratios, where *right* as subscript denotes the wake zone expanse from the right trailing edge of the body before joining the mid section of wake region at far downstream (as seen from top) and *left* as subscript denotes the wake zone expanse from the left trailing edge of the body before joining the mid section of wake region at far downstream (as seen from top). From Figure 14 it can be concluded that, a spike (a forward-facing object in front of the nose), irrespective of its nose-type or size, is capable of reducing the low-pressure level behind the forebody by significantly affecting the flow physics. For  $l/D = 0.5$ , the deflection provided by the spike to the flow remains considerably away from the body and cannot reach the wake region in spite of the existence of large suction zone at the base. Similar is the case with a conical spike, which provides larger radius of deflection to the streamline. For a flat-faced spike, the radius of deflection gets reduced, resulting in lesser confinement zone of the wake vortices, whereas hemispherical spike stands as the sole candidate capable of positively affecting the wake region, and simultaneous reduction in drag.

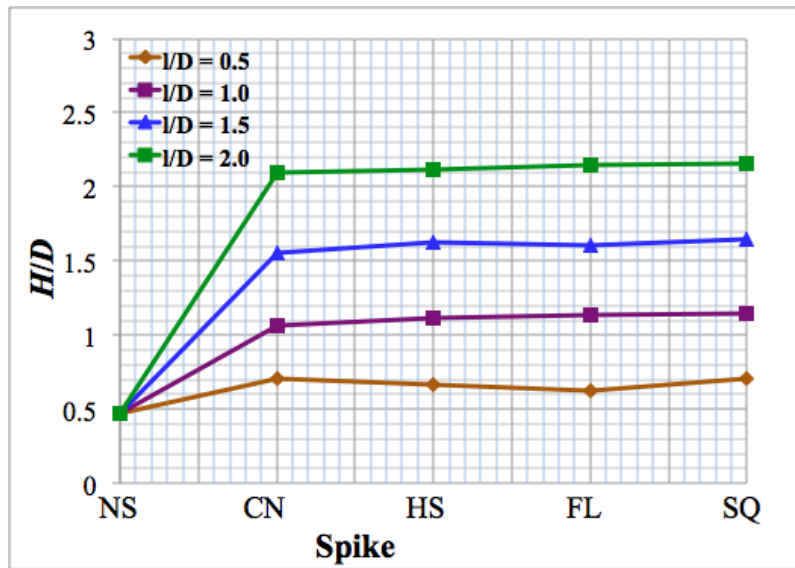


[Figure A.19.  $H/D$ -variation around the nose for various spikes.]

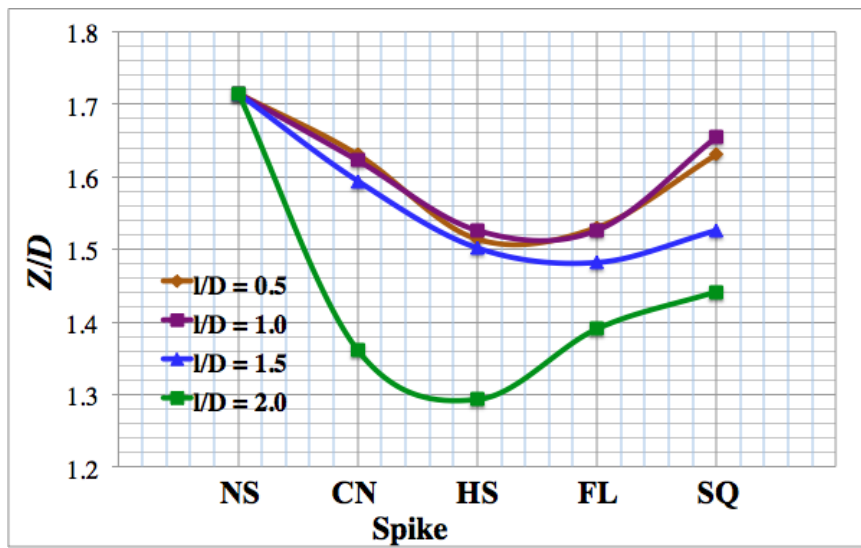


[Figure A.20.  $Z/D$ -variation around the nose for various spikes.]

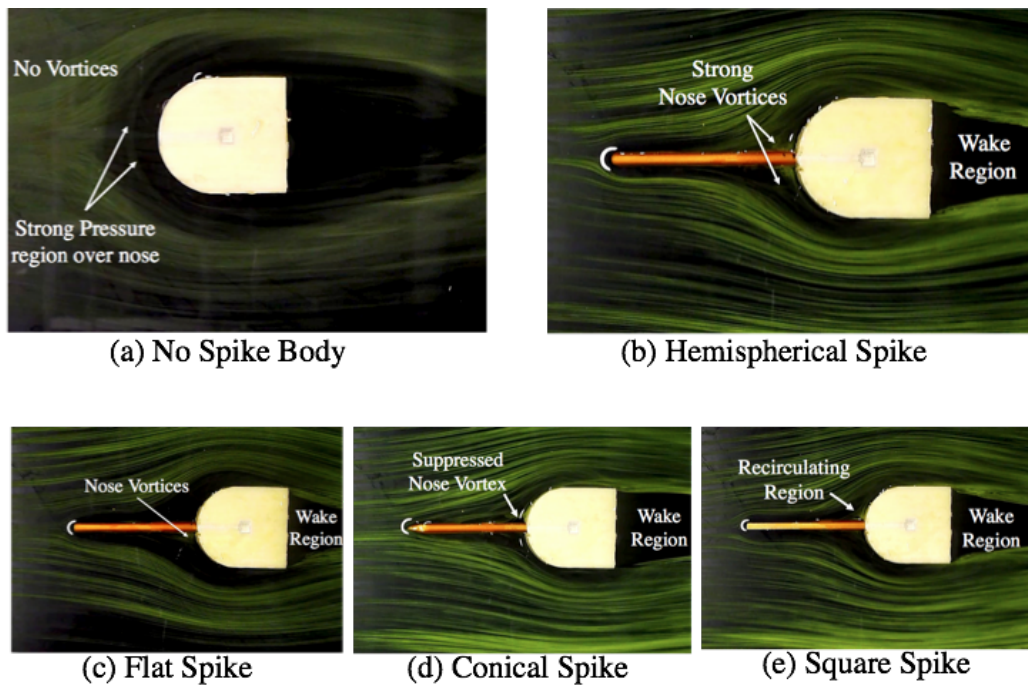


[Figure A.21. Flow field showing near-nose region with ( $l/D=1.5$ ) and without spike.]

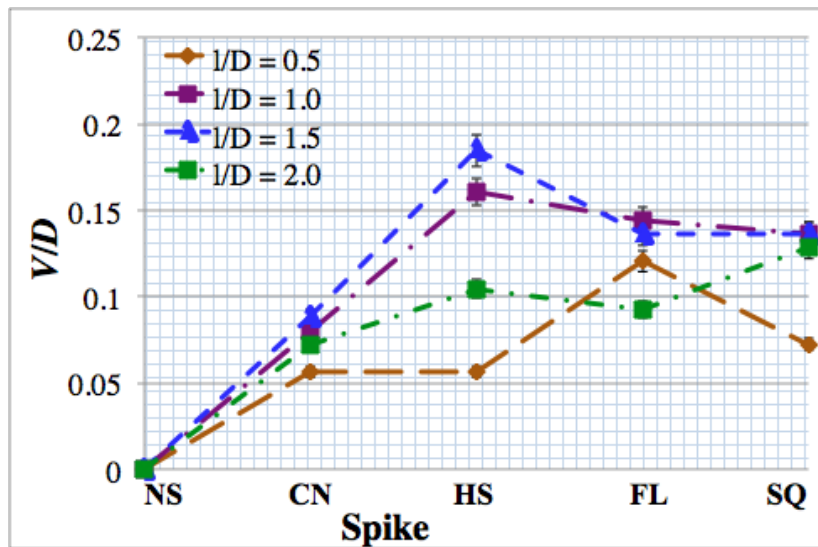


[Figure A.22.  $V/D$ -variation around the nose for various spikes.]

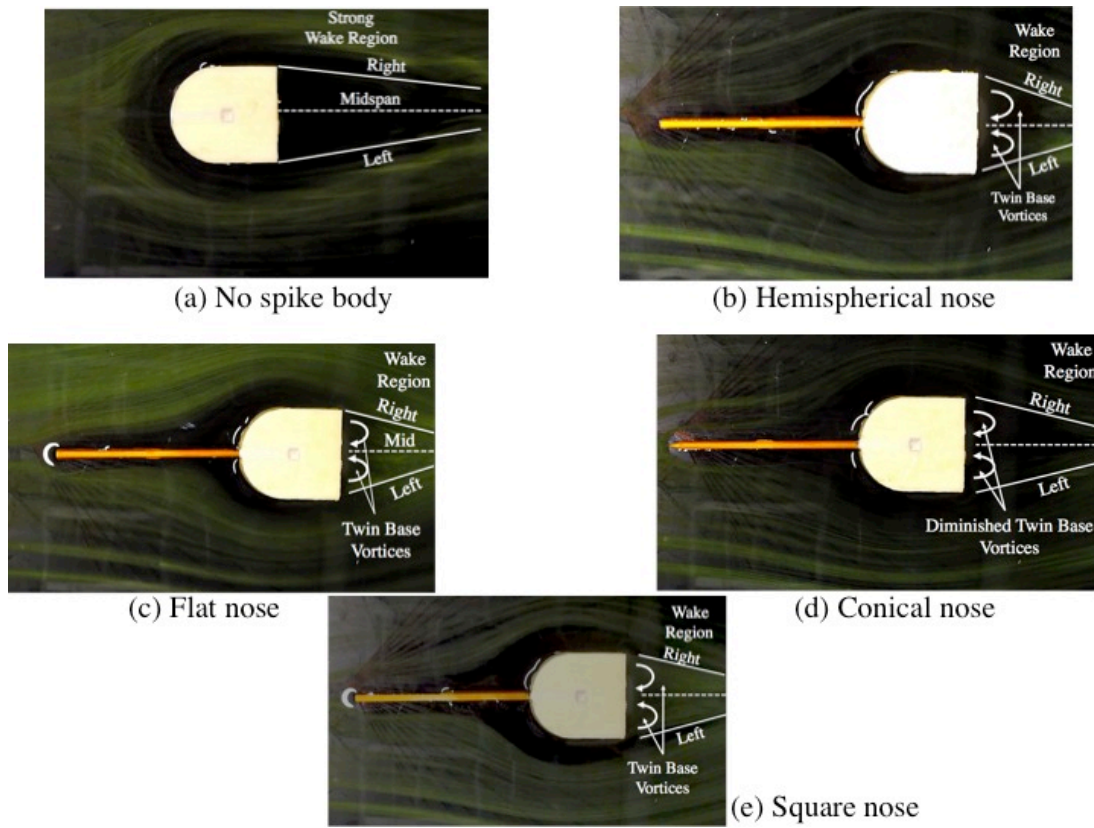


[Figure A.23. Flow field showing wake region with ( $l/D=2.0$ ) and without spike.]

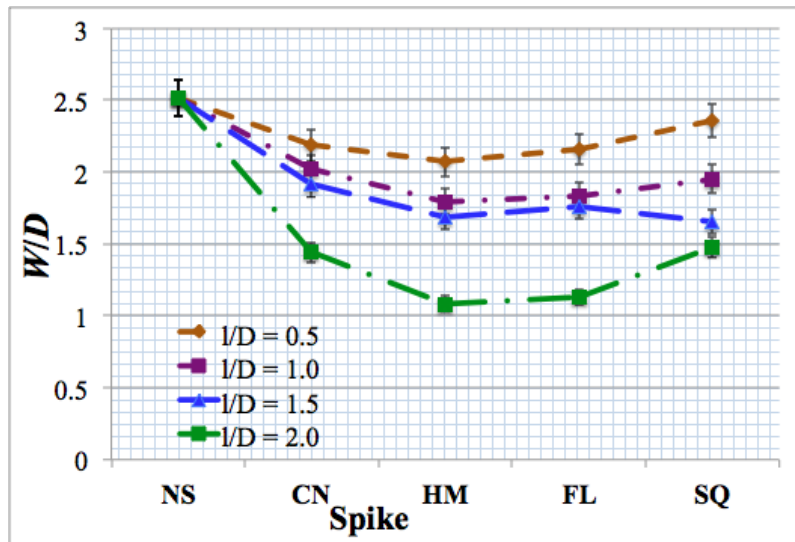


[Figure A.24.  $W/D$ -variation around the base for various spikes.]

Flow field around a blunt-nosed body, with and without spike, for different spike nose-configurations and varying  $l/D$ -ratio (spike length/body-nose-diameter ratio) were visualized using a water flow channel. The vortices near the stagnation area (spike root) of the spiked body and in the wake region were captured in the visualization. Vortex characteristic lengths  $V$  and  $W$  were quantified by measuring them from the visualized pictures. The results clearly show that, spike with hemispherical nose is a potential candidate from drag reduction point of view, compared to the conical and flat nosed spikes. It is found that, there is a specific length-to-diameter ratio for every spike nose-configuration, resulting in the largest vortex at the attached end of the spike, at a given Reynolds number. Furthermore, the dependence of vortex strength at the base of the main body has also been found to be a strong function of the spike length-to-diameter ratio, for the current low-speed incompressible flow indicating its potential for such applications. Larger the  $l/D$ -ratio weaker will be the vortices at the base and smaller will be the confinement zone of the wake region.

**Case C: - Simulating a Hypersonic Flow in a Shallow Water Channel employing Hydraulic Analogy**

A spike attached to the nose of the body, as a passive control device, is considered effective for reduction of drag, facilitating the reduction in aerodynamic heating that the body has to suffer at very high-speeds. An aerospike is capable of changing the flow field (especially the high-pressure envelope at the nose) around a blunt-nosed body, resulting in a reduced pressure, leading to reduced drag. The pressure reduction caused by the spike is dictated by the vortices formed at the junction of spike attachment with the nose. The detached weak foreshock at the nose of the body is rendered oblique, by the spike, and the recirculation zone caused by the vortices at the spike root attracts the oblique shock towards the body. This renders the shock to become weaker. Thus, higher the suction caused by the vortex, the weaker would be the shock. Weakening of the shock results in reduced pressure over the body nose and this reduced pressure results in reduced drag at stagnation nose area. Though considerable amount of research has been reported on this problem, almost all of them are based on force measurement in wind tunnels and visualization of the waves with schlieren technique. Therefore, the vortices dictating the pressure field have not been

visualized so far. This is because visualization and hence quantification of vortices through experiments in hypersonic flow is not practical owing to large inertia. Although numerical study is capable of estimating the mechanism, it requires significant efforts in terms of computational power (space and time), and also needs to be validated through experimental results, to gain confidence about the results obtained. Therefore, there is an urgent need to understand the formation and size of the vortex at the root end of the spike to understand the process causing drag reduction. To directly address this issue and to investigate the effectiveness and prospects of an experimental technique for qualitative investigation, a visualization study was performed to visualize the generation and the characteristics of the vortices around an aerospike attached to a typical hemispherical-nosed cylindrical body, shown in Figure A.25, using a shallow water flow. To simulate flow analogous to a Mach 6 hypersonic air stream, a shallow water stream with Froude number 6, in a rectangular water channel facility was employing hydraulic analogy (Rathakrishnan 2007 [6]). The flow field around the blunt-nosed body, with and without spike was visualized in the shallow water stream and recorded on videotape. The presence of two oppositely rotating vortices family (clockwise and counter-clockwise), which is deemed as the key phenomena for favorably modifying the flow field, have been successfully visualized and analyzed around the spike root in front of the body nose.

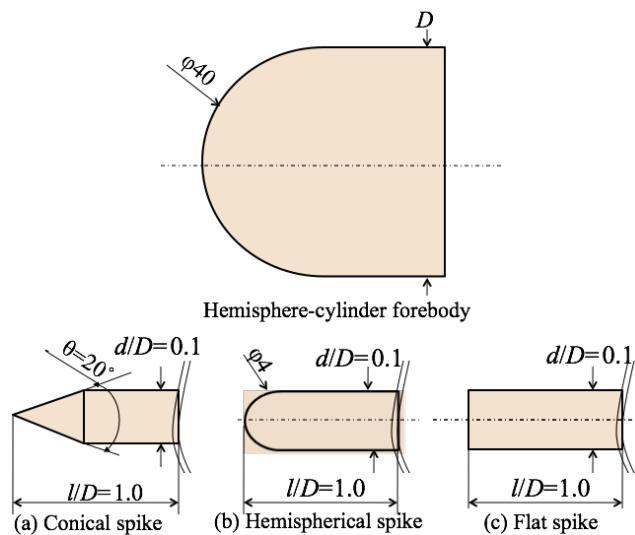


[Figure A.25 Test geometry with spike configurations.]

## Results and Discussion

The tests of the present study were carried out at equivalent Froude number, evaluated as  $\{v/(gh)^{1/2}\}$ , of 6 (analogous to Mach 6 air stream, using Hydraulic Analogy). Figures A.26-A.29 show some representative visualization pictures of the flow field captured from the water channel experiments, for with and without spike cases. The key flow features of equivalent hydraulic jump (analogous to shock in gas-flow) in front of body nose and emanating from the spike-nose, regenerating waves from body shoulder, equivalent expansion waves around the wake region together with the presence of oppositely rotating vortices (one clockwise and other counter-clockwise) positioned at spike root have been successfully observed. In spite of the limitations of water channel facility and hydraulic analogy, in correlating and simulating the conditions of a hypersonic gas-flow accurately, a qualitative insight into the flow physics, with the technique being capable of serving as a low cost, quick and fairly accurate visualization technique, can be considered for preliminary investigation for a study.

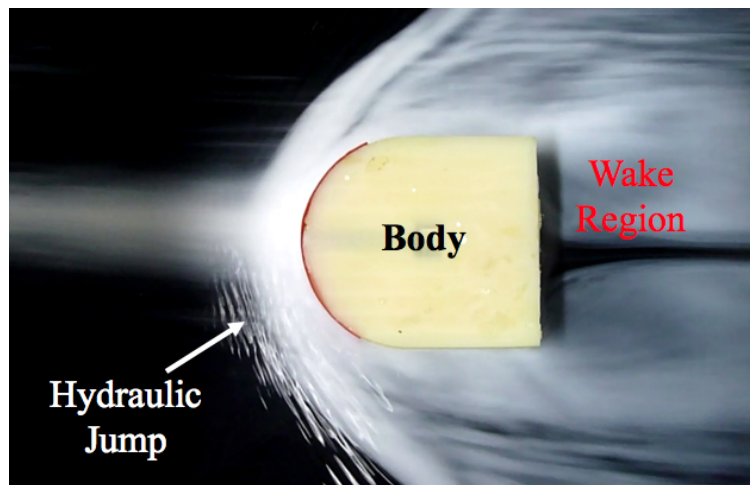


[Figure A.26 Flow field around the basic body (no vortices).]

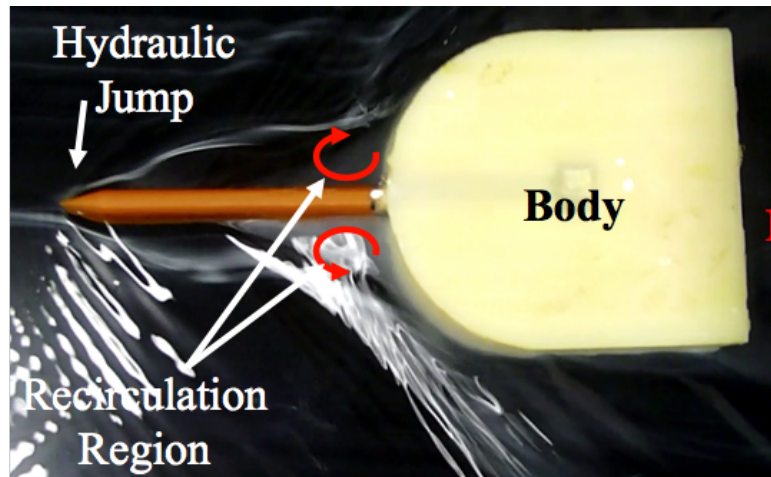


[Figure A.27 Flow field for spiked with conical-nose.]

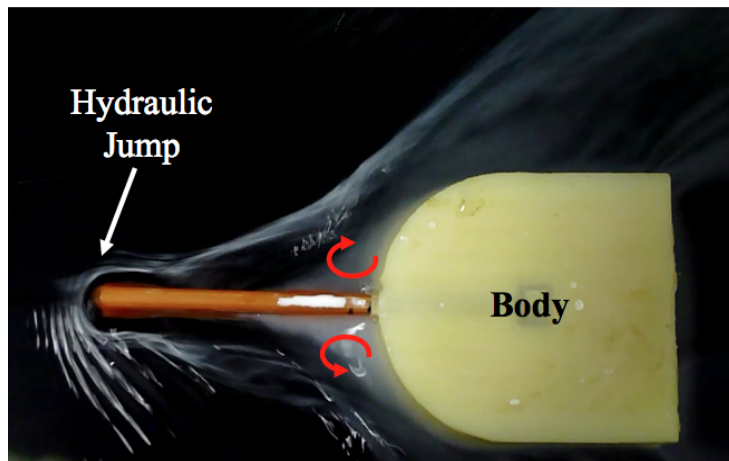


[Figure A.28 Flow field for spike with flat-nose.]

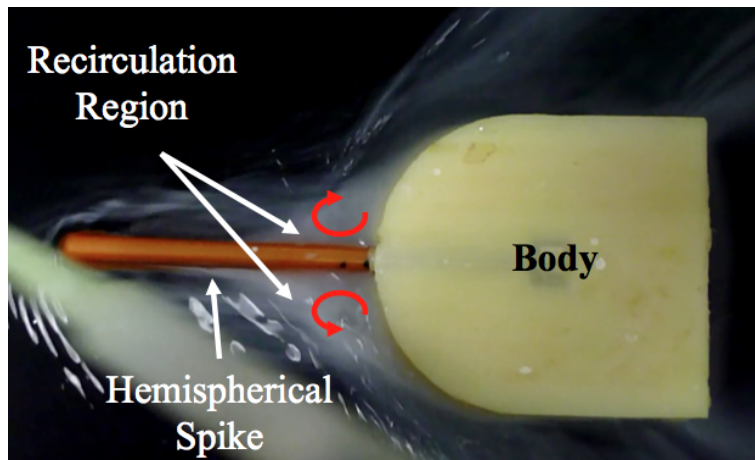
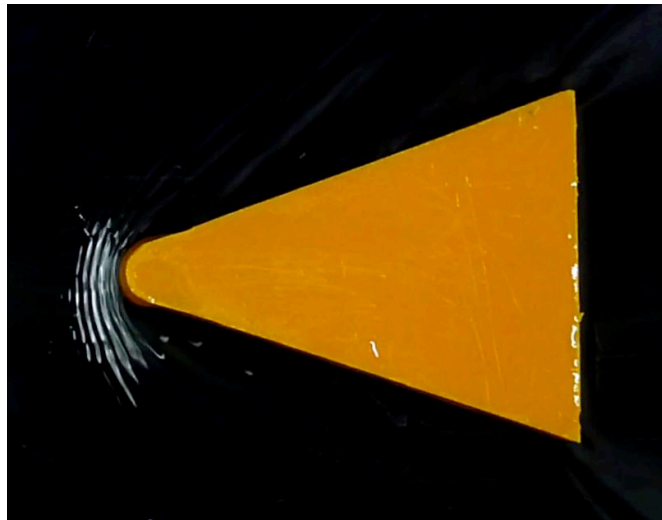


[Figure A.29 Flow field for spike with hemispherical-nose.]

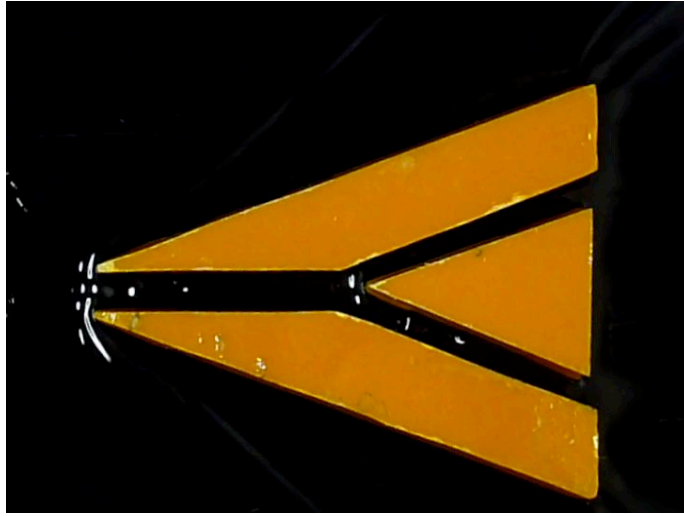
---

**Case D: - Simulating a Hypersonic Flow in a Shallow Water Channel around Breathing Blunt Nose Models**

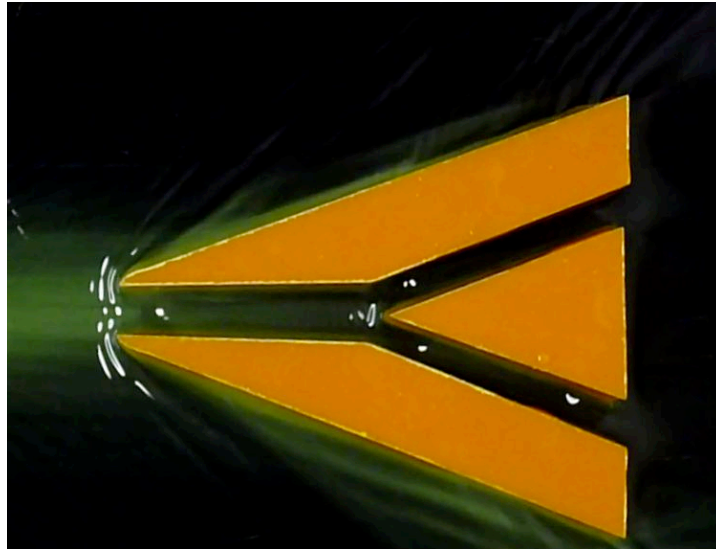
Similar experiments were performed around two-dimensional lifting-body configuration model at an analogous Froude number of 7 (corresponding to hypersonic experiments at Mach 7), with and without holes, as shown in Figure A.30, to obtain a qualitative understanding about the behavior of flow inside the channel. The videos recorded clearly exhibit the flow field at the body nose, through the channels and in the wake region (body base) with the time-captured images been illustrated in Figures. A.31-A.34.



(a) No hole body



(b) Body with  $\phi 5$  mm hole



(c) Body with  $\phi 7$  mm nose hole

[Figure A.30. Typical models for water channel visualization.]

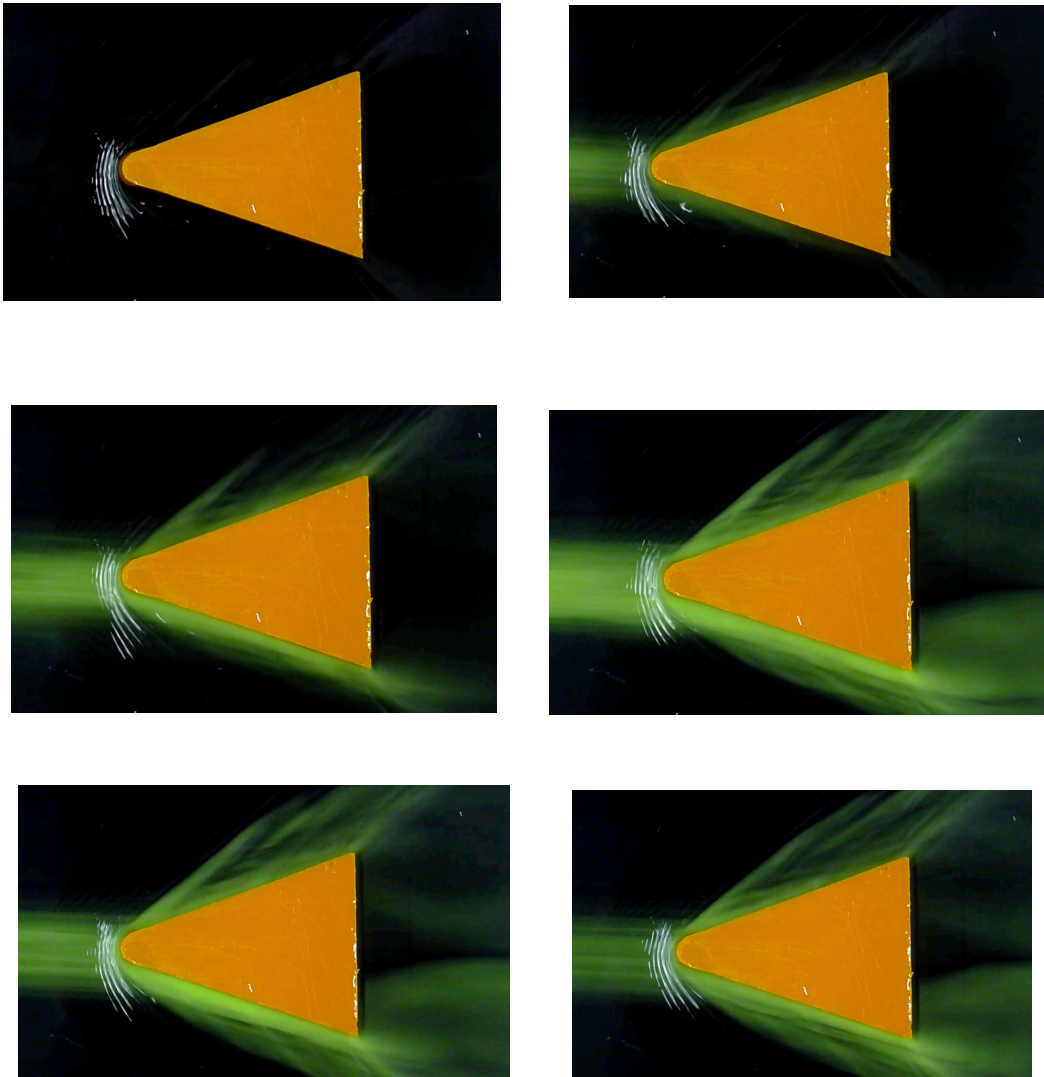


[Figure A.31. Time-captured images around no-hole body at  $\alpha=0^\circ$ .]

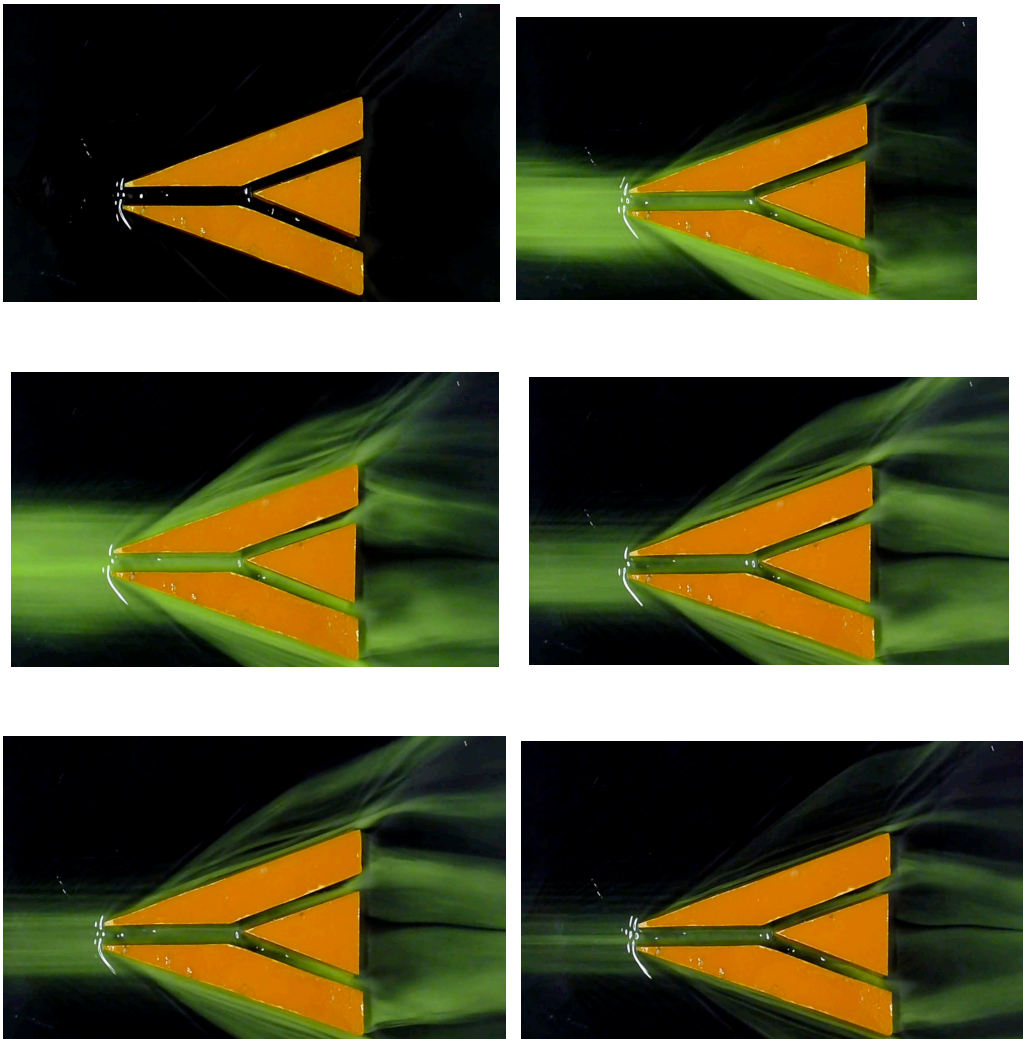


[Figure A.32. Time-captured images around  $\phi 5\text{mm}$  nose hole geometry at  $\alpha=0^\circ$ .]

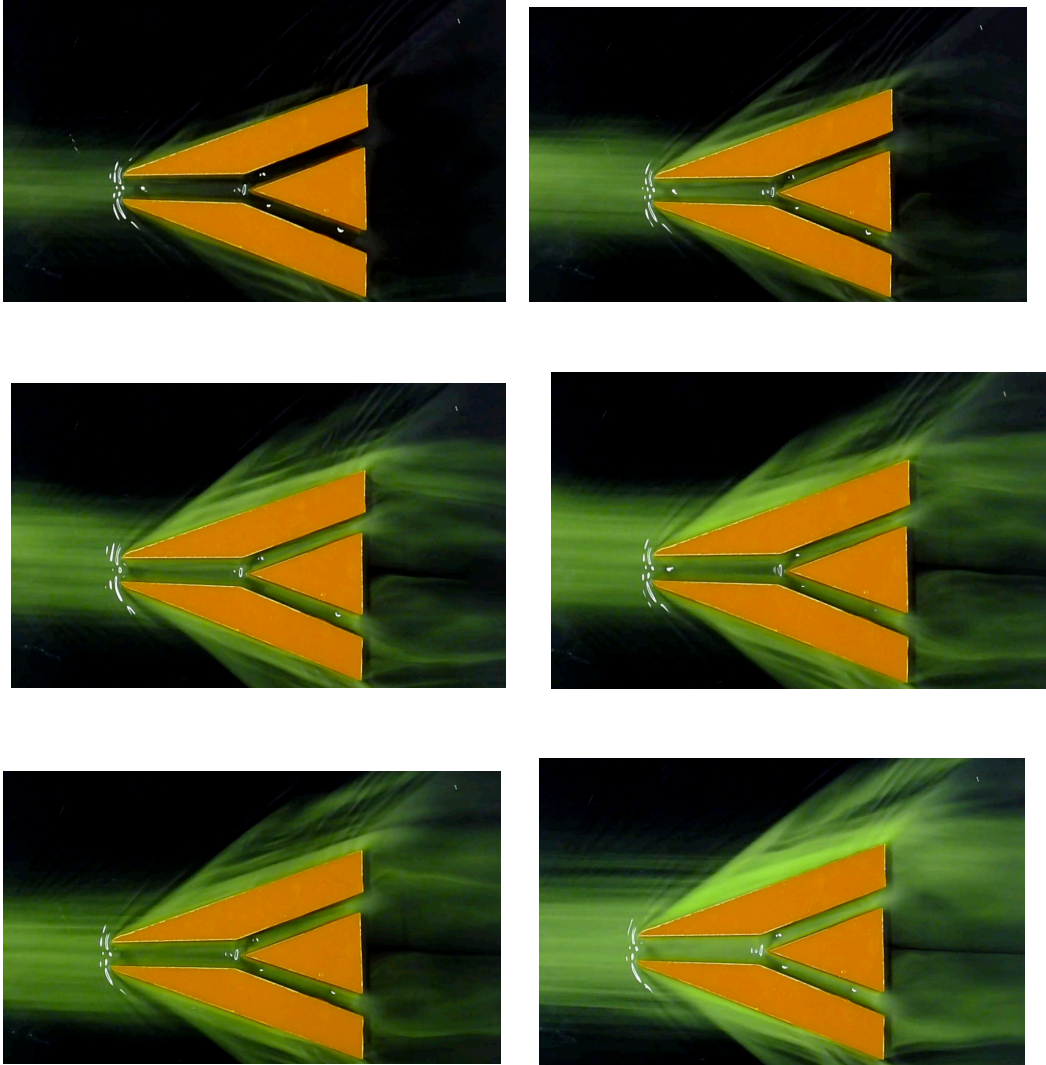


[Figure A.33. Time-captured images around  $\phi 7\text{mm}$  nose hole geometry at  $\alpha=0^\circ$ .]

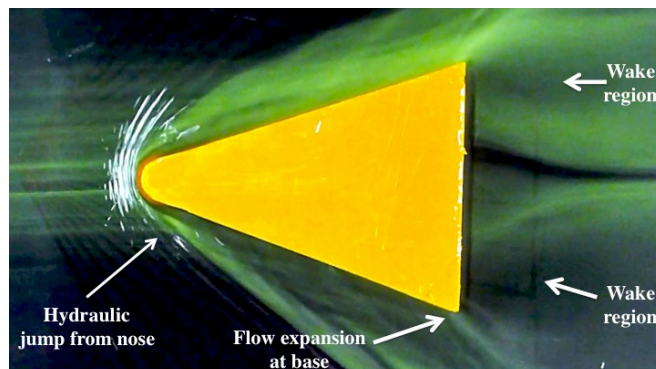
Figure A.34 represents the captured images from the videos of the experiments with the necessary details about the flow field to provide an enhanced understanding of the flow physics and the development of flow with the introduction of the hole on the nose, to be compared with the Schlieren pictures obtained from during the wind tunnel experiments. Figure A.34(a) shows the representative lifting body configuration, which when placed in the flow in water channel, generates hydraulic jump (analogous to shock wave in gas flow, bow shock in this case). Figure A.34(b) shows the schematic of the flow field around the no-hole body. From the streamlines, it can be seen that a hydraulic jump results in high pressure zone at the

nose and the wake region (extremely low pressure area) existing behind the body, results in flow expansion at the trailing edge of the body, with the flow being forced from high pressure region (behind the expansion waves) towards the base wake area, yet the expanse of the suction zone remains finite. The flow field constitutes a highly positive  $C_p$  at the nose (location A-A) and negative  $C_p$  (location C-C) at the base.

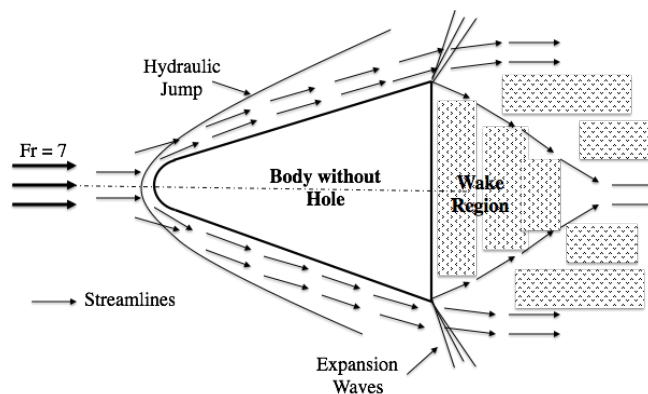
Figure A.34(c) shows the flow field around the body with  $\phi 5\text{mm}$  hole at the nose, meant for bleeding the air and Fig. A.34(d) depicting the schematic of the flow field. The flow field can be considered identical with the one visualized in wind tunnel. It can be seen that the flow is bled inside the channel and the shape of the hydraulic jump gets modified at the nose, which is in correlation with the Schlieren picture. The hydraulic jump becomes weaker in strength and poses reduced pressure (reduced  $C_p$  at location A-A) at the nose. The flow is bled from the nose towards the channel, and encounters another stagnation zone (about mid-way of the length of the model) from where it gets divided into two branches. At this location B-B, the flow encounters stagnation and contributes to the drag offered to the flow, which is the function of the flow rate bled at the nose. The jets discharged at the base from the channel encounters sudden expansion at the exit of the channel and mixes with the flow (as highlighted by streamlines in Fig. A.34(d)) past the expansion jet from the base of the body towards the wake region (as highlighted in Green in Fig. A.34(d)). The jets from the channel and its mixing at the base plays a key role in reducing the size of wake region (represented by a shrank wake region) and increasing its pressure at location C-C. Reduction in magnitude of positive  $C_p$  at the nose (A-A), with a moderate drag offered at dividing B-B location and reduction in magnitude of negative  $C_p$ , consequently results in the reduction of resultant pressure acting on the body in the direction of the flow. This effect can be clearly seen as a factor for the reduction in drag coefficient at  $\alpha=0^\circ$ .

Figure A.34(e) shows the flow field with the body with  $\phi 7\text{mm}$  hole at the nose with the schematic shown in Fig. A.34(f). The analogous hydraulic jump moves further inside of the channel, with two different jumps emanating from the outer edge of the nose, resulting in further decrease of pressure (directly proportional of nose diameter) and  $C_p$  at the nose (location A-A). With the increase in nose diameter to

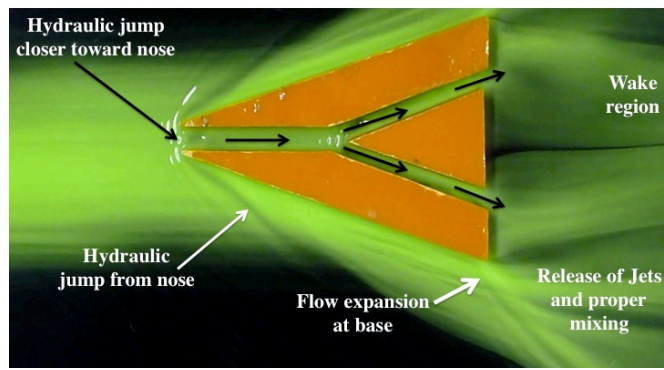
$\phi 7\text{mm}$ , the flow rate also increases, thereby offering increased resistance at the secondary stagnation region (location B-B), more than  $\phi 5\text{mm}$  case. The release of the increased sized jets at the base results in improper mixing with the flow past the expansion wave from the base, consequently resulting in increase of the wake region at location C-C (represented by a bloated wake region), effectively not contributing to its purpose of existence. Further reduction in magnitude of positive  $C_p$  at the nose (A-A), with significant drag offered at dividing B-B location and increase in magnitude of negative  $C_p$ , consequently results in the increment of resultant pressure acting on the body in the direction of the flow. This correlates with the wind tunnel results, making the drag coefficient more than  $\phi 5\text{mm}$  case, corroborating the existence of limit of bleeding from the nose, resulting in maximum reduction in drag coefficient, beyond which any further increase in hole diameter adversely affects the same and will add to the drag force offered to the body.



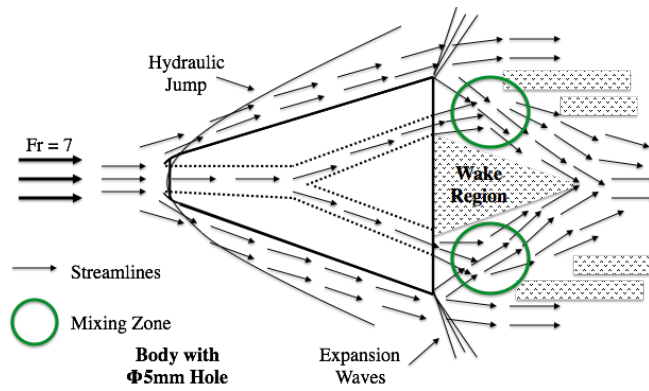
(a) Model without hole.



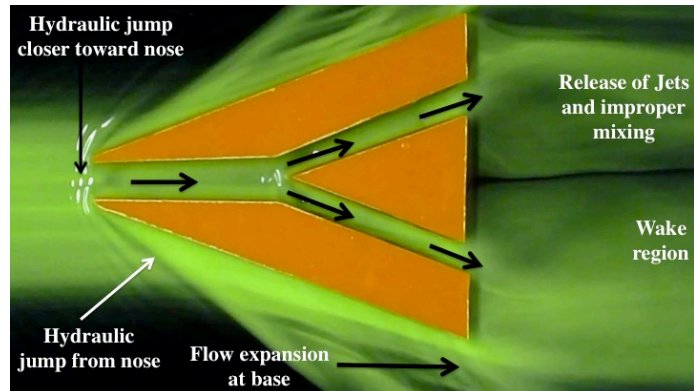
(b) Schematic diagram of flow field without hole.



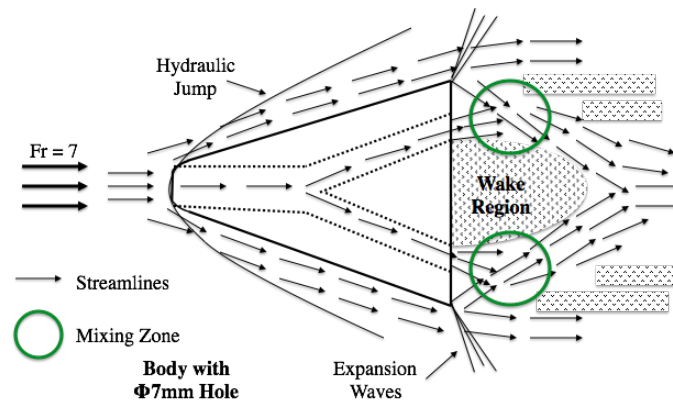
(c) Model with  $\phi 5$  mm hole.



(d) Schematic diagram of flow field with  $\phi 5$  mm hole.



(e) Model with  $\phi 7$  mm hole.



(f) Schematic diagram of flow field with  $\phi 7\text{mm}$  hole.

[Figure A.34. Two-dimensional flow field around representative geometries at  $\alpha=0^\circ$ .]

## References

- [1] Anderson, J.D.Jr.: *Hypersonic and High Temperature Gas Dynamics*, McGraw-Hill, New York, 1989.
- [2] Foley, T.M., "Big Hopes for Small Launchers," *Aerospace America*, Vol. 33, No. 7, 1995, pp. 28-34.
- [3] Russell, G., Cayson, S., Jones, M., Carriger, W., Mitchell, R., Strobel, F., Rembert, M., and Gibson, D., "Laser Window Design for the Army Hypersonic Compact Kinetic Energy Missile," *Journal of Spacecraft and Rockets*, Vol. 43, No. 5, 2006, pp. 982-989.
- [4] Smith, B.A., and Asker, J.R., "NASA Speeds Selection of X-33, X-34 Plans," *Aviation 24 Week and Space Technology*, Vol. 142, No. 11, 1995, pp. 107-109.
- [5] Freeman, D.C., Jr., Talay, T.A., and Austin, R.E., "Single-Stage-to-Orbit Meeting the Challenge", *Acta Astronautica*, Vol. 38, No. 4-8, 1996, pp. 323-331.
- [6] Rathakrishnan, E., *Applied Gas Dynamics*, John Wiley and Sons, Singapore, 2010.
- [7] Ahmed, MYM and Qin, N., "Recent advances in the aerothermodynamics of spiked hypersonic vehicles", *Progress of Aerospace Sciences*, 2011, doi:10.1016/j.paerosci.2011.06.001
- [8] Conti, Raul J, "Laminar Heat-Transfer and Pressure Measurements at a Mach Number of 6 on Sharp and Blunt 15 deg Half-Angle Cones at Angles of Attack Up to 90 deg", NASA Technical Report, NASA-TM-X-33.
- [9] Vashishtha. A., and Rathakrishnan. E., "Breathing Blunt-Nose Concept for Drag Reduction in Supersonic Flow," *Proceedings of the Institution of Mechanical Engineers, Part G: Journal of Aerospace Engineering*, 200, Vol. 223, pp. 31-38.

## References

---

- [10] Mair W.A., (1952) "Experiments on Separation of Boundary Layers on Probes in Front of Blunt-nosed Bodies in a Supersonic Air Stream," *Phil. Mag.*, Vol. 43, No. 342, pp. 695-716, 1952.
- [11] Crawford, D.H.: "Investigation of the flow over spiked-nose hemisphere cylinder at Mach number of 6.8", NASA TND-118-2000.
- [12] Maull, D.J.: "Hypersonic Flow over Symmetric Spiked Bodies", *Jl. Fluid Mech.* 8 (1960), pp. 584.
- [13] Kubota H., "Some Aerodynamic and Aerothermodynamic Considerations for Reusable Launch Vehicles", *AIAA-2004-2428*.
- [14] Motoyama. N., Mihara. K., Miyajima, R., Watanuki. T. and Kubota. H.: Thermal Protection and Drag Reduction with use of spike in hypersonic flow", *AIAA-2001-1828*.
- [15] Kalimuthu, R. and Rathakrishnan E.: "Aerodynamic Characteristics of Blunt Nosed Body with and without Aerospike at Mach 5.87", Proceedings of the 10<sup>th</sup> Asian Symposium on Visualization, 2010.
- [16] Kalimuthu, R.: "Experimental investigation of hemispherical blunt nose body with different spikes in Hypersonic Mach Number", *Ph.D Thesis*, 2009, Department of Aerospace Engineering., IIT, Kanpur.
- [17] Menezes, V., Saravanan S. and Reddy, K.P.J., "Shock Tunnel Study of Spike Aerodynamic Bodies Flying Hypersonic Mach Numbers", *Shock Waves*, 12 (2002), pp. 197-204.
- [18] Mehta, R.C., "Peak Heating for Reattachment of separated flow on a spiked blunt-body", *Jl. Heat Mass Transf.* 36 (2000), pp. 277-283.
- [19] Imamura, O., Watanuki, T., Suzuki, K., and Rathakrishnan, E., "Breathing Blunt Nose (BBN) for Drag Reduction at Hypersonic Speeds", *Journal of Visualization*, Vol. 11, No. 4, 2008, pp. 280.
- [20] Townend, L.H.: "Research and Design for Lifting Reentry", *Progress in Aerospace Sciences*, Vol. 18, pp. 1- 80, 1979.

## References

---

- [21] Mahulikar, S.P.: “Theoretical aerothermal concepts for configuration design of hypersonic vehicles”, *Aerospace Science and Technology*, No. 9, pp. 681–685, 2005.
- [22] Mahulikar, S.P., Khurana, S., Degwekar, S., and Soni, J., : “*Aerothermal Studies of Hypersonic Vehicles*”, 26th I.S.T.S Conference, 2008-o-1-02v, 1-8 June 2008, Hamamatsu, Japan.
- [23] Murphy, K. J., Nowak, R. J., Thompson, R. A., and Brian, R. H., “X-33 Hypersonic Aerodynamic Characteristics,” *AIAA Atmospheric Flight Mechanics Conference and Exhibit*, AIAA-99-4162, Portland, Oregon, Aug. 1999.
- [24] Thompson, R. A., “Review of X-33 Hypersonic Aerodynamic and Aerothermodynamic Development”, *22nd International Congress of Aeronautical Sciences*, Paper ICAS 2000-3.2.3, Harrogate, UK, 28th Aug.-1st Sept.
- [25] Imamura, O., Watanuki, T., Suzuki, K., Kashiwa Wind Tunnel Working Group (Univ. of Tokyo): “Flow characteristics of UT-Kashiwa Hypersonic Wind Tunnel”, *Proceedings of 39th Fluid Dynamics Conference / Aerospace Numerical Simulation Symposium*, p50-55, JAXA-SP-07-016, 2007 (in Japanese).
- [26] CHINO TP-L0225E Thermal Imaging Sensor Manual- Instrumart  
Website: - [www.instrumart.com](http://www.instrumart.com)
- [27] Umar, M.Z., Hamzah, A.R. and Vavilov, V.: Study of Defect Determination using Active Mode Thermography, *Non-Destructive Testing Group*, Malaysian Nuclear Agency.
- [28] Simeonides, G., Vermeulen, J.P., Boerrigter, H.L. and Wendt, J.F.: Quantitative Heat Transfer Measurements in the Hypersonic Wind Tunnels by means of InfraRed Thermography, *IEEE Paper CH3028-8/91/0000-0178*, 1991.
- [29] Khurana, S., Suzuki, K., and Rathakrishnan, E., “Flow field around a Blunted-nosed Body with Spike”, *Int. Jl. Jet Engines and Turbines*, 2012, doi:10.1515/tjj-2012-0002.
- [30] Takama, Y., Suzuki, K., and Rathakrishnan, E., “Visualization and size measurement of vortex shed by flat and arc plates in an uniform flow”, *Int. Rev. Aerosp. Engg.*, Vol. 1, 2008, pp. 55-60.

## *References*

---

## **Acknowledgement**

I express my deep and heartiest gratitude towards my supervisor Prof. Kojiro Suzuki, Professor, Department of Advanced Energy (G.S.F.S.), The University of Tokyo, for giving me the opportunity to work under him, and on this project. I would like to sincerely thank him for his constant guidance, valuable suggestions during discussions, encouragement and support throughout the course of the project which inspired me to work hard & accomplish the goals of the project. The independent atmosphere provided by him instilled in me the perseverance required for independent research, and familiarized me with the joys & rigors of the same. The project helped me develop a true scientific outlook and the ways of analyzing available data and information with a keen faculty of the mind. I am grateful to him for his very generous financial support for my conference trips to Seoul (October 2010), Shizuoka (November 2010), Okinawa (June 2011), Sendai (November 2011) and Shanghai (September 2012). Added to this, I would like to extend my thanks to University of Tokyo for providing me International Research Grant for Conference Travel (New Orleans, 2012).

I would like to sincerely express my thankfulness to Prof. Ethirajan Rathakrishnan, Professor, IIT-Kanpur, India, for introducing me with the importance of Shallow Water Channel Visualization Technique and the subsequent knowledge on the same, which played an instrumental part in arriving at significant conclusions. The exhaustive discussions on the two methods used in the current investigation, and during the preparation of manuscripts for various submittals and the invaluable guidance throughout the tenure of working under him, provided a remarkable experience.

I would like to owe special thanks to all the reviewing Professors (Prof. Kenichi Rinoie, Prof. Kimiya Komurasaki, Prof. Kazuhisa Fujita and Prof. Koji Okamoto), during my Doctoral Research work, investing their time in studying my work and for examining this thesis, whose constructive criticism, in the form of suggestions and recommendations, helped me identify the potential weaker points in my thesis and strengthen them.

## *Acknowledgment*

---

I would like to express my deep gratitude towards Dr. Osamu Imamura and Mr. Takeo Okunuki at the Hypersonic Wind Tunnel facility for their constant availability and assistance in successful operation of the experiments. Their invaluable expertise and assistance in various manufacturing and instrumentation issues ensured the successful completion of the experiments.

I take this opportunity to thank all my lab mates at the Suzuki Laboratory, working together and endless discussions with them gave a platform for numerous ideas to be explored. I would like to convey a vote of thanks especially to Dr. Masashi Kanamori for discussions and support with the understanding of C.F.D., Mr. Yusuke Izumi for the help offered with the working of Rapid Prototyping Machine, Dr. Naohiko Honma for being my mentor at the laboratory and for the life in Japan, together with Mr. Yasumasa Watanabe, Mr. Masashi Yoshida and Mr. Hiroki Nakamoto for the extended support during the conduct of experiments at the Wind tunnel facility. Without them, completion of this phase would not have been possible.

I would like to owe special thanks to Ms. Hiromi Yamazaki, Ms. Maki Kamakura and Ms. Akiko Yamasue at the Students Affairs Section, for taking care of all the administrative and academic logistics related to travel and my Student life at the University of Tokyo.

I am really indebted towards all my language teachers at the International Center (Hongo Campus and Kashiwa Campus), the University of Tokyo, for their excellent teaching style and interactions, making me well-acquainted with Japanese Language, to observe and experience the society, and life in here from a closer perspective together with ability to communicate with people in Japanese, thereby providing a chance for important discussions and learning from their research as well as life experiences. Also, I am indebted towards all the Professors I came in contact at the University of Tokyo, the talks with whom left me with various useful ideas and suggestions to be incorporated.

I would like to thank all my Indian friends at University of Tokyo Indian Student Association (U.T.I.S.A.), Japanese friends, and friends from different countries, without whom my life at the University of Tokyo would have been very

## *Acknowledgment*

---

mundane. You guys never let me feel homesick. In short, I would like to thank the whole of the University to conspire to help me finish my thesis and provide a wonderful stay for four years (including the research student phase).

Finally, I would like to thank my family back in India. Their support and encouragement at all stages, and with time have always motivated me throughout my life especially during the times of difficulties. I completely owe the credit of what I am today, to you.

In the end, I extend my sincere apologies if inadvertently I missed anyone. I would like to dedicate this work to the countless innocent people who lost their lives and suffered during the Great East Japan Earthquake (March 2011). In spite of facing the hostilities during such a huge calamity, the society's patience, endurance and perseverance instilled in me a sense of motivation to continue and to thrive till the completion.

**Shashank Khurana**

**June 2013**

## *Acknowledgment*

---

## Related Publications

### JOURNAL PAPERS

1. Shashank Khurana and Kojiro Suzuki, “Hypersonic Flow Investigation of Aerospikes for Delta-type Lifting Body Configurations”, 2013, *Transactions of the Japan Society for Aeronautical and Space Sciences (JSASS)*.
2. Shashank Khurana, Kojiro Suzuki and Ethirajan Rathakrishnan, 2012, “Flow field around a Blunted-nosed Body with Spike”, *International Journal of Turbo and Jet Engines*, Vol. 29, pp. 217–221. DOI:10.1515/tjj-2012-0002.

### REFEREED CONFERENCE PUBLICATIONS

1. Shashank Khurana and Kojiro Suzuki, “Assessment of Aerodynamic Effectiveness for Aerospike Application on Hypothesized Lifting Body in Hypersonic Flow”, *31<sup>st</sup> A.I.A.A. Applied Aerodynamics Conference*, San Diego, California, U.S.A, 24<sup>th</sup>-27<sup>th</sup> June 2013. (**Accepted**)
2. **Shashank Khurana** and Kojiro Suzuki, “Application of Aerospikes for Lifting-Body Configuration in Hypersonic Flow at Mach 7”, *43<sup>rd</sup> A.I.A.A. Fluid Dynamics Conference and Exhibit*, San Diego, California, U.S.A, 24<sup>th</sup>-27<sup>th</sup> June 2013. (**Accepted**)
3. Shashank Khurana and Kojiro Suzuki, “Towards Heat Transfer Control by Aerospikes for Lifting-Body Configuration in Hypersonic Flow at Mach 7”, *44<sup>th</sup> A.I.A.A. Thermophysics Conference*, San Diego, California, U.S.A, 24<sup>th</sup>-27<sup>th</sup> June 2013. (**Accepted**)
4. Shashank Khurana and Kojiro Suzuki, “Recent Advances in Shock Wave Structure Control of Lifting Bodies in Hypersonic Flow”, *24<sup>th</sup> Symposium on Shock Waves in Japan*, Kita Kyushu, Fukuoka, Japan 13<sup>th</sup>-15<sup>th</sup> March 2013.
5. Shashank Khurana, Kojiro Suzuki and Ethirajan Rathakrishnan, “Parallel Hypersonic flow field simulation around a Spiked Body using Hydraulic Analogy”, *9<sup>th</sup> International Conference on Flow Dynamics*, Sendai, Japan, 19<sup>th</sup>-21<sup>st</sup> September 2012.

### *Related Publications*

---

6. Shashank Khurana, Kojiro Suzuki and Ethirajan Rathakrishnan, “Effect of Vortex-size around Spike Root and Body Base on Possible Hypersonic Drag Reduction”, *7th International Colloquium on Blunt Body Aerodynamics and Applications*, Shanghai, China, 2<sup>nd</sup>-6<sup>th</sup> September 2012.
7. Shashank Khurana, Kojiro Suzuki and Ethirajan Rathakrishnan, “Application of Breathing Blunt Nose Concept to Lifting Body Configuration”, *30th A.I.A.A. Applied Aerodynamics Conference*, New Orleans, Louisiana, U.S.A, 25<sup>th</sup>-28<sup>th</sup> June 2012.
8. Shashank Khurana, Kojiro Suzuki, Yasumasa Watanabe and Ethirajan Rathakrishnan, “Water-channel visualization of flow around a spiked body”, *8th International Conference on Flow Dynamics*, Sendai, Japan, 9<sup>th</sup>-11<sup>th</sup> November 2011.
9. Shashank Khurana and Kojiro Suzuki, “Hypersonic flow investigation of aerospikes for delta-type lifting body configuration”, *28<sup>th</sup> International Symposium on Space Technology & Science*, Okinawa, Japan, 5<sup>th</sup> -12<sup>th</sup> June 2011.
10. Shashank Khurana, Naohiko Honma and Kojiro Suzuki, “Hypersonic Wind Tunnel Experiments on Aerothermal Characteristics of Thick Blunt Delta Lifting Bodies”, *54<sup>th</sup> Joint Space Science Technology Conference*, Shizuoka, Japan, 17<sup>th</sup>-19<sup>th</sup> November 2010.

### POSTER PRESENTATIONS

1. Shashank Khurana and Kojiro Suzuki, “Flow Control Application Studies for Space-plane type High Speed Vehicles”, *India-Japan Symposium on “Frontiers in Science & Technology: Successes and Emerging Challenges”*, Tokyo, Japan, 20<sup>th</sup>-21<sup>st</sup> September 2012.
2. Shashank Khurana and Kojiro Suzuki, “Heat Transfer and Aerodynamic Drag Control Methods for Spacecrafts in Hypersonic Flow”, *University of Tokyo International Symposium on Multidisciplinary Research*, University of Tokyo, Tokyo, Japan, 6<sup>th</sup> March 2011.